ADVANCED FUNCTIONAL MATERIALS
www.afm-journal.de

Scavenging Energy and Information through Dynamically Regulating the Electrical Double Layer

Xiang Li, Zhong Lin Wang, and Di Wei**

The electrical double layer (EDL) between solids and liquids serves as the primary interface for ionic-electronic coupling and is pivotal in nanoscale phenomena, governing electric field effects, ion transport, surface interactions, etc. Dynamically regulating the EDL through mechanical or electrostatic methods can influence charge carrier behavior, thereby impacting energy scavenging and storage processes. This regulation enabled efficient energy scavenging by governing ionic migration and optimizing charge carrier concentration at the interface, presenting a novel avenue to achieve efficient energy and information flow. Here, various scavenging energy and information devices through dynamically regulating the EDL are systematically reviewed. They are classified into three groups by regulating the distribution and movement of charge carriers throughout the entire EDL, diffuse layer, and Debye length range. The review provided a comprehensive overview of the operating principles, influencing factors, output characteristics, and typical applications, along with a discussion on future challenges. This holistic examination offers researchers valuable insights for evaluating their applicability in various scenarios.

1. Introduction

Since the mid-19th century, fossil fuels such as coal and oil have been pivotal energy sources, fueling global industrialization and economic expansion.[1–4] Nonetheless, their finite nature and environmental repercussions, including climate change and pollution, underscore the imperative for transitioning to sustainable alternatives.[5–9] With the emergence of the Internet of Things (IoT)[10–13] and artificial intelligence (AI), the need for efficient distributed energy resources has been accentuated, intensifying the urgency of this transition.[14–18] In natural environments, water stands as one of Earth's most abundant resources,[19–22] offering unique advantages as a renewable energy source due to its widespread distribution and vast reserves. The oceans,[23–27] rivers,[28–31] raindrops,[32–34] and evaporation[35–38] constitute vital elements of water energy, with reserves exceeding 75 TW,[39,40] promising abundant energy resources for humanity. Harnessing this energy could potentially satisfy a significant portion of the global demand, estimated at 18 TW.[41] However, the random[42–44] and low-frequency[45–48] nature of water energy, characterized by wave undulations[49–52] and river flow variations,[53–55] poses challenges for conventional electromagnetic generators.[56–60] Addressing these challenges necessitates the development of efficient and streamlined energy scavenging mechanisms. Overcoming the inherent complexities of scavenging energy from water can unlock its full potential, promoting sustainable development and enhancing global energy security.

The interface between solids and liquids, influenced by the abundance and cyclic nature of water resources,[61–64] occupies a central position on Earth.[65–69] Within this interface, the interplay of charge transfer and ion adsorption gives rise to the electrical double layer (EDL),[70–73] profoundly shaping physical and chemical properties.[74–79] Its significance extends beyond regulating chemical reactions and solute adsorption to encompass interface stability and ion transport, which are crucial for technologies such as batteries,[80–83] supercapacitors,[84–87] and chemical sensors.[88–91] Recent research highlighted the potential of dynamically regulating the EDL to control ionic migration, facilitating efficient electrical current generation.[92–96] This breakthrough laid the foundation for advancements in energy scavenging and storage, particularly in the effective

X. Li, Z. L. Wang, D. Wei
Beijing Institute of Nanoenergy and Nanosystems
Chinese Academy of Sciences
Beijing 101400, P. R. China
E-mail: zhong.wang@mse.gatech.edu; dw344@cam.ac.uk
X. Li
School of Nanoscience and Engineering
University of Chinese Academy of Sciences
Beijing 100049, P. R. China
Z. L. Wang
Beijing Key Laboratory of Micro-Nano Energy and Sensor
Center for High-Entropy Energy and Systems
Beijing Institute of Nanoenergy and Nanosystems
Chinese Academy of Sciences
Beijing 101400, P. R. China
Z. L. Wang
Guangzhou Institute of Blue Energy
Knowledge City, Huangpu District, Guangzhou 510555, P. R. China
Z. L. Wang
Georgia Institute of Technology
Atlanta, GA 30332-0245, USA
D. Wei
Centre for Photonic Devices and Sensors
University of Cambridge
9 JJ Thomson Avenue, Cambridge CB3 0FA, UK

The ORCID identification number(s) for the author(s) of this article can be found under https://doi.org/10.1002/adfm.202405520

DOI: 10.1002/adfm.202405520

harnessing of water energy.[97–100] Novel methodologies like solid-liquid triboelectric,[101–104] hydrovoltaic,[105–108] and osmotic power[109–112] technologies have emerged as solutions for scavenging high-entropy energy from natural environments. Simultaneously, the sensitivity of the EDL to external stimuli has facilitated the development of self-powered information flow fields,[113–118] applicable in human-machine interaction[119–123] and interface probes.[124–127] Hence, dynamic regulation of the EDL represents a promising pathway toward enhancing both energy and information flow,[128] with far-reaching implications for the development of intelligent, autonomous, and efficient IoT and AI systems. This pioneering approach holds substantial promise across diverse application contexts in energy scavenging and self-powered systems. In recent years, notable progress has been achieved in this domain, culminating in the establishment of a relatively comprehensive research framework.

The energy scavenging device assumes a pivotal role in energy infrastructure, with its internal operational mechanisms profoundly influencing the stability, efficiency, and power output of electricity. In this context, it is imperative to conduct a comprehensive review of pertinent scavenging energy devices, focusing on the dynamically regulated components within the EDL. The objective is to effectively integrate output performance with operational mechanisms. This review comprehensively analyzed the evolution of EDL models, from the initial Helmholtz model[129] proposed for conductor surfaces to the latest "two-step" model[130,131] applicable to dielectric surfaces. This analysis offered a crucial theoretical framework for enhanced comprehension and application of the EDL. As per the "two-step" model, energy scavenging devices could be categorized into three groups by regulating the distribution and mobility of charge carriers across the entire EDL, diffuse layer, and Debye length range, as illustrated in **Figure 1**. Initially, in dynamically regulating the entire EDL, mechanical force could move the EDL boundary, inducing directional ionic migration and generating a low-amplitude constant current.[105,132–134] Additionally, the charge distribution in the EDL could be controlled via electrostatic force to induce directional ionic migration, thereby generating high-voltage alternating current (AC) signals.[128,135–137] Second, regulating the diffuse layer involved moving its boundary on the dielectric surface, maintaining a stable EDL. This induced the alternating transfer of electrons between charge-collecting electrodes, generating AC high-voltage output.[101,138–140] Another method involved supplementing the diffuse layer on the dielectric surface with the ionic charge generated by the solid-liquid CE. This created a concentration gradient that drove the directional migration of ions to regulate electron transfer, generating high-power density instantaneous direct current (DC) ionic-electronic coupling output.[128] Third, dynamically regulating the Debye length range of the EDL involved utilizing the ionic concentration gradient or evaporation effect to drive specific polar ions through charged nanochannels in liquid environments, resulting in a constant current signal.[109,141–143] Alternatively, within high-humidity environments, the ionic concentration gradient could drive ions to migrate rapidly through 2D nanofluidic channels.[144–147] This not only enhanced constant current output efficiency but also expanded application possibilities. Furthermore, typical application scenarios of energy scavenging devices were demonstrated to validate their practical efficacy and potential applications in energy scavenging fields[148–150] and self-powered systems.[151–153]

2. The Evolution of the EDL Model

2.1. The EDL Model at the Conductor Interface

The EDL typically refers to a configuration comprising two layers of opposing charges in close proximity to the solid surface when in contact with a liquid. This structure significantly influences electrochemical properties, charge transfer dynamics, and chemical reactions occurring at the interface. Consequently, its composition and structure have been extensively investigated as displayed in **Figure 2**. The earliest Helmholtz EDL model, proposed in 1853,[129] illustrated that when a charged electrode was immersed in an electrolyte solution, two layers of opposite-polarity ions formed within molecular-scale distances near the electrode surface (Figure 2a). The Helmholtz model laid the groundwork for subsequent investigations into charge distribution, potential differences, and the kinetics of electrochemical reactions on electrode surfaces. However, it did not account for ionic diffusion and adsorption in the solution, nor did it consider interactions between the solvent and the electrode. In the early 20th century, the Gouy-Chapman model was introduced,[154,155] incorporating the concept of the diffuse layer (Figure 2b). This model posited that as the charge carried by the electrode increased, the diffuse layer became more compact. As the charge carried by the electrode increased, the diffuse layer became denser in the model. Ionic charge distribution exhibited a functional relationship with the distance to the electrode surface, decreasing exponentially until reaching the bulk solution, influenced by ionic interaction and thermal motion. Closer to the electrode surface, higher charge concentrations prevailed due to the dominance of electrostatic forces over thermal effects, while farther away, the electrostatic effect weakened, resulting in lower charge concentrations. In the 1920s, the Stern model was proposed[156,157] (Figure 2c), building upon and refining previous models. This model provided a more precise depiction of the EDL structure and charge distribution on the conductor surface. The Stern layer, delineated by distance from the electrode surface, comprised an Inner Helmholtz Plane (IHP) and an Outer Helmholtz Plane (OHP). The IHP, closest to the electrode surface, consisted of specifically adsorbed ions and solvent molecules, influenced by both electrostatic and chemical interactions. Meanwhile, the OHP represented a charged plane formed by solvated ions, often involving nonspecific adsorption, with solvated ions interacting solely through long-range electrostatic forces with the electrode surface. The diffuse layer, extending from the OHP to the bulk solution, primarily consisted of free ions in the solution, influenced by both electrostatic force and thermal motion. The combined width of the Stern layer and the diffuse layer typically fell within the Debye length range. This parameter, crucial for describing ion interactions in solution, represented a specific scale of interaction strength between ions. The Debye length of the EDL typically depends on the concentration of electrolytes and the dielectric constant of the medium.[158–160] In dilute electrolyte solutions, the Debye length may be longer, whereas, in concentrated ones, it may be shorter. Generally, the Debye length of the EDL typically ranges from 0.2–20 nm.[161–163] The Stern model has found wide-ranging

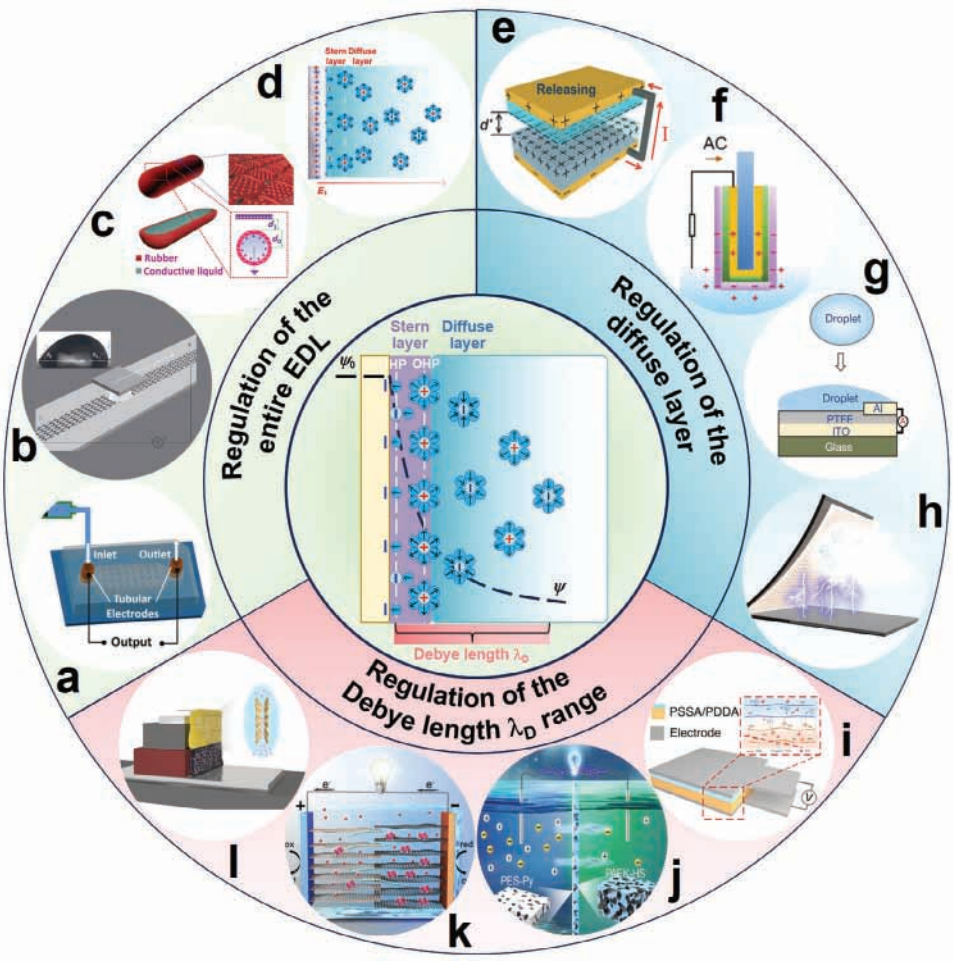

Figure 1. As per the "two-step" model, energy scavenging devices could be categorized into three groups by regulating the distribution and mobility of charge carriers across the entire EDL, diffuse layer, and Debye length range. a–d) Regulation of the entire EDL.[105,128,132,135] e–h) Regulation of the diffuse layer.[101,128,138,139] i–l) Regulation of the Debye length range. Reproduced with permission.[141,142,144,145] a) Copyright 2015, WILEY-VCH. b) Copyright 2014, Springer Nature. c) Copyright 2016, The Authors. d) Copyright 2023, Elsevier Inc. e) Copyright 2013, WILEY-VCH. f) Copyright 2021, American Chemical Society. g) Copyright 2020, Springer Nature. h) Copyright 2023, Elsevier Inc. i) Copyright 2021, Springer Nature j) Copyright 2018, American Association for the Advancement of Science. Distributed under a Creative Commons Attribution NonCommercial License 4.0. k) Copyright 2021, the author(s) retains copyright to individual articles, and the NAS retains an exclusive license to publish these articles and holds copyright to the collectivework. l) Copyright 2024, Springer Nature.

applications in fields such as energy scavenging/storage, chemical sensing, and environmental monitoring, serving as a fundamental theoretical framework for investigating charge transfer processes at the conductor-liquid interface.

2.2. The "Two-Step" EDL Model at the Dielectric Interface

The three models aforementioned mainly focused on the conductor-liquid interface, neglecting the interaction between the dielectric and the liquid. To explore the charge distribution within the EDL at the dielectric-liquid interface, Lin et al. conducted a series of nanoscale charge decay experiments in 2020,[164,165] as depicted in **Figure 3**. These experiments yielded crucial insights into the charge transfer mechanism at the nanoscale level. The initial charge density on the dielectric surface was determined using Kelvin Probe Force Microscopy (KPFM). Subsequently, controlled sliding of deionized (DI) water droplets on the dielectric surface induced solid-liquid contact electrification (CE), facilitating the transfer of charges from the liquid to the dielectric surface (Figure 3a). To distinguish between ions and electrons, the dielectric was heated to 513 K for 10 min. According to thermionic emission theory, electrons reach high energy levels at this temperature, facilitating their emission from the dielectric surface, while ions remain attached to the surface due to potential covalent bonds[166,167] (Figure 3b). Using SiO_2 as an example, the initial charge density increased to -0.8 μC cm^{-2} upon contact with DI water, decreasing to -0.18 μC cm^{-2} after heating, confirming electron emission (Figure 3c). Meanwhile, charges remaining on the dielectric surface were identified as ions. As available charge positions became occupied, the exchange mechanism between solid and liquid ceased, confirming the presence of both electrons and ions during dielectric-liquid CE. The hydrophilicity of dielectric materials significantly

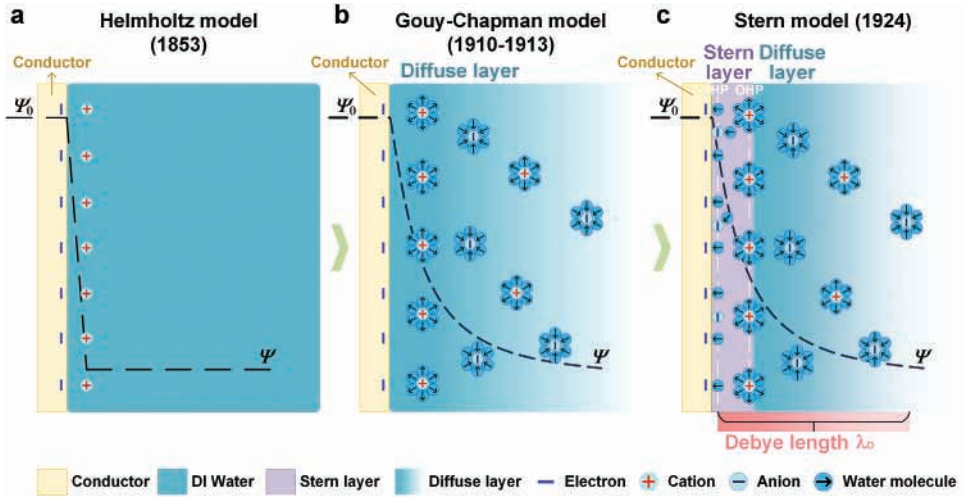

Figure 2. The evolution of the EDL model at the conductor interface. a) The Helmholtz model. b) The Gouy-Chapman model. c) The Stern model.

influences charge transfer during solid-liquid CE processes. Lin et al. conducted nanoscale charge decay experiments in 2020 to explore these effects[168] (Figure 3d). Results revealed that while charge decay curves followed thermionic emission theory across all-dielectric surfaces, the proportions of transferred ions and electrons varied considerably. For instance, when AlN (hydrophobic) contacted DI water, over 88% of the transferred charge was electrons, contrasting with Si_3N_4 (hydrophilic), where electrons accounted for only ≈30%. This discrepancy stems from varying hydrophilic properties of dielectric surfaces, affecting interaction strength between water molecules and dielectric atoms. Stronger interactions on hydrophilic surfaces facilitate ionization reactions, favoring ion dominance in charge transfer, whereas hydrophobic surfaces favor electron transfer. Moreover, during thermionic emission, charge density on some dielectric surfaces decayed, indicating polarity consistency between transferred electrons/holes and ions from liquid to solid. Notably, experiments demonstrated independent behavior between electron and ion transfer during liquid-solid CE processes.

The "two-step" EDL model was introduced by Wang et al. in 2019, encapsulating electron transfer and ion adsorption processes.[130,131] Illustrated in **Figure** 4a, this model provided a comprehensive depiction of charge transfer and EDL structure at the dielectric-liquid interface. Initially, upon contact with the dielectric surface, electrons transferred from water molecules to solid atoms due to electronegativity differences, alongside potential ionization reactions on the solid surface. This led to the simultaneous accumulation of electrons and ions, forming the IHP. Subsequently, electrostatic attraction between IHP and oppositely charged ions in the liquid generated the OHP near the charged dielectric surface. Together, IHP and OHP formed a dense Stern layer with a specific polar net charge, while a diffuse layer comprised ions less tightly bound to the surface. Figure 4b illustrates the "two-step" EDL model, integrating electron transfer and ion adsorption processes to offer a comprehensive framework. This model not only elucidates electronic-ionic interactions but also advances the understanding of solid-liquid interface behavior, fostering innovation in interface research. In the EDL structure, both the Stern model at the conductor surface and the "two-step" model at the dielectric surface comprise Stern and diffuse layers, with widths typically within the Debye length range. Dynamic regulation of charge carrier distribution and movement across the entire EDL, diffuse layer, and Debye length range via mechanical or electrostatic forces enables the construction of energy scavenging devices.

3. Energy Scavenging Devices Based on Dynamic Regulating the Entire EDL

3.1. Moving the EDL Boundary on the Solid Surface

3.1.1. Moving the EDL Boundary on the Dielectric Surface

Mechanical force applied to move the entire EDL boundary on the dielectric surface could prompt the directional migration of free ions within the diffuse layer, inducing the DC ionic current, as shown in **Figure** 5. Upon dropping the first droplet onto the initial dielectric surface, the solid-liquid CE effect was initiated, triggering charge transfer and EDL formation (Figure 5a). According to the "two-step" EDL model, a Stern layer with net negative charges formed on the dielectric surface, tightly adhering to the solid surface, while positive charges in the diffuse layer remained free and capable of directional migration with droplet movement. As the droplet continued to slide, the entire EDL boundary extended forward, leading to charge carrier redistribution at the solid-liquid interface and an incremental increase in positive charges within the diffuse layer (Figure 5b). When the droplet slid off the dielectric surface, positive charges in the diffuse layer contacted the electrode surface, inducing unidirectional electron transfer and generating the DC ionic current (Figure 5c). As subsequent droplets traversed the dielectric surface, the densely adhered Stern layer could gradually form, impeding ongoing charge transfer between the droplets and the solid surface. Consequently, the amount of positive charge carried in the diffuse layer of the droplets sliding through the dielectric surface might decrease, weakening the induced ionic current (Figure 5d). This process involves a sophisticated interplay of mechanical force, charge transfer dynamics, and EDL

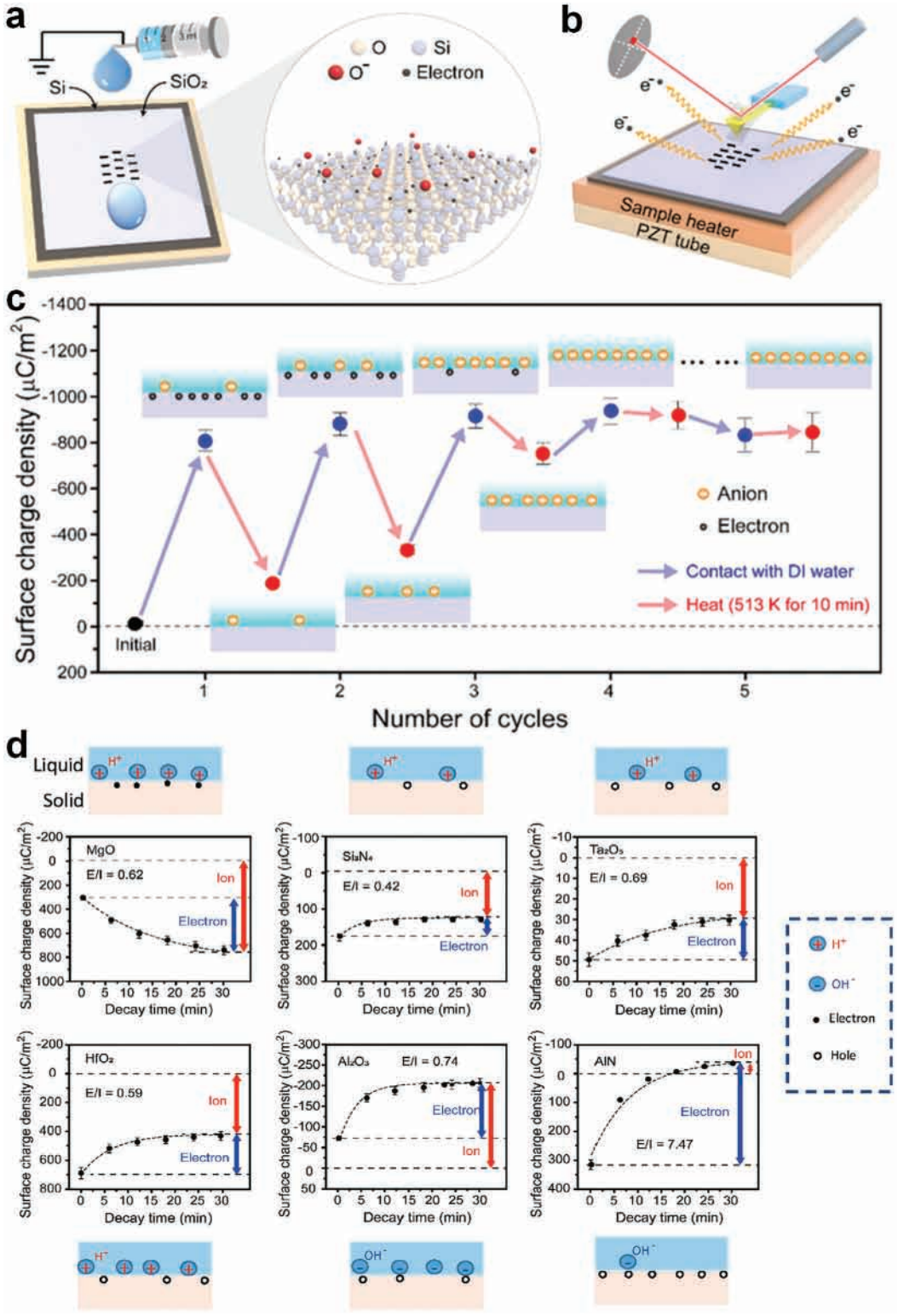

Figure 3. The nanoscale charge decay experiments based on the thermionic emission effect were carried out by Lin et al. in 2020. a) DI water droplets slid on the dielectric surface, and charges were transferred from the liquid to the dielectric surface. Reproduced with permission.[164] Copyright 2020, The Author(s). Distributed under the terms of the Creative Commons CC BY license. b) The principle of thermionic emission. c) The ionic charge density on the SiO_2 surface gradually increased with successive progress of thermionic emission. Reproduced with permission.[165] Copyright 2024, Elsevier Inc. d) The hydrophilicity of dielectric materials played a crucial role in the transferred proportion of ions and electrons during the dielectric-liquid CE process. Reproduced with permission.[168] Copyright 2020, Wiley-VCH.

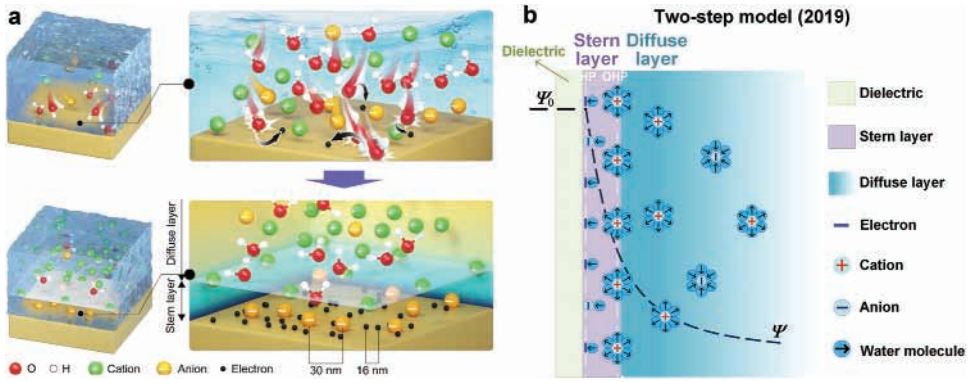

Figure 4. The "two-step" EDL model at the dielectric-liquid interface was proposed by Wang et al. in 2019. a) The "two-step" formation process incorporated both electron transfer and ion adsorption mechanisms. Reproduced with permission.[131] Copyright 2022, American Chemical Society. b) The EDL structure and charge composition of the "two-step" model.

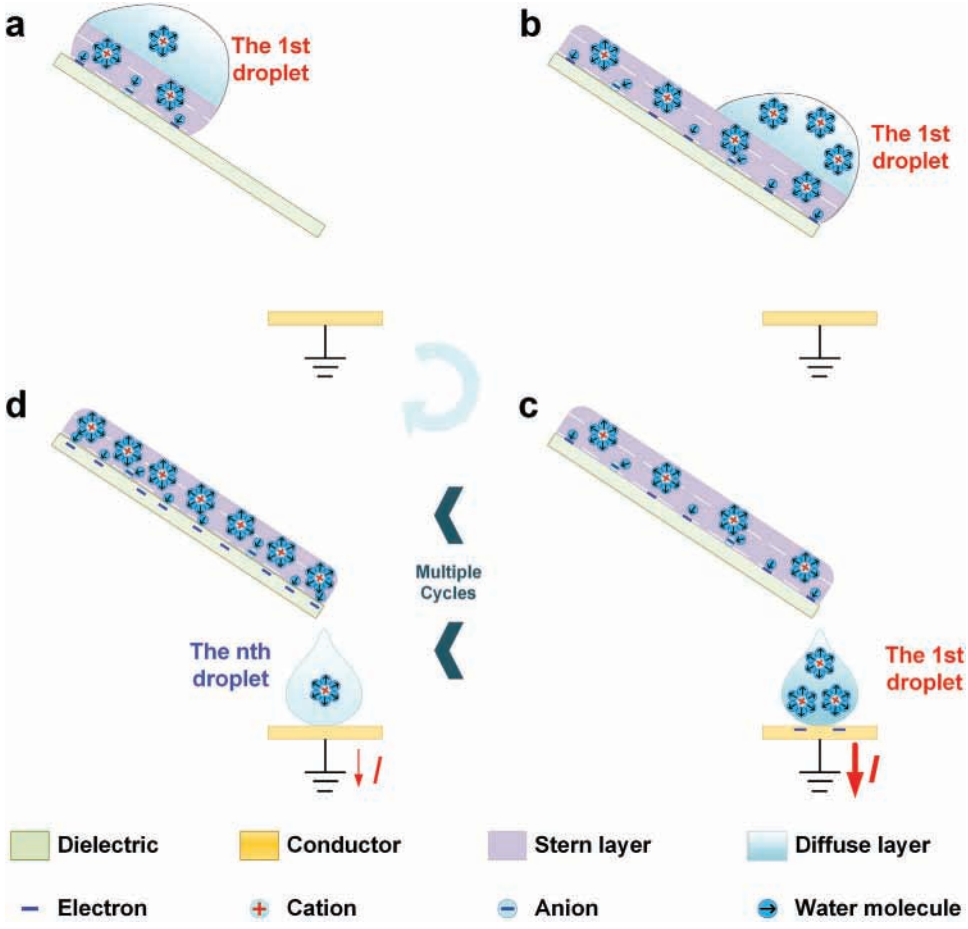

Figure 5. Mechanical force applied to move the entire EDL boundary on the dielectric surface could prompt the directional migration of free ions within the diffuse layer, inducing the DC ionic current. a) Upon dropping the first droplet onto the initial dielectric surface, the solid-liquid CE effect was initiated, triggering charge transfer and EDL formation. b) As the droplet continued to slide, the entire EDL boundary extended forward, leading to charge carrier redistribution at the solid-liquid interface and an incremental increase in positive charges within the diffuse layer. c) When the droplet slid off the dielectric surface, positive charges in the diffuse layer contacted the electrode surface, inducing unidirectional electron transfer and generating the DC ionic current. d) As subsequent droplets traversed the dielectric surface, the densely adhered Stern layer could gradually form, impeding ongoing charge transfer between the droplets and the solid surface and weakening the induced ionic current.

behavior on the dielectric surface, leading to the generation of the DC signal. A comprehensive understanding of these mechanisms is essential for various applications involving surface interactions and energy scavenging.

The capability to dynamically regulate the entire EDL on dielectric surfaces has paved the way for controlling surface properties, manipulating fluid behavior, and generating electrical signals. In 2005, Heyden et al. introduced a technique for dynamically regulating the entire EDL on dielectric material surfaces, subsequently laying the groundwork for the development of energy scavenging devices,[169] as demonstrated in **Figure 6**a. They observed that when an electrolyte solution was driven through a SiO_2 nanochannel, it generated a streaming current of around a hundred picoamperes, marking an early exploration of leveraging dynamic EDL manipulation for energy scavenging. Experimental findings revealed that the short-circuit current (I_{SC}) amplitude generated by the device correlated with the nanochannel height, electrolyte solution concentration, and applied pressure. Increasing nanochannel height augmented the solid-liquid contact area, facilitating charge transfer during contact electrification and elevating the ionic content in the diffuse layer. Consequently, I_{SC} amplitude continuously increased (Figure 6b). Solution concentration below 10^{-4} M effectively enhanced solution conductivity, reducing device internal resistance and consequently boosting current amplitude. However, exceeding 10^{-3} M led to rapid Stern layer formation on the SiO_2 surface, impeding further charge transfer and resulting in reduced diffuse layer charge and subsequent current amplitude decrease. Elevated liquid pressure accelerated the directional migration of ionic charges in the diffuse layer, enhancing output performance (Figure 6c). Additionally, charge transfer direction differences during solid-liquid CE due to dielectric material electronegativity significantly influenced device performance. Flowing KCl solution through SiO_2 surfaces resulted in the positively charged diffuse layer, while on the polylysine surface, they became negatively charged, indicating opposing charge distributions in the EDLs formed at two dielectric-liquid interfaces. In 2015, the microfluidic generator (MFG) developed by Zhang and colleagues represented an advancement aimed at further improving output performance,[132] as depicted in Figure 6d. This device was designed to generate a more efficient constant current by driving a KCl solution to slide on a Polydimethylsiloxane (PDMS) prepolymer surface. The experimental evidence indicated that the directional migration direction of ionic charges in the diffuse layer depended on the flow direction of liquid, which in turn determined the direction of the generated current (Figure 6e). Furthermore, the experiments showcased the exceptional solution compatibility of the device. Under consistent ionic concentrations, and as long as the ions migrating directionally maintained the same valence state in the solution, their output performance remained nearly identical (Figure 6f). Leveraging microfluidic principles in the MFG optimized fluid-surface interactions, enhancing charge transfer and subsequently improving output performance. For instance, when a 1 μM KCl solution flowed through the device at a rate of 0.1 mL min^{-1}, it generated a constant current of 1.75 nA.

In addition to external mechanical driving, the EDL boundary could also be influenced by liquid evaporation. In 2022, Chi et al. introduced a liquid-solid triboelectric nanogenerator (L-S TENG),[170] harnessing the combined effects of liquid evaporation and capillary forces. This setup facilitated DI water flow within the Al_2O_3 ceramic sheet, initiating the triboelectric charging process and generating electrical output, as displayed in Figure 6g. Experiments confirmed that controlling the sealing of environments could regulate liquid evaporation, ensuring continuous liquid flow within nanochannels and stable electrical output (Figure 6h). Moreover, increasing environmental temperature or wind speed could enhance liquid evaporation, effectively boosting electric current amplitude (Figure 6i). This highlighted the significance of environmental factors in optimizing energy-scavenging device performance and suggested strategies for enhancing efficiency. The optimized L-S TENG demonstrated promising capabilities, with performance metrics of 0.3 μA I_{SC} and 0.7 V open-circuit voltage (V_{OC}), suitable for various self-powered systems and energy scavenging applications. However, extended liquid flow over the solid surface might lead to the formation of a dense Stern layer, potentially inhibiting subsequent charge transfer and compromising device output stability. To tackle this challenge, Dong et al. developed a gas-liquid two-phase flow-based triboelectric nanogenerator (GL-TENG) in 2022,[171] as illustrated in Figure 6j. This innovative design countered the dense Stern layer by utilizing dielectric breakdown. It optimized the contact area and sliding velocity between deionized water and the polytetrafluoroethylene (PTFE) tube via gas-liquid two-phase flow dynamics, promoting solid-liquid charge exchange. This enhanced ion mobility and charge content within the diffuse layer, ensuring stable current output. During continuous operation, accumulated charge triggered dielectric breakdown, generating a pulse current and resetting the state of the tube (Figure 6k). Overall, incorporating dielectric breakdown mechanisms into GL-TENG designs could lead to improved device stability and more efficient energy scavenging. It could generate an extremely high I_{SC} of 867 μA (Figure 6l), a V_{OC} of 3789 V, and a volumetric peak power density (P_R) of 143.6 mW cm^{-3}.

3.1.2. Moving the EDL Boundary on the Charge Collecting Layer of the Dielectric Substrate

When the dielectric surface was coated with an ultra-thin conductor layer, the movement of the boundary of the entire EDL on its surface could also generate the DC electrical signal. The charge collecting layer facilitates low-resistance charge transport, minimizing losses and maximizing DC signal amplitude. As the EDL boundary moved, ions in the diffuse layer migrated directionally, as illustrated in **Figure 7**. When a DI water droplet was deposited onto an ultra-thin charge-collecting layer, it penetrated the layer and contacted the underlying dielectric substrate. This interaction initiated solid-liquid charge exchange, resulting in the formation of an EDL near the charge-collecting layer (Figure 7a). As the droplet was propelled along the surface of the charge-collecting layer, the boundary of the entire EDL extended forward with the droplet, giving rise to a new segment at the leading edge of the droplet. Consequently, an asymmetric EDL was established between the region rich in charge at the rear of the droplet and the region with sparse charge at the front. This asymmetrical charge distribution within the EDL engendered a concentration gradient, propelling directional ion migration

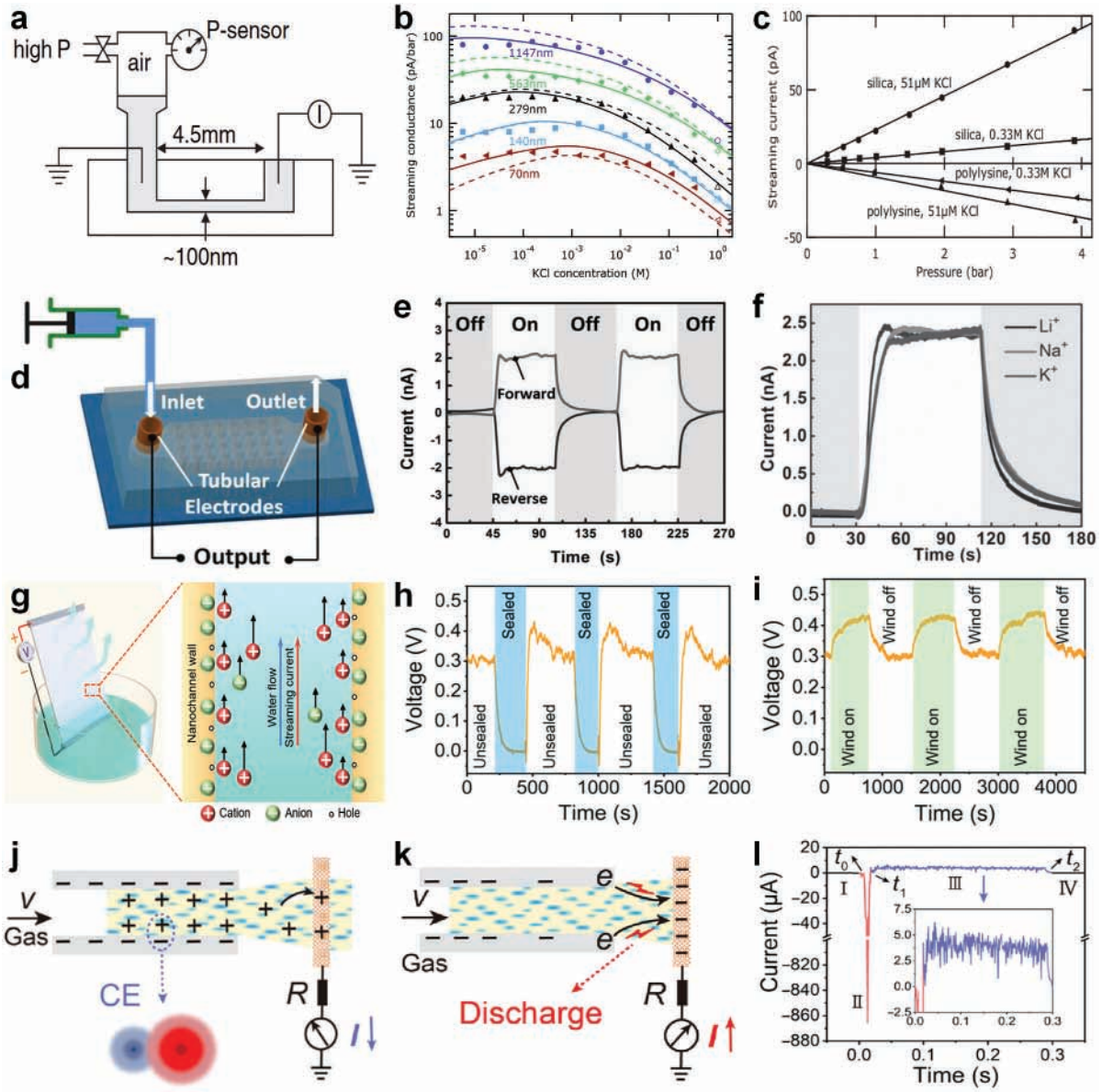

Figure 6. A series of energy scavenging devices were developed based on moving the entire EDL boundary on the dielectric surface. a) A technique for dynamically regulating the entire EDL on dielectric material surfaces was introduced by Frank et al. in 2005.[169] b) The I_{SC} was related to the height of the nanochannel and the ionic concentration. c) The I_{SC} was also related to the pressure on the liquid and the electronegativity of dielectric materials. a–c) Reproduced with permission.[169] Copyright 2024, American Physical Society. d) The MFG was developed by Zhang and colleagues in 2015.[132] e) The direction of the generated current depended on the flow direction of the liquid. f) The MFG exhibited exceptional solution compatibility. d–f) Reproduced with permission.[132] Copyright 2015, Wiley-VCH. g) The L-S TENG was developed by Chi et al. in 2022,[170] harnessing the combined effects of liquid evaporation and capillary forces. h) Controlling the sealing of environments could regulate liquid evaporation, ensuring continuous liquid flow within nanochannels and stable electrical output. i) Increasing environmental temperature or wind speed could enhance liquid evaporation, effectively boosting electric current amplitude. g–i) Reproduced with permission.[170] Copyright 2022, The Authors. Distributed under the terms of the Creative Commons CC BY license. j) The GL-TENG based on the solid-liquid CE and dielectric breakdown was developed by Dong and his colleagues in 2022.[171] k) During continuous operation, accumulated charge triggered dielectric breakdown, generating a pulse current and resetting the state of the tube. l) The GL-TENG could generate an extremely high I_{SC} of 867 μA. j–l) Reproduced with permission.[171] Copyright 2012, American Association for the Advancement of Science. Distributed under a Creative Commons Attribution NonCommercial License 4.0.

within the droplet. This, in turn, instigated corresponding charge transfer within the charge collecting layer, culminating in the generation of a DC ionic current (Figure 7b). Hence, mobilizing the droplet across the charge-collecting layer surface of the dielectric substrate through mechanical force to manipulate the EDL boundary proved efficacious in power generation. This methodology exploited the reorganization of charges within the EDL to instigate current flow, presenting opportunities for diverse applications. With prolonged sliding of the droplets, the potential formation of a compact Stern layer might ensue, potentially

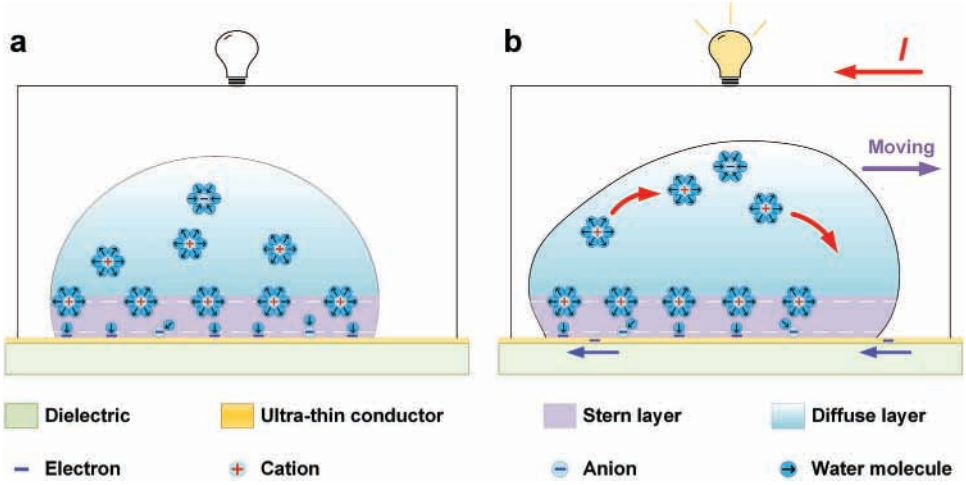

Figure 7. When the dielectric surface was coated with an ultra-thin conductor layer, the movement of the boundary of the entire EDL on its surface could also generate the DC electrical signal. a) When a DI water droplet was deposited onto an ultra-thin charge collecting layer, it penetrated the layer and contacted the underlying dielectric substrate, which initiated solid-liquid charge exchange, resulting in the formation of an EDL near the charge collecting layer. b) As the droplet was propelled along the surface of the charge collecting layer, the boundary of the entire EDL extended forward with the droplet, which culminated in the generation of a DC ionic current.

impeding subsequent solid-liquid CE effects and consequently diminishing device performance output.

Energy scavenging devices exploiting the manipulation of the EDL boundary on the charge collecting layer surface of the dielectric substrate have garnered considerable attention and have undergone swift advancement in recent years. As early as 2014, Yin et al. introduced a droplet-driven hydrovoltaic generator, thereby highlighting the promise of this paradigm.[105] In this apparatus, the movement of a droplet across a single-layer graphene surface on a PET (polyethylene terephthalate) substrate yielded a millivolt-level V_{OC}, as shown in **Figure** 8a. Experiments validated that the direction of the generated potential depended on the sliding direction of the droplet (Figure 8b). The ability to manipulate the sliding direction of the droplet facilitates precise control over the extension direction of the EDL, consequently shaping the formation of the ionic concentration gradient within the asymmetric EDL. This, in turn, governs the direction of ionic migration and thereby regulates the generation of potential in a predetermined direction. Both the velocity of sliding and the number of droplets exert influence over the magnitude of the generated potential (Figure 8c). Increasing the sliding speed of the droplet accelerated the migration speed of ions within the EDL, thereby, allowing more ions to be involved in creating the potential difference and amplifying the generated potential. Simultaneously, when multiple droplets slid simultaneously on the graphene surface in sequence, they induced the migration of ions in series, leading to a cumulative effect and increasing the overall potential generated by the device. Further, the development of a wave-driven hydrovoltaic generator proposed by Yin et al. in 2014 represented a significant advancement in such energy scavenging technology,[172] as depicted in Figure 8d. Through systematic insertion and withdrawal of a monolayer graphene sheet on the PET substrate into and out of the liquid medium, the manipulation of the EDL boundary could be orchestrated to harness mechanical energy and convert it into instantaneous AC electrical signals. Within this apparatus, the amplitude of the V_{OC} generated during the graphene insertion process directly correlated with the operational velocity, suggesting that elevating the operational speed could proportionally enhance the velocity of directional ion migration (Figure 8e). Nevertheless, when the pulling velocity surpassed the critical dewetting threshold of graphene from water, the resultant electric potential remained nearly invariant. Operating within a 0.6 M NaCl solution (akin to seawater), the hydrovoltaic generator exhibited higher V_{OC} and I_{SC} based on the larger solid-liquid contact area and the relative motion speed. Employing two power generation units in series, the V_{OC} was increased to 80 mV, and the I_{SC} reached 8 μA when connected in parallel (Figure 8f).

Energy scavenging devices relying on the EDL boundary on the charge collecting layer atop dielectric substrates epitomized a forefront strategy for ocean energy extraction. To thoroughly explore the influence of dielectric substrate materials and charge collecting layer thickness on device efficacy, and to authenticate the charge transfer mechanism at the micro-interface, Yang et al. undertook a sum-frequency vibrational spectroscopy investigation of a polymer-supported graphene-based hydrovoltaic generator in 2018,[173] as displayed in Figure 8g. Sum-frequency vibrational spectra from various interfaces—solution-graphene, solution-polymer, and solution-graphene/polymer—were analyzed. Experimental results showed exclusive ion adsorption onto the polymer or graphene/polymer interface, with no adsorption observed solely on graphene. These findings support the conclusion that charge transfer predominantly occurs at the solid-liquid contact interface between the liquid and the dielectric substrate. Additionally, a decrease in the sum-frequency signal was observed with an increase in graphene layers, indicating reduced ion adsorption on the graphene/polymer surface (Figure 8h). Hence, graphene exhibited no active ion attraction, functioning solely as a charge collecting layer to facilitate electron transport. The interaction between ions and the polymer surface was observed to be of short range, with graphene displaying a mild shielding effect. Furthermore, the influencing factors of the

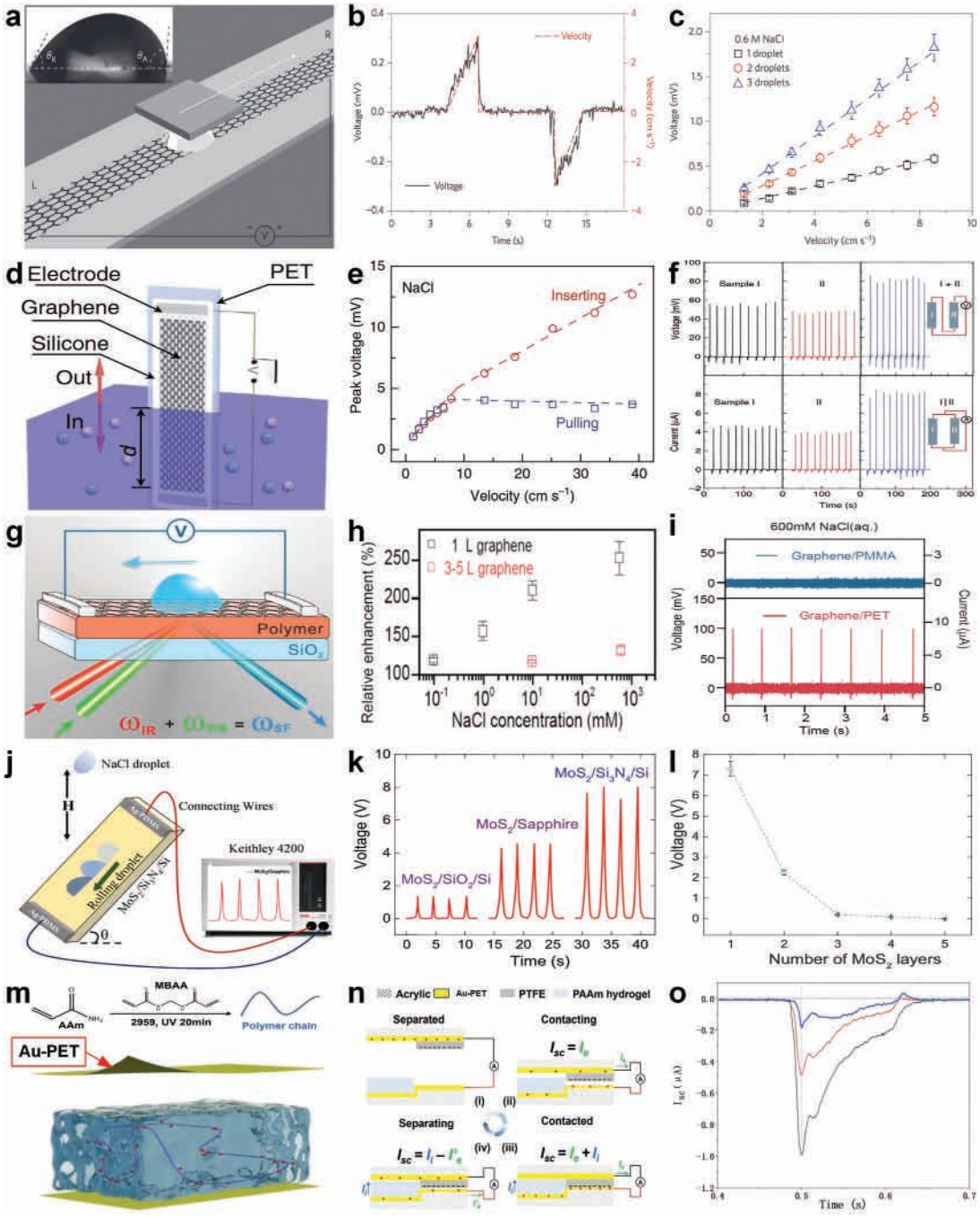

Figure 8. Energy scavenging devices were developed based on moving the EDL boundary on charge collecting layer of dielectric substrates. a) A droplet-driven hydrovoltaic generator was proposed by Yin et al. in 2014.[105] b) The V_{OC} direction depended on the sliding direction of the droplet. c) Both the sliding speed and the number of droplets could affect the V_{OC}. a–c) Reproduced with permission.[105] Copyright 2014, Springer Nature. d) The wave-driven hydrovoltaic generator proposed by Yin et al. in 2014.[172] e) The V_{OC} during the insertion of graphene into the liquid was proportional to the operating speed. f) By employing two power generation units in parallel, the I_{SC} could reach 8 μA. d–f) Reproduced with permission.[172] Copyright 2014, Springer Nature. g) The charge transfer mechanism on the polymer-supported graphene-based hydrovoltaic generator was explored by Yang et al. in 2018.[173] h) The sum frequency signal was reduced with an increase in the number of graphene layers. i) When employing dielectric materials with stronger electronegativity or enhanced ionic adsorption capacity, the V_{OC} could be improved. g–i) Reproduced with permission.[173] Copyright 2018, American Chemical Socie. j) A nanogenerator utilizing MoS_2 as the charge collecting layer was developed by Kumar et al. in 2021.[174] k) Employing Si_3N_4/Si as the substrate resulted in the V_{OC} exceeding 7 V. l) As the number of MoS_2 layers increased, the generated V_{OC} continuously decreased. j–l) Reproduced with permission.[174] Copyright 2021, Elsevier B.V. m) In 2024, a DC-iontronic TENG capable of generating an ionic-electronic coupled current was proposed.[175] n) Temporally controlling EDL formation could regulate the AC electronics displacement current of the conventional TENG, thus enabling the DC ionic-electronic coupling output. o) As the ionic current increased, its regulatory effect on the electronic displacement current became more pronounced. m–o) Reproduced with permission.[175] Copyright 2024, American Chemical Society.

energy scavenging device could be further corroborated through droplet drop experiments (Figure 8i). Employing dielectric materials possessing stronger electronegativity or augmented ionic adsorption capacity effectively facilitated charge transfer and redistribution between solid and liquid, resulting in higher V_{OC} in the device. Hence, this study likely yielded valuable insights into optimizing hydrovoltaic generator design and augmenting energy scavenging efficiency. While employing graphene as a charge collecting layer offered high current output owing to its superior conductivity, it diminishes the V_{OC} quickly in the energy scavenging device due to its exceedingly low internal resistance, thereby constraining practical applications. In contrast, utilizing semiconductor materials to collect charges enabled both current conduction and the generation of higher voltage output due to the increased internal resistance. In 2021, Kumar et al. developed a nanogenerator utilizing MoS_2 as the charge collecting layer,[174] as illustrated in Figure 8j. By facilitating the sliding of 0.6 M NaCl solution droplets on the MoS_2 surface, the generated potential significantly surpassed that of energy scavenging devices relying on graphene to collect charges. Its output was evaluated using different dielectric substrates to ensure sufficient charge transfer upon contact with the droplet (Figure 8k). Ultimately, employing Si_3N_4/Si as the substrate resulted in a V_{OC} exceeding 7 V. Additionally, experiments were conducted to verify the screening effect of the charge collecting layer on the charge transfer between the droplet and the dielectric substrate. It was observed that as the number of MoS_2 layers increased, the generated V_{OC} continuously decreased (Figure 8l). Thus, the output performance of the device could be effectively regulated by selecting the dielectric substrate materials and controlling the charge collecting layer thickness. In addition to directly converting mechanical energy into electrical energy output, temporally controlling EDL formation could also be used as a rectifier. Recently, we proposed a DC-iontronic TENG capable of generating an ionic-electronic coupled current,[175] as demonstrated in Figure 8m. By regulating the formation time of EDLs between the hydrogel and the dielectric substrates, an ionic concentration gradient could be established to drive the directional migration of ions, resulting in stable ionic currents between charge collecting layers. It regulated the AC electronic displacement current of the conventional TENG, enabling the DC-iontronic TENG to produce DC outputs (Figure 8n). The experiment showed that as the ionic current increased, its effect on regulating the electronic displacement current became more significant (Figure 8o).

3.2. Regulating the Charge Distribution in the EDL by Electrostatic Fields

3.2.1. Regulating the Charge Distribution in the EDL by Unidirectional Electrostatic Field

During the manipulation of the EDL boundary on the dielectric surface, a compact Stern layer bearing net charges may form at the solid-liquid interface as the droplet progresses, potentially impeding subsequent charge transfer. Apart from triggering dielectric breakdown to eliminate net charges on the dielectric surface, the electrostatic field generated by solid-solid CE could be leveraged to modulate the charge density within the Stern layer. This regulation prompts the qualitative migration of free ions in the diffuse layer, thereby engendering efficient power output. This regulatory mechanism offers a specific avenue for optimizing energy scavenging processes, as shown in **Figure 9**. Upon contact between the liquid and the upper surface of the electronegative dielectric I, a stable EDL formed at the contact surface due to solid-liquid CE (Figure 9a). Subsequently, when the electropositive dielectric II, possessing higher electronegativity, contacted dielectric I from the opposing side, solid-solid CE effects caused electron transfer from the surface of dielectric I to dielectric II. As dielectric II, now carrying electrons, moved away from dielectric I, the positive electrostatic field on the surface of material I gradually intensified (Figure 9b). This facilitated enhanced charge transfer between the liquid and dielectric I, resulting in a higher net negative charge density in the Stern layer. Consequently, there was an increase in the concentration gradient of cations, propelled away from the contact interface toward the charge collecting electrode under electrostatic interaction, thereby inducing electron transfer to the electrode surface and yielding a positive ionic current. Upon adsorption of cations onto the electrode surface, the directional migration of ions ceased (Figure 9c). As dielectric II, carrying electrons, gradually returned to the surface of dielectric I, the positive electric field on the surface of material I was continually shielded. Under the electrostatic interaction of net charges in the Stern layer, positive charges adsorbed on the charge collecting electrode surface could be driven to migrate, while electrons were induced to transfer out of the electrode surface, resulting in a reverse ionic current (Figure 9d). Therefore, utilizing electrostatic fields to regulate the charge density in the Stern layer of the EDL showed promising potential for enhancing ionic migration in the diffuse layer to facilitate AC output generation. Further exploration in this direction could lead to unlocking new opportunities for energy scavenging.

Based on the dynamic regulation of the entire EDL via the electrostatic field, Yi et al. successfully introduced a novel shape-adaptive triboelectric nanogenerator (SA-TENG) in 2016,[135] as shown in **Figure 10**a. This device utilized the positive electrostatic field on the dielectric surface with lower electron affinity to propel the EDL at the contact interface between the sealed rubber cover and the internal conductive liquid, resulting in efficient energy extraction. Experimental findings revealed that increasing the separation distance between the dielectric material and the rubber cover could significantly enhance the charge transfer of the nanogenerator (Figure 10b). This enhancement might be attributed to the controlled regulation of the separation distance, allowing modulation of the electrostatic field intensity changes, thereby regulating the net charge density in the Stern layer within the EDL to modulate the directional ionic migration in the diffuse layer. Moreover, altering the radius of the rubber cover facilitated regulations to the contact area with the internal conductive liquid, potentially augmenting the content of free ions in the diffuse layer and further enhancing the output performance of the SA-TENG. Leveraging the insulating properties of dielectric materials, energy scavenging devices employing electrostatic fields to regulate the EDL were inclined to yield high-voltage outputs, possibly owing to effective control over charge distribution within the EDL. Consequently, the open-circuit voltage V_{OC} of the SA-TENG in single-electrode mode could achieve 70 V (Figure 10c). Connecting the charge collecting layer on the

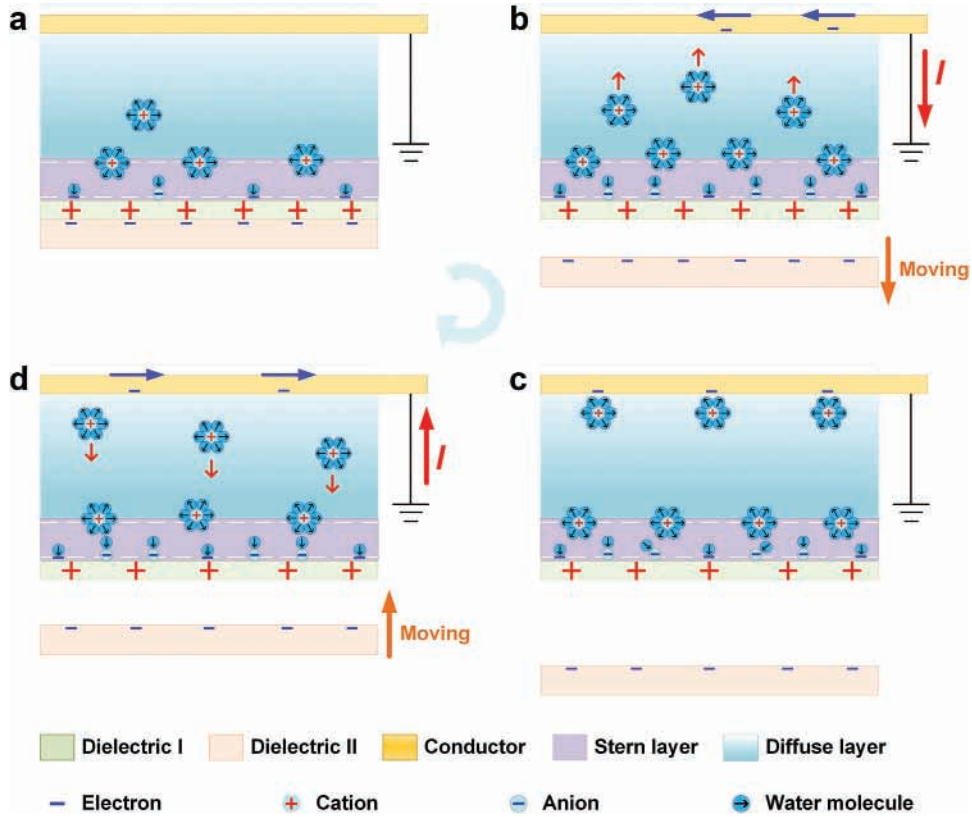

Figure 9. The electrostatic field generated by solid-solid CE could be leveraged to modulate the charge density within the Stern layer to prompt the qualitative migration of free ions in the diffuse layer, thereby engendering efficient power output. a) Upon contact between the liquid and the upper surface of the electronegative dielectric I, a stable EDL formed at the contact surface due to solid-liquid CE. b) As dielectric II carrying electrons, moved away from dielectric I, the positive electrostatic field on the surface of material I gradually intensified. c) Upon adsorption of cations onto the electrode surface, the directional migration of ions ceased. d) As dielectric II gradually returned to the surface of dielectric I, positive charges adsorbed on the charge collecting electrode surface could be driven to migrate, while electrons were induced to transfer out of the electrode surface, resulting in a reverse ionic current.

back of the dielectric material with the conductive liquid enabled the P_R of the SA-TENG in vertical contact-separation mode to reach ≈0.2 mW cm^{-2}. In 2019, Wu et al. developed a liquid single-electrode TENG based on graphene oxide dispersion (GO LS-TENG) to further investigate the effect of ionic concentration in the conductive liquid on the output performance of the device,[176] as depicted in Figure 10d. This GO LS-TENG utilized the positive electric field carried by the human skin surface to regulate the EDL at the contact interface between the PDMS cover and the internal GO dispersion, thereby generating effective power output. The experimental findings revealed that the ISC experienced a continuous increase as the GO concentration in the dispersion rose from 0 to 10 mg mL^{-1} (Figure 10e). This escalation was attributed to the increased ionic concentration resulting from the hydrolysis of oxygen-containing functional groups on the surface of GO within the dispersion. This increase not only facilitated charge transfer at the solid-liquid interface, thereby boosting the concentration of free ions in the diffuse layer, but also reduced the internal resistance of the device, consequently enhancing its output performance. However, when the GO concentration reached 15 mg mL^{-1}, the generated I_{SC} started to decrease. This decrease might be ascribed to the excessive ionic concentration produced by hydrolysis, leading to the formation of a dense Stern layer on the PDMS surface, which failed to effectively shield the electrostatic field, thus impeding charge migration and diminishing the output performance of the LS-TENG. Upon tapping with the palm, the GO LS-TENG exhibited notable contact output performance, with a P_R density of 0.50 mW cm^{-2} (Figure 10f). These findings underscored the potential of the fabricated GO LS-TENGs to enable advanced functionalities in wearable technology, by offering a reliable and efficient energy scavenging solution that could conform to the dynamic and flexible nature of wearable devices.

In addition to regulating the ionic concentration in the conductive liquid, modifying the strength of the electrostatic field could effectively regulate the output performance of the device. In 2019, Chen et al. developed a triboelectric nanogenerator featuring a hierarchical micro-nanostructure (HM-TENG), proficient in efficiently scavenging both mechanical energy and raindrop energy,[177] as displayed in Figure 10g. In this TENG, a hierarchical micro-nanostructure was created on the elastomer surface through electrospinning. The increased surface roughness significantly augmented the microscopic contact area with the dielectric film, boosting the electrostatic field strength. This facilitated the directional migration of more free ions at the elastomer-ion conductor interface, leading to higher current output.

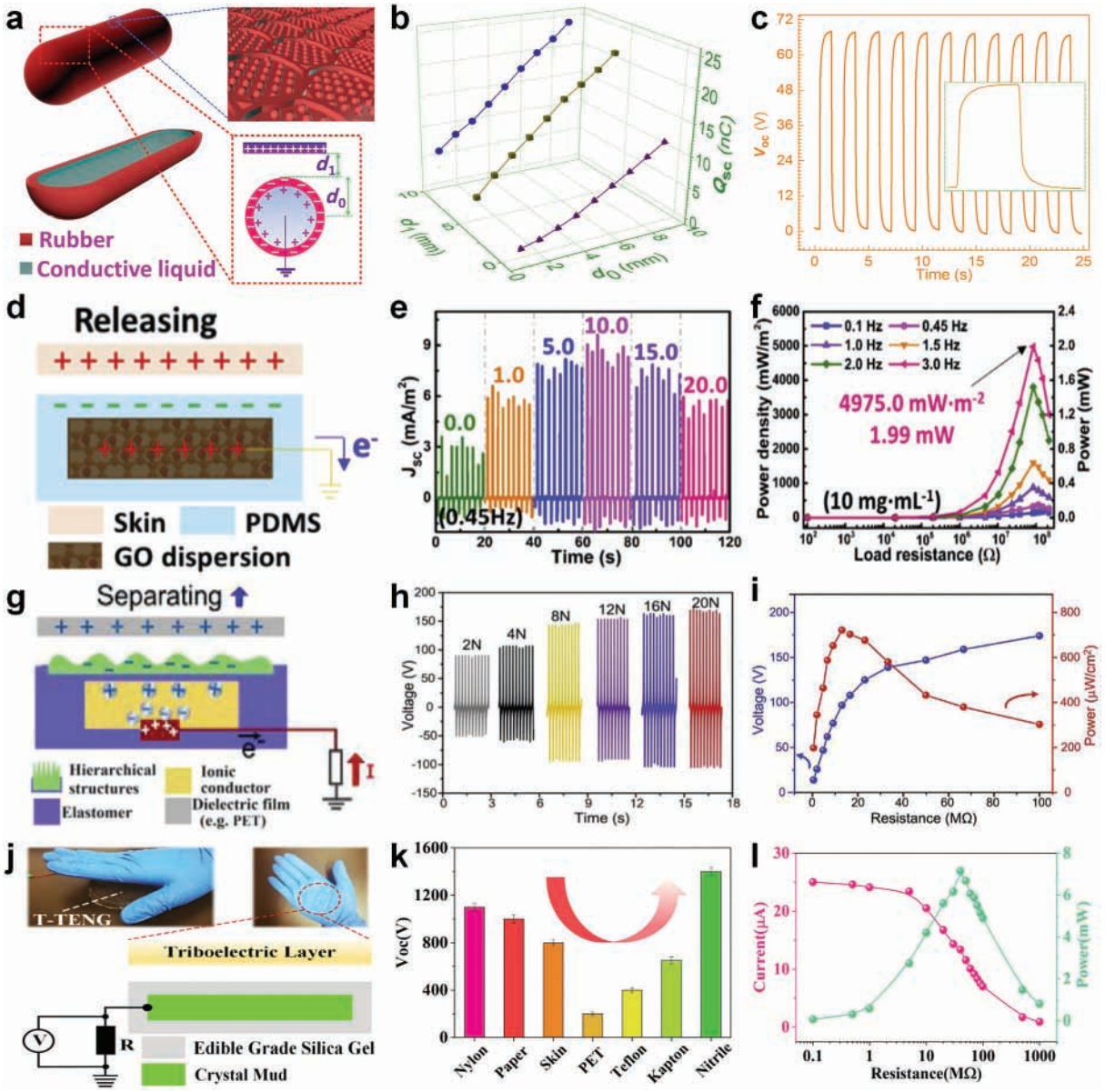

Figure 10. The energy harvesting devices were developed based on dynamically regulating the charge distribution in the EDL by the electrostatic field. a) The SA-TENG was developed by Yi et al. in 2016.[135] b) Increasing the separation distance between the dielectric material and the rubber cover could significantly enhance the charge transfer of the nanogenerator. c) The V_{OC} of the SA-TENG in the single-electrode mode could reach 70 V. a–c) Reproduced with permission.[135] Copyright 2016, The Authors. Distributed under a Creative Commons Attribution NonCommercial License. d) The GO LS-TENG was designed by Wu et al. in 2019.[176] e) The I_{SC} experienced a continuous increase as the GO concentration in the dispersion rose from 0 to 10 mg mL^{-1}. f) Upon tapping with the palm, the GO LS-TENG exhibited notable contact output performance, with a P_R density of 0.50 mW cm^{-2}. d–f) Reproduced with permission.[176] Copyright 2019, Elsevier Ltd. g) The HM-TENG was constructed by Chen et al. in 2019.[177] h) Applying pressure on the dielectric film surface increased elastomer deformation, further enhancing elastomer-dielectric film contact. i) The P_R density of 0.72 mW cm^{-2} was obtained using an external load resistance of 13 MΩ. g–i) Reproduced with permission.[177] Copyright 2019, Elsevier Ltd. j) A fully transparent and stretchable EC-TENG was proposed by Xia et al. in 2021.[178] k) The stronger electrostatic field could be constructed when the electronegativity difference between the dielectric materials was larger, leading to higher performance by the EC-TENG. l) With a matching load of 40 MΩ, it achieved a maximum output power of 0.17 mW cm^{-2}. j–l) Reproduced with permission.[178] Copyright 2021, Elsevier Ltd.

Additionally, applying pressure on the dielectric film surface increased elastomer deformation, further enhancing elastomer-dielectric film contact (Figure 10 h). This strengthens the electrostatic field, leading to higher electrical signals from the HM-TENG. The optimized HM-TENG achieved a V_{OC} of ≈170 V, an I_{SC} density of 12.5 μA cm^{-2}, and a transferred charge (Q_{SC}) density of 24 nC cm^{-2}. Additionally, the P_R density of 0.72 mW cm^{-2} was obtained using an external load resistance of 13 MΩ (Figure 10i). This study highlights the importance of mechanical force in influencing TENG performance and underscores the

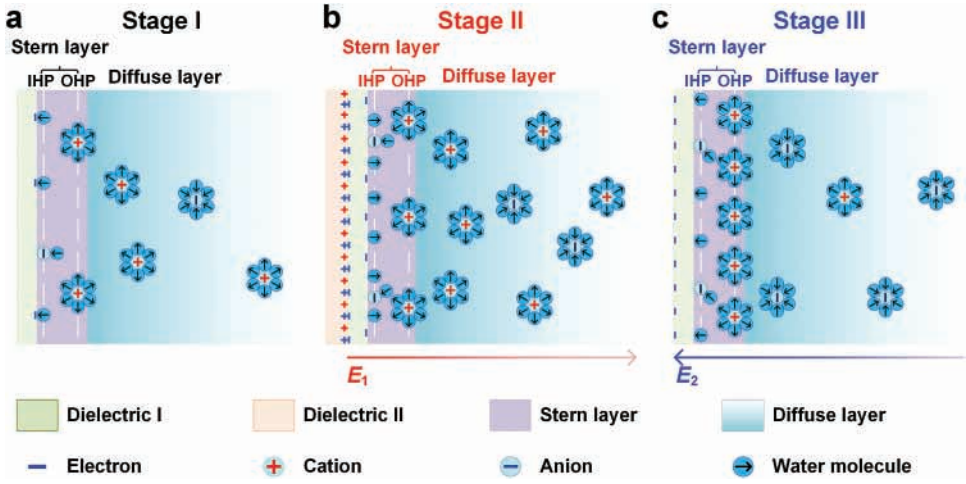

Figure 11. In 2023, a triboiontronics system using bidirectional electrostatic fields via solid-solid CE was developed. a) In Stage I, DI water contacted electronegative dielectric I, forming a stable EDL with a net negative charge. b) Electropositive dielectric material II, precharged with positive charges, induced solid-solid CE with dielectric I, creating a positive electrostatic field in Stage II. c) After removing dielectric II in Stage III, its transferred electrons created a negative electrostatic field, attracting hydrated cations to the solid-liquid interface and leading to a significant number of free anions in the diffuse layer.

need for further research to fully exploit this technology in energy scavenging applications. Additionally, differences in electronic attraction between dielectric materials can affect charge transfer during solid-solid CE, thereby regulating device output performance. In 2021, Xia et al. developed a fully transparent and stretchable triboelectric nanogenerator based on edible grade silica gel and crystal mud (EC-TENG) with ultra-high voltage output, leveraging a significant electronegativity difference,[178] as illustrated in Figure 10j. By selecting different dielectric materials to contact edible grade silica gel and generating solid-solid CE effects, various electrostatic fields were constructed to regulate the EDL at the contact interface between the silica gel and its inner crystal mud, resulting in diverse electrical signals. This investigation aimed to probe the impact of electronegativity difference between dielectric materials on the output performance. Experimental results demonstrated that a stronger electrostatic field could be constructed when the electronegativity difference between the dielectric materials was larger, leading to higher performance by the EC-TENG (Figure 10k). With significant electronegativity contrast, pressing the stretchable EC-TENG with nitrile gloves at a frequency of 5 Hz resulted in I_{SC}, V_{OC}, and Q_{SC} measurements of 25.96 μA, 1400 V, and 150 nC, respectively. With a matching load of 40 MΩ, it achieved a maximum output power of 0.17 mW cm^{-2} (Figure 10l). Introducing the influence of triboelectric sequence in the EC-TENG improved electrical characteristics, enhancing energy scavenging capabilities. Therefore, in energy scavenging devices relying on dynamically regulating the charge distribution in the EDL by unidirectional electrostatic field, incorporating liquid or gel sealing enhanced the flexibility and deformability of these energy scavenging devices, making them more suitable for wearable technology applications aimed at harvesting biomechanical energy or achieving self-powered information flow for monitoring biomechanical motions. Future research could focus on fine-tuning design parameters and exploring diverse applications of this technology within self-powered wearable systems.

3.2.2. Regulating the Charge Distribution in the EDL by Bidirectional Electrostatic Fields

Based on the "two-step" model, the EDL forms an exceptional ionic-electronic coupling interface in iontronics. Iontronics signifies a paradigm shift from traditional electronics, harnessing efficient transfer and exchange of ionic and electric charges at this coupling interface, leading to significantly higher energy efficiency compared to conventional electronics. A notable example is the human brain, serving as a highly integrated iontronic processing unit, consuming only ≈12 W of power. In contrast, constructing a brain-like integrated electronic system would require tens of megawatts.[179] Such contrast underscores the potential of iontronics in revolutionizing energy-efficient technologies and systems. In 2023, we developed a triboiontronics system using bidirectional electrostatic fields via solid-solid CE,[128] as demonstrated in **Figure 11**. This system controlled the distribution of charges in the Stern layer, enabling precise manipulation of charge polarity and ion transport in the diffuse layer. In Stage I, DI water contacted electronegative dielectric I, forming a stable EDL with a net negative charge (Figure 11a). Electropositive dielectric material II, precharged with positive charges, induced solid-solid CE with dielectric I, creating a positive electrostatic field in Stage II (Figure 11b). This facilitated charge transfer, increasing the net negative charge in the Stern layer and enhancing free cation concentration in the diffuse layer. After removing dielectric II in Stage III, its transferred electrons created a negative electrostatic field (Figure 11c), attracting hydrated cations to the solid-liquid interface. This resulted in a Stern layer with a net positive charge, leading to a significant number of free anions in the diffuse layer. Thus, our triboiontronics system effectively regulated charge redistribution in the Stern layer, allowing precise control over charge polarity and ion transport in the diffuse layer.

We further developed a triboiontronic bionic neurologic circuit based on dynamically regulating the EDL using

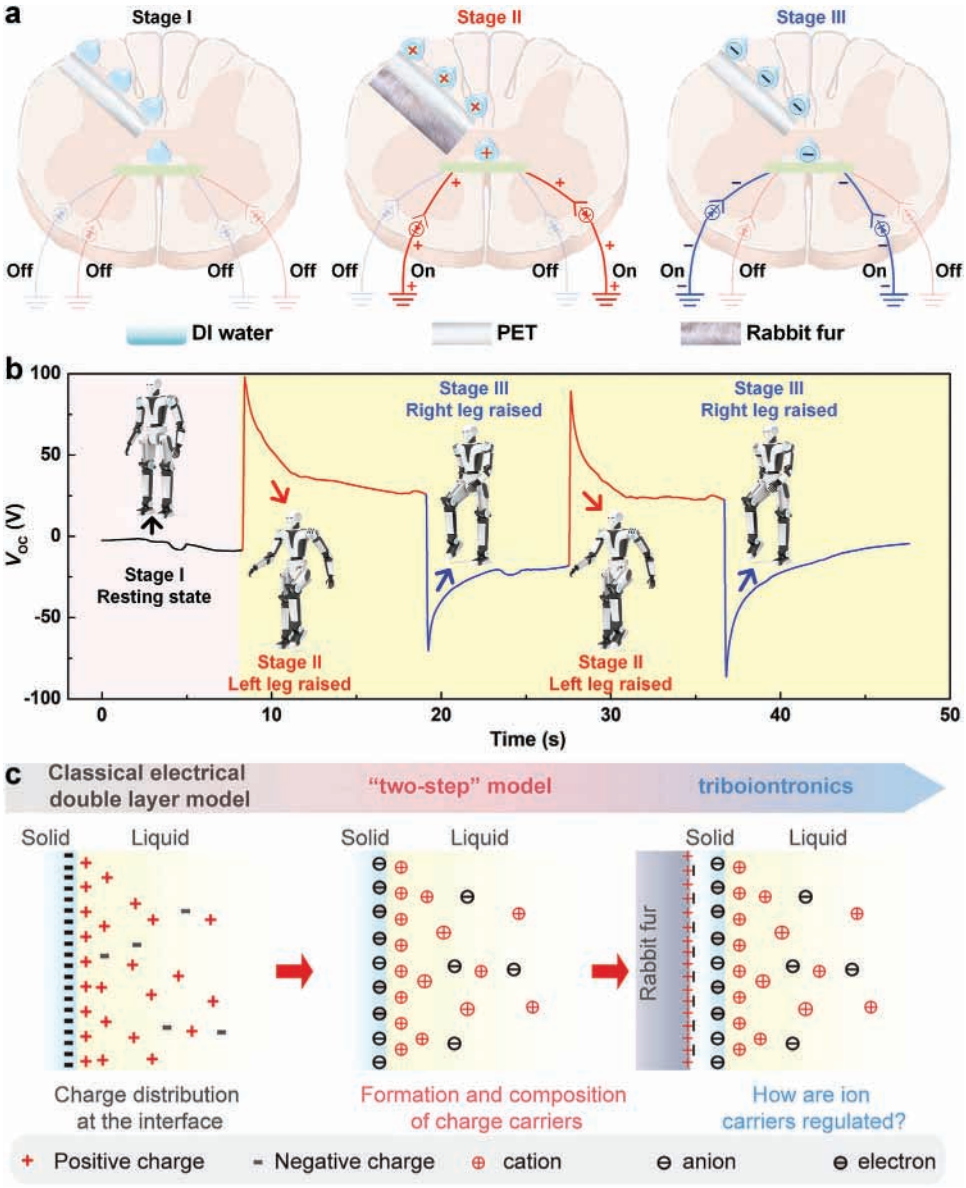

Figure 12. The triboiontronic bionic neurologic circuit was developed in 2023.[128] a) The bionic neurologic circuit was based on dynamically regulating the EDL by bidirectional electrostatic fields. b) The bionic neurologic circuit exhibited potential applications in controlling robots to perform walking movements. Reproduced with permission.[128] Copyright 2023, Elsevier Inc. c) In 2023, Wang et al. emphasized the significance of dynamically regulating the EDL via triboiontronics. Reproduced with permission.[180] Copyright 2023, Elsevier Inc.

bidirectional electrostatic fields,[128] as shown in **Figure 12a**. In Stage I, weak contact CE resulted in fewer free cations, simulating a resting state. In Stage II, positively charged rabbit fur induced numerous cations, generating a positive electronic current. In Stage III, the removal of the rabbit fur induced a reverse electronic current. This circuit regulated ionic charge polarity, conveying tactile contact information without an external power supply. It could control robots for walking movements (Figure 12b). The bionic neurologic circuit initially facilitated the cross-media transmission of physical contact information, encoding them as varying ionic charge polarities within the diffuse layer. Subsequently, these encoded signals were converted into corresponding electronic signals. In contrast to intricate silicon-based chips, the ionic-electronic coupling in triboiontronics provided a straightforward, secure, and efficient interface for human-computer interaction, operating without the need for an external power source. Through the integration of triboiontronic logic circuits endowed with distributed parallel processing capabilities and excellent biocompatibility, efficient information flow could be enabled, including self-powered in-sensor computing systems, implantable neuronal-computer interfaces, and various low-power neuromorphic devices. In 2023, Wang et al. discussed our triboiontronics concept, emphasizing the significance of dynamically regulating the EDL[180] (Figure 12c). They highlighted the consideration of charge generation mechanisms at the solid-liquid interface and

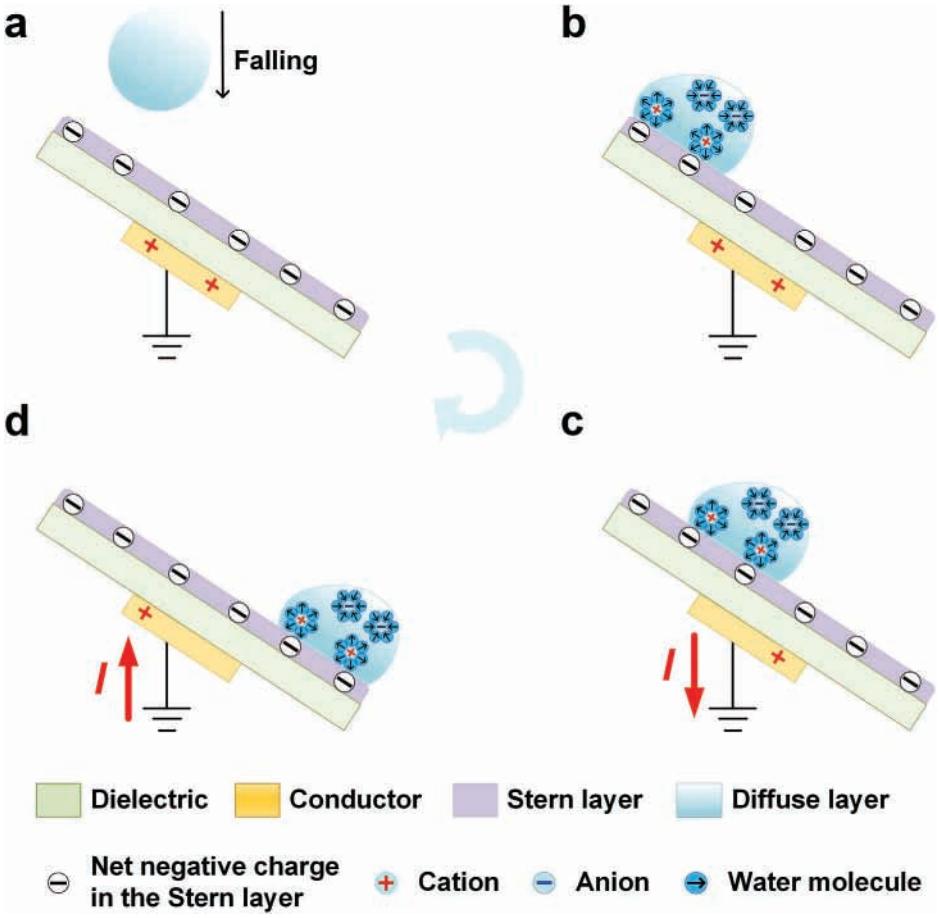

Figure 13. Moving the diffuse layer boundary on the dielectric surface could generate effective AC electrical signals. a) A stable EDL formed upon liquid-dielectric contact, and the Stern layer bearing net negative charges facilitated electron transfer from the charge collecting layer on the rear surface of the dielectric. b) Cations in the droplet migrated toward the Stern layer upon droplet contact, forming a new diffuse layer, while anions moved oppositely. c) As the droplet nears the charge collecting layer, cations could shield the net negative charges in the Stern layer, prompting electron transfer and generating a positive electronic displacement current. d) Upon the departure of cations, the net negative charges in the Stern layer were restored, inducing a reverse electronic displacement current.

demonstrated the close relationship between EDL properties and electrostatic interaction. Dynamically regulating the EDL could bridge ionic-electronic controllable information flow, offering new avenues for applications such as interface control, biosensors, and human-computer interaction, promising to advance triboiontronics across various fields. In the pursuit of energy-scavenging devices that dynamically regulate the entire EDL, the challenge lies in orchestrating directional ionic migration to achieve heightened energy transfer efficiency and precise information dissemination. Central to this objective is the effective manipulation of ionic migration dynamics and precise regulation of ionic flux. Optimizing the design of energy transfer systems holds promise for minimizing energy dissipation and augmenting transmission efficacy. Additionally, the development of high-fidelity sensing and feedback control mechanisms is pivotal for enabling real-time monitoring and regulating of ion migration parameters, thereby enhancing the efficiency and precision of energy transfer processes. Addressing these challenges is crucial for propelling the advancement of next-generation energy harvesting and information processing technologies.

4. Energy Scavenging Devices Based on Dynamic Regulating the Diffuse Layer

4.1. Moving the Diffuse Layer Boundary on the Dielectric Surface

By manipulating the movement of droplets along the initial dielectric surface, the entirety of the EDL boundary can be mobilized, thereby instigating the generation of DC electrical signals. As droplets persist in their movement, the formation of the Stern layer gradually ensues on the dielectric surface. This layer serves as a barrier with a screening effect, curtailing the further transfer of charges at the interface between the solid and liquid phases, consequently diminishing the DC output. However, subsequent to the establishment of a dense Stern layer, the ongoing sliding of droplets prompts the diffuse layer boundary to traverse atop the Stern layer. Consequently, this instigates the production of stable AC electrical signals amid the charge-collecting layers situated on the rear surface of the dielectric, as elucidated in **Figure 13**. Initially, a stable EDL formed upon liquid-dielectric contact. The Stern layer bearing net negative charges facilitated electron transfer from the charge collecting layer on the rear surface of the

dielectric (Figure 13a). Subsequently, cations in the droplet migrated toward the Stern layer upon droplet contact, forming a new diffuse layer, while anions moved oppositely (Figure 13b). As the droplet nears the charge-collecting layer, cations could shield the net negative charges in the Stern layer, prompting electron transfer and generating a positive electronic displacement current (Figure 13c). Upon the departure of cations, the net negative charges in the Stern layer were restored, inducing a reverse electronic displacement current (Figure 13d). Manipulating the diffuse layer boundary optimized AC electrical signal generation, offering the potential for enhanced efficiency and functionality in energy scavenging devices.

By exploring the influencing factors of the diffuse layer boundary movement and optimizing its manipulation, significant advancements can be achieved. Lin et al. introduced the first solid-liquid triboelectric nanogenerator (SL-TENG) in 2013,[101] employing PDMS as the dielectric material as shown in **Figure 14a**. Upon full contact between PDMS and water, a stable EDL formed at the interface. As the two dielectric materials were separated, the Stern layer continuously generated net negative charges, driving cations and anions oppositely within the water. This induced effective AC electrical signals through repeated electron transfers in the external circuit between the charge collecting layers. Initial experimental exploration focused on the effect of the liquid type on output performance (Figure 14b). An increase in ethanol percentage reduced electron transfer effectiveness and ionic content, leading to decreased net charge density in the Stern layer and reduced output performance. Modifying the PDMS surface microstructure increased the solid-liquid contact area, promoting charge transfer and enhancing the output efficiency of the SL-TENG. Under optimal parameters, it generated ≈80 V V_{OC} and 0.25 μA cm^{-2} I_{SC} at a 5 Hz operating frequency (Figure 14c), achieving a P_R density of 5 μW cm^{-2} with an 88 MΩ load resistance. To enhance ocean or water wave energy harvesting, You et al. developed a single electrode mode SL-TENG in 2021,[138] as displayed in Figure 14d. Investigating the effects of solid-liquid contact area and relative motion speed on device performance revealed that increasing the contact area between the dielectric material (PTFE film) and water enhanced V_{OC} generation (Figure 14e). This expansion of the electrostatic field modulation range attracted more cations, enhancing LS-TENG electrical signals. Additionally, higher relative sliding velocities between the PTFE film and water boosted V_{OC} generation (Figure 14f) by intensifying impacts between solid and liquid materials, increasing microscopic contact area and promoting directional ion migration. Optimizing these factors enabled the single electrode mode LS-TENG to achieve ≈400 V V_{OC}, demonstrating effective ocean or water wave energy harvesting potential.

While water wave energy has received significant attention, the largely unexplored potential of raindrop kinetic energy offers a promising avenue for sustainable energy development. In 2014, Lin et al. introduced a droplet-driven LS-TENG to efficiently harvest energy from raindrops,[181] as displayed in Figure 14g. The electrostatic field on the PTFE surface was harnessed to drive the directional migration of free ions within the droplets, thus inducing effective AC electrical signals. By regulating the droplet height, the contact area between the droplet and the PTFE film could be increased to enhance the charge carried by the droplet and consequently improve the output performance (Figure 14h). A single drop of 30 μL of liquid sliding through the PTFE surface generated a V_{OC} of 9.3 V and an I_{SC} of 17 μA (Figure 14i), and the P_R density was 9.1 μW cm^{-2}. These findings underscored the significant potential of the droplet-driven LS-TENG for harvesting energy from liquid droplet motion, pioneering the utilization of droplets for power generation. To further enhance the kinetic energy scavenging of droplets such as raindrops, the droplet-based electricity generator was designed by Xu et al. in 2020,[139] as illustrated in Figure 14j. As droplets hit the PTFE surface, they spread and contact the aluminum (Al) charge collecting layer, converting interfacial effects into bulk effects. This drove transient electron transfer between the Al and indium tin oxide (ITO) in the external circuit, generating an efficient positive current. As droplets flowed through the Al layer, a reverse electron flow in the external circuit generated a low-amplitude current output. Exploiting the bulk effect, the generator achieved a V_{OC} and I_{SC} of ≈143.5 V and 270 μA, respectively (Figure 14k), significantly higher than the single-electrode mode generator without the Al electrode. Under a load resistance of 332.0 kΩ, its P_R density reaches 5.01 mW cm^{-2}, three orders of magnitude above the single-electrode mode generator. In 2023, Li et al. developed a high-voltage generator to explore the mechanism behind ultra-high power density output,[182] as demonstrated in Figure 14l. They found that the significant enhancement resulted from directional ionic migration in the droplet driven by the electrostatic field of the Stern layer in the EDL. This induced rapid electron transfer between charge collecting layers upon droplet contact, yielding efficient positive current output. Subsequent droplet flow generated a low-amplitude reverse current. Fine-tuning contact dynamics and optimizing circuit design enabled the generator to reach a V_{OC} of 1200 V, showcasing efficient power harnessing by manipulating the diffuse layer boundary on the dense Stern layer. The aforementioned investigations were rooted in the dynamic modulation of the diffuse layer in a stable EDL. In 2024, we embarked on an innovative exploration delving into the influence of the EDL formation process on charge transfer dynamics between ice and dielectric materials during solid-liquid phase transitions4,[183] as shown in Figure 14m. Before the melting, electron transfer predominated within solid-solid contacts. The emergence of micro-droplets during the initial melting of ice amplified material contact areas, leading to a six-fold enhancement in charge transfer (Figure 14n). As ice undergoes partial melting, macroscopic droplets might condense on surfaces, establishing solid-liquid contacts with dielectric materials. Concurrently, the EDL began forming, effectively screening the dielectric material's surface charge, with output current primarily driven by diffuse layer charges. Upon complete ice melting into water, the stable EDL provided robust screening effects, resulting in minimal charge transfer levels. These findings offered valuable insights into understanding substance interactions and charge transfer dynamics within dynamic phase transition scenarios.

4.2. Dynamically Regulating the Charge Density in the Diffuse Layer

The output performance of energy scavenging devices, reliant on dynamically regulating the EDL, is intricately tied to the charge density of directional migration. Thus, increasing the

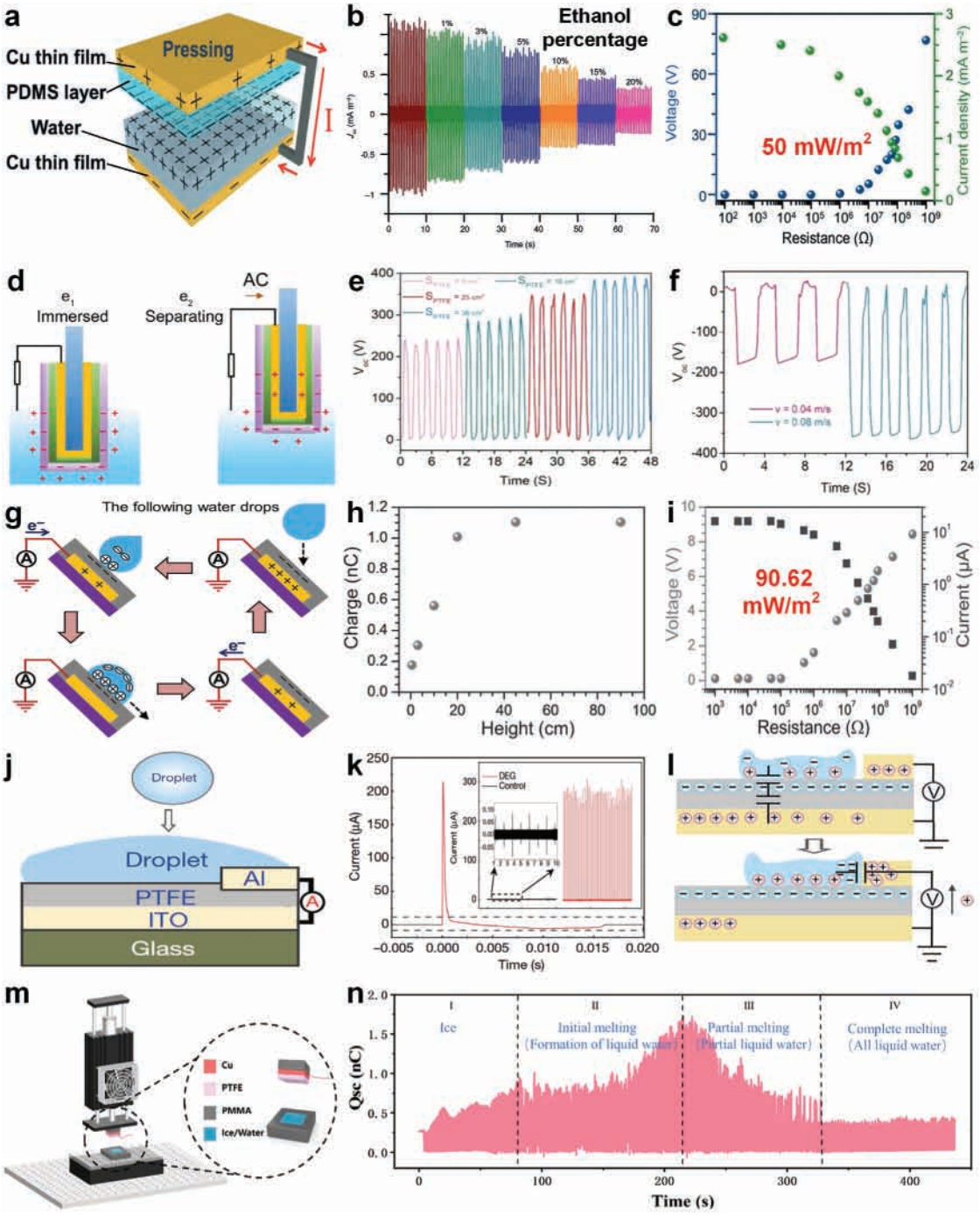

Figure 14. The energy scavenging devices were developed based on moving the diffuse layer boundary on the dielectric surface. a) The first SL-TENG was introduced by Lin et al. in 2013.[101] b) The effect of the liquid type on the SL-TENG output was studied. c) The LS-TENG could achieve a P_R density of 5 μW cm^{-2} at an operating frequency of 5 Hz. a–c) Reproduced with permission. Copyright 2013, Wiley-VCH. d) The single-electrode mode SL-TENG was developed by You et al. in 2021.[138] e) Increasing the solid-liquid contact area could effectively enhance the generated output. f) Increasing the solid-liquid relative sliding velocity also could boost the output of the SL-TENG. d–f) Reproduced with permission.[138] Copyright 2021, American Chemical Society. g) A droplet-driven LS-TENG to efficiently harvest energy from raindrops was introduced by Lin et al. in 2014.[181] h) By regulating the droplet height, the LS-TENG output could be improved. i) A single drop of 30 μL could generate a P_R density of 9.1 μW cm^{-2}. Reproduced with permission.[181] Copyright 2014, Wiley-VCH. j) The droplet-based electricity generator with high instantaneous power density was designed by Xu et al. in 2020.[139] k) The I_{SC} could reach 270 μA. j,k) Reproduced with permission.[139] Copyright 2020, Springer Nature. l) The mechanism of ultra-high power density output was developed by Li et al. in 2023. Reproduced with permission.[182] Copyright 2023, American Association for the Advancement of Science. Distributed under a Creative Commons Attribution NonCommercial License 4.0. m) The influence of the EDL formation process on charge transfer dynamics between ice and dielectric materials during solid-liquid phase transitions was explored in 2024.[183] n) In the process of phase transition, the charge transfer between ice and dielectric materials. m,n) Reproduced with permission.[183] Copyright 2024, Elsevier Ltd.

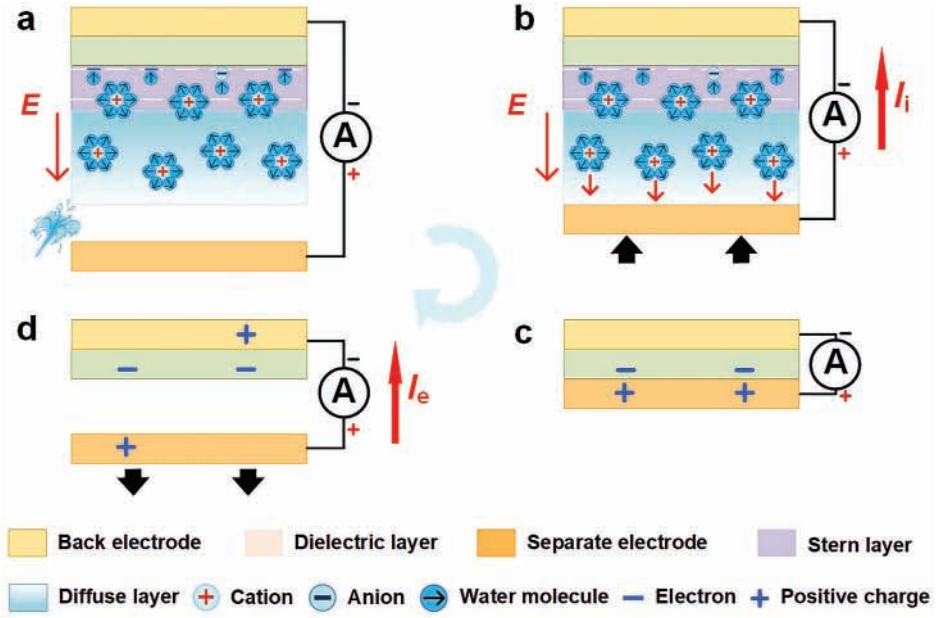

Figure 15. Dynamically regulating the charge density in the diffuse layer by solid-solid CE could generate a DC ionic-electronic coupling output.[128] a) DI water formed a stable EDL on the dielectric surface with low diffuse layer charge density. Positively charged DI water mist, generated via solid-liquid CE, regulated cation charge density, creating a positive electric field on the dielectric surface. b) Upon contact with a separate electrode, positive charges migrated, inducing electron transfer and forming an effective ionic current. c) Subsequent solid-solid CE between the dielectric layer and separate electrode facilitated electron transfer, driven by electrostatic induction. d) As the dielectric layer moved away, negative charges induced electron flow, generating an electronic displacement current in the external circuit.

ionic charge density presents an effective strategy for enhancing device performance. In pursuit of efficient DC output, we explored a dynamic regulation method utilizing solid-solid CE to control the ionic charge density within the diffuse layer,[128] as depicted in **Figure 15**. Initially, DI water formed a stable EDL on the dielectric surface with low diffuse layer charge density. Positively charged DI water mist, generated via solid-liquid CE, regulated cation charge density, creating a positive electric field on the dielectric surface (Figure 15a). Upon contact with a separate electrode, positive charges migrated, inducing electron transfer and forming an effective ionic current (Figure 15b). Subsequent solid-solid CE between the dielectric layer and separate electrode facilitated electron transfer, driven by electrostatic induction (Figure 15c). As the dielectric layer moved away, negative charges induced electron flow, generating an electronic displacement current in the external circuit (Figure 15d). This process, repeated with each cycle of DI water mist application, demonstrated that dynamically regulating diffuse layer charge density via solid-solid CE could produce a DC ionic-electronic coupling output.

We introduced the Direct-Current Triboiontronic Nanogenerator (DC-TING)[128] in 2023 to dynamically regulate charge density in the diffuse layer, producing DC ionic-electronic coupling output, as depicted in **Figure 16**a. Initially functioning as a conventional TENG, it generated 0.8 μA AC electrical signal at 1 Hz (Figure 16b). Upon spraying charged DI water mist, it transitioned into producing stable 6.0 μA DC output. Longer replenishment times at lower frequencies increased current output (Figure 16c). The studies demonstrated that treating the micro surface morphology of the dielectric through micro-engraving could effectively increase its specific surface area. The presence of air within the microstructure could hinder solid-liquid contact, leading to a reduction in the hydrophilicity of the dielectric surface (Figure 16d,e). Combining strategies maintained optimal charge density, ensuring consistent and efficient DC output. I_{SC} density and Q_{SC} density reached 36 μA cm^{-2} (Figure 16f) and 560 nC cm^{-2} (Figure 16g), respectively. with a remarkable P_R density of 12.64 mW cm^{-2} (Figure 16h), several orders of magnitude over conventional solid-liquid TENGs. These findings underscored the significance of optimal charge density for maximizing TENG efficiency, offering the potential for enhanced energy scavenging technologies. Concerning energy scavenging devices that hinge on dynamically regulating the diffuse layer, a pivotal constraint hindering their widespread adoption in energy harvesting and information dissemination domains is the diminished transferred charge density resulting from increased internal resistance attributed to the dielectric material. Consequently, endeavors in research and development should prioritize materials characterized by reduced internal resistance, including those with enhanced conductivity or diminished resistivity. Furthermore, optimizing the choice of dielectric materials and enhancing electrode materials could further enhance charge transfer efficiency.

5. Energy Scavenging Devices Based on Regulating the Debye Length Range

5.1. Migration of Ions Driven by Different Driving Forces

5.1.1. Migrating of Ions Driven by Functional Group Hydrolysis

Hydrolysis of surface functional groups releases ions into the surrounding liquid, forming an EDL near the solid surface. The

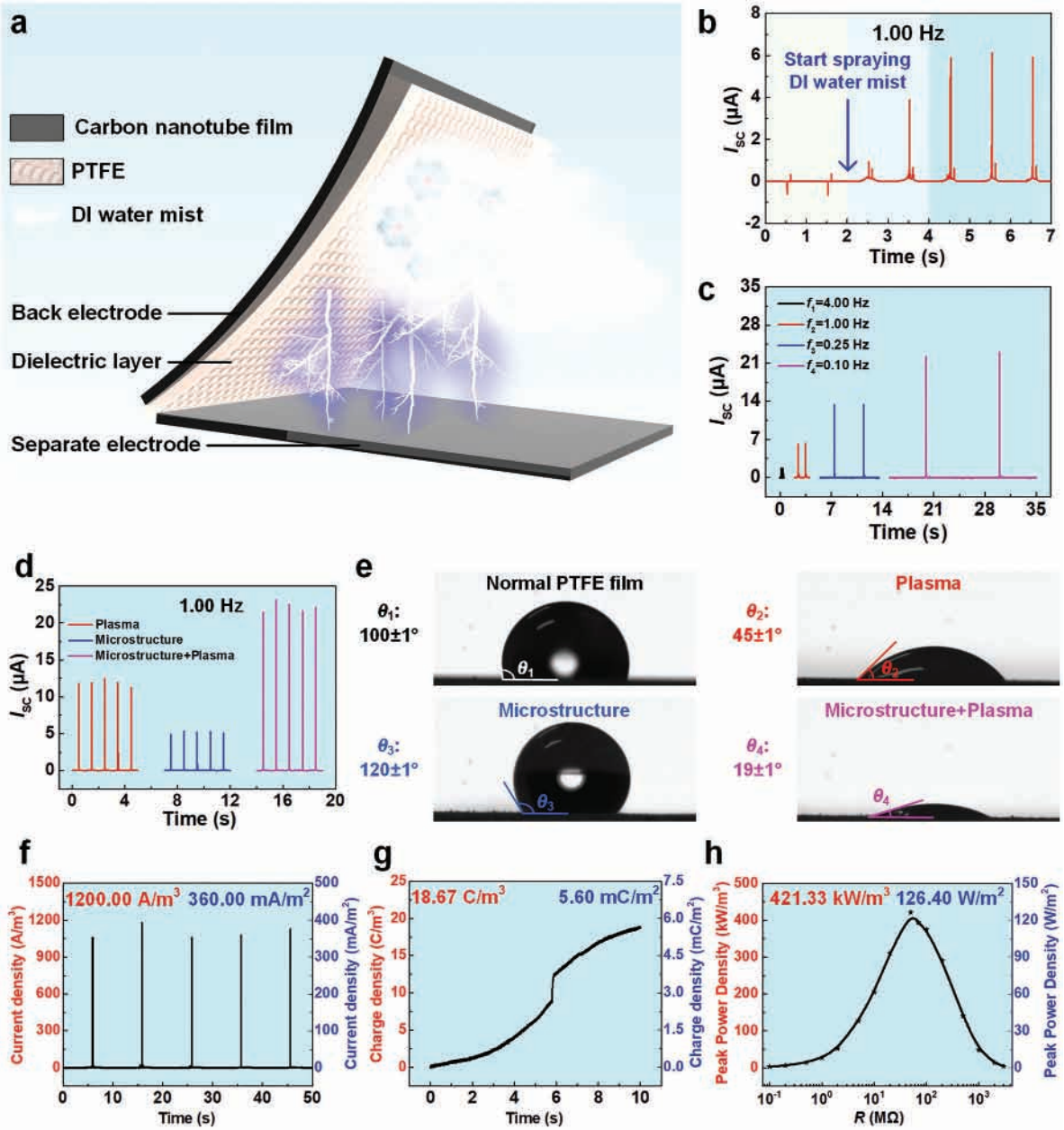

Figure 16. Based on dynamic regulating the charge density in the diffuse layer, the DC-TING was developed in 2023.[128] a) Schematic diagram of the DC-TING. b) The DC-TING could produce DC ionic-electronic coupling output by regulating the charge density in the diffuse layer in EDL on the dielectric surface. c) With lower operating frequencies, a longer replenishment time allowed for the accumulation of more charge in the diffuse layer. thereby resulting in higher current output. d) The comprehensive treatment of micro-engraving and plasma could effectively improve the hydrophilicity of the dielectric surface and thus effectively improve the DC-TING output. e) The contact angle of DI water droplets on the dielectric surface after different treatments. f) By employing the combination of charge replenishment strategies, the I_{SC} density could reach 36 μA cm^{-2}. g) The Q_{SC} density of the DC-TING could reach 560 nC cm^{-2}. h) The P_R density of the DC-TING could reach 12.64 mW cm^{-2}, which was several orders of magnitude over conventional solid-liquid TENGs. a–h) Reproduced with permission.[128] Copyright 2023, Elsevier Inc.

Debye length, determined by solution properties, dictates the distance of significant electrostatic interactions between ions. In nanochannels with charged surfaces, ions within the Debye length experience strong electrostatic forces. By establishing a concentration gradient along the nanochannel, ions can be directionally driven within the Debye length, generating electrical energy output. **Figure 17** illustrates the mechanism of inducing constant current output by controlling functional group distribution in the nanochannel (Figure 17a) to create an ionic concentration gradient. Upon liquid entry into the nanochannel, the hydrolysis of functional groups initiates, releasing ions within the Debye length and forming the EDL near the surface (Figure 17b). A concentration gradient of ions ensues, driving directional ion migration toward regions of lower concentration within the

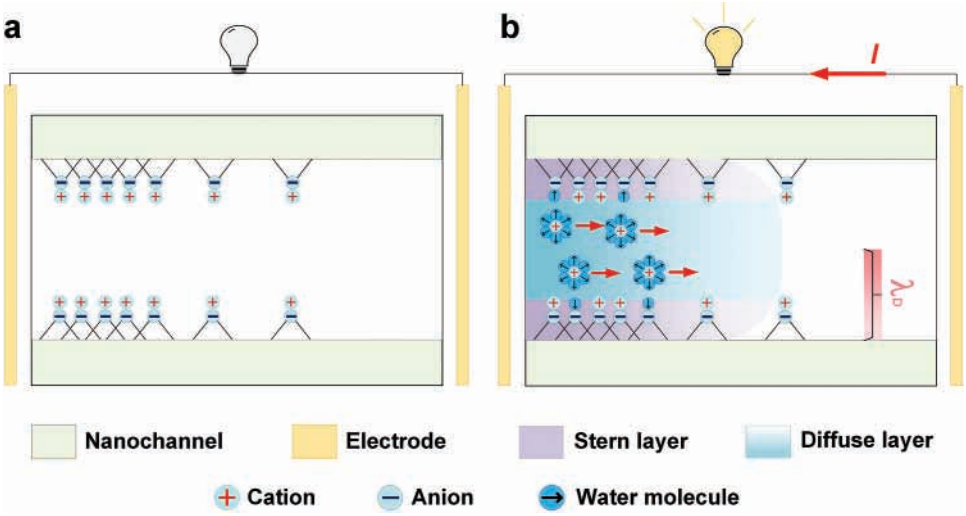

Figure 17. The constant current output could be induced by controlling functional group distribution in the nanochannel to create an ionic concentration gradient. a) The functional group distribution was controlled in the nanochannel. b) Upon liquid entry into the nanochannel, the hydrolysis of functional groups initiates, releasing ions within the Debye length and forming the EDL near the surface.

Debye length. This migration generates a potential difference, facilitating electron transfer in the external circuit, and thereby, a constant current. This method holds great potential for sustainable energy scavenging.

Zhao et al. developed the moisture-enabled electric generator (MEG) in 2016,[184] utilizing a GO framework as shown in **Figure 18a**. The GO membrane, rich in hydrophilic oxygen-containing groups, reacted with water vapor to release H^+ ions, driving electrical current generation through internal nanochannels. Investigating the impact of GO membrane thickness revealed that optimal power output was achieved with a thickness of 50 µm (Figure 18b). Additionally, the effect of GO membrane area showed that while larger areas enhanced water adsorption and output current, excessive decrease in membrane resistivity due to hydration limited further power increase, leading to stabilized output (Figure 18c). Through optimization, the MEG achieved impressive performance, with an average power (P_A) density of ≈1 mW cm^{-2} and an energy scavenging efficiency of ≈52% at 75% relative humidity (RH). Shao et al. further introduced the wearable fiber-form hygroelectric generator (WF-HG) in 2018[185] as depicted in Figure 18d, featuring a unique long-axis structure that enhances shape adaptability and broadens application scope. The WF-HG demonstrated a notable I_{SC} density of ≈0.75 µA per centimeter at 70% RH (Figure 18e), with the ability for convenient amplification through simple series/parallel connections (Figure 18f). Its compatibility with textiles enhanced durability and portability, offering stronger wearability and portability for electronic devices. In most concentration-gradient-driven energy scavenging devices utilizing hydrolysis of functional groups, monovalent ionic charge carriers like H^+ were commonly employed. To enhance output performance, Chen et al. introduced a moisture-enabled electric generator with high-valent metal carrier transport (HMC-EMG) in 2019,[186] as displayed in Figure 18g. They developed a 1D hydrophilic conductive polymer nanoarray, doping it with high-valence metal cations like Mg^{2+} and Al^{3+} to enhance charge transportation capacity (Figure 18h). The HMC-EMG achieved a volumetric P_R density of 40 mW cm^{-3} using Al^{3+} as the charge carrier (Figure 18i). Wang et al. proposed a heterogeneous moist-electric generator (HMEG) in 2021[141] as illustrated in Figure 18j, employing a dual-layer polyelectrolyte membrane. The membrane induced reverse co-migration of ions with opposite polarities, enhancing the volumetric P_A density to 0.9 µW cm^{-3} (Figure 18k). The integrated soft HMEG device in series could provide more than 1 kV V_{OC} (Figure 18l), which made it highly promising for applications in high-voltage fields.

5.1.2. Migrating of Ions Driven by Evaporation

Constant current output in energy scavenging devices can arise through two mechanisms: ionic concentration gradients from hydrolyzed functional groups and liquid flow carrying a net charge. After hydrolysis, the inner surface of the nanochannel carried a specific polarity as depicted in **Figure 19a**, determining ion-selective membrane characteristics. Evaporation drove liquid into the nanochannels, where surface charge repels like-charged ions and attracts oppositely charged ions, forming an EDL (Figure 21b). These charges migrated within the Debye length range as liquid flows, resulting in constant current output. This ionic selectivity enhanced output reliability.

Utilizing evaporation-induced ionic migration within the Debye length range of the EDL, innovative energy scavenging devices have emerged. In 2017, Ding et al. devised an evaporation-driven generator inspired by plant transpiration,[187] employing a fully printed porous carbon film as shown in **Figure 20a**. Evaporation propelled liquid through the film, leading to hydrolysis of surface functional groups and acquiring a negative charge, impeding anion entry and prompting upward water movement, inducing current generation. They proposed a control strategy regulating liquid evaporation efficiency via airflow velocity control(Figure 20b), achieving a reliable V_{OC} of 1 V and volumetric P_A density of 8.1 µW cm^{-3} (Figure 20c). This generator could hold the potential for eco-friendly, self-powered devices. To boost

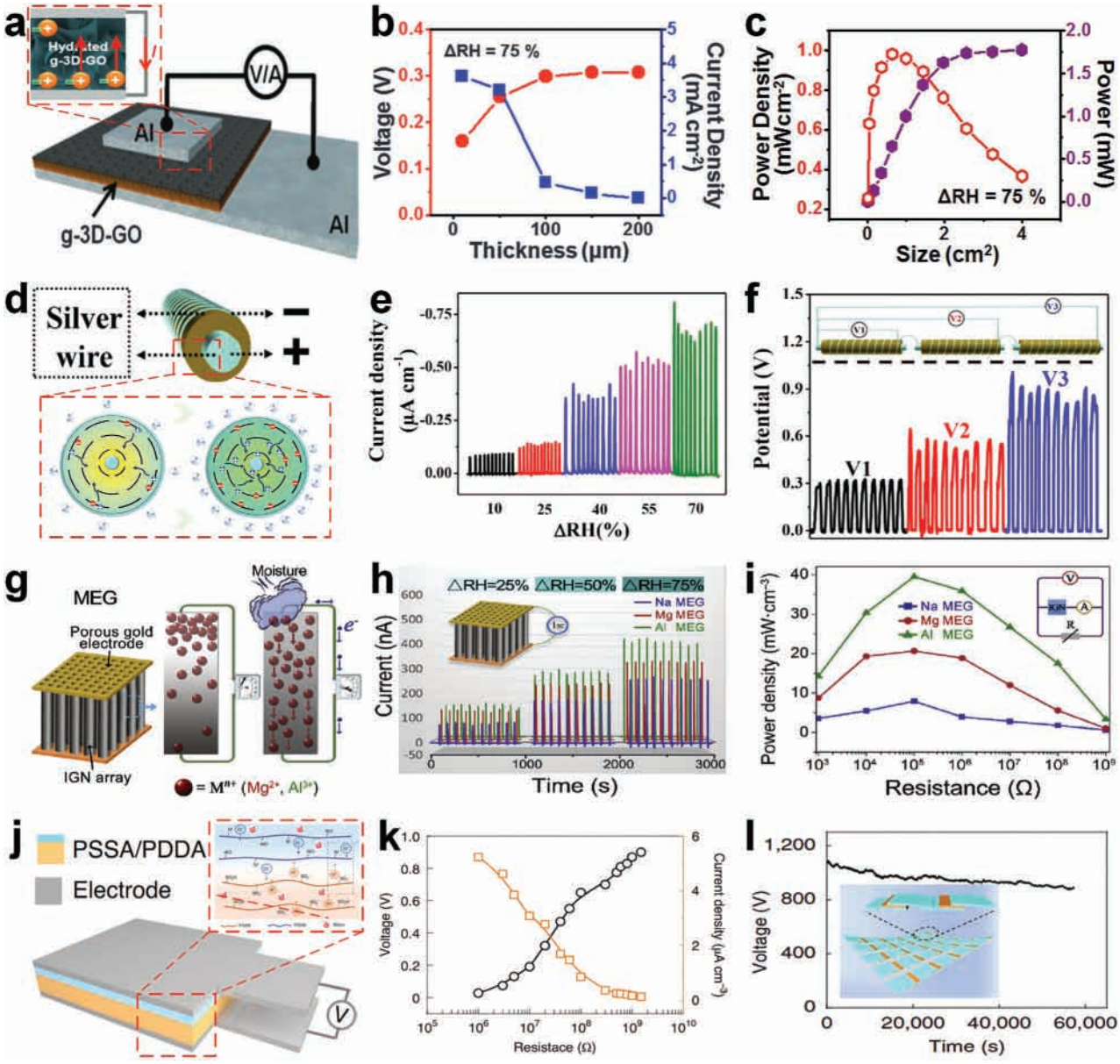

Figure 18. Energy scavenging devices were developed based on the migrating of ions driven by functional group hydrolysis. a) The MEG using a GO framework was designed by Zhao et al. in 2016.[184] b) The optimal power output was achieved with a thickness of 50 μm. c) The MEG achieved a P_A density of ≈1 mW cm^{-12}. a–c) Reproduced with permission.[184] Copyright 2024, Royal Society of Chemistry. d) The WF-HG was introduced by Shao et al. in 2018.[185] e) The WF-HG demonstrated a notable I_{SC} density of ≈0.75 μA per centimeter at 70% RH. f) Its output could be amplified by a simple series/parallel connection. d–f) Reproduced with permission.[185] Copyright 2018, Elsevier Ltd. g) A novel HMC-EMG was proposed by et al. in 2019.[186] h) The doping of high-valent metal cations in the conductive polymer could enhance the charge transport capacity. i) The HMC-EMG achieved a volumetric P_R density of 40 mW cm^{-3} using Al^{3+} as the charge carrier. g–i) Reproduced with permission.[186] Copyright 2019, Elsevier Ltd. j) The HMEG was proposed by Wang et al. in 2021.[141] k) The volumetric P_A density could reach 0.9 μW cm^{-3} of the HMEG. l) Soft HMEG devices in series could provide more than 1 kV V_{OC}. j–l) Reproduced with permission.[141] Copyright 2021, Springer Nature.

high voltage output and broaden applications, Li et al. designed an evaporation-driven water flow nanogenerator in 2019 using flexible carbon nanoparticle film,[188] as depicted in Figure 20d. By regulating the Zeta potential of carbon nanoparticles through surface functional group manipulation, they controlled the polarity and charge density of surface functional groups post-hydrolysis. Liquid flow through the nanochannel resulted in observable changes in the current output direction due to migration charge polarity (Figure 20e). By employing modified carbon films with opposite surface charges, they achieved counter-directional synergistic diffusion of anions and cations, significantly enhancing generator performance. This allowed a 5 cm × 5 cm dual-film generator to generate a maximum V_{OC} of 5 V and an I_{SC} of 1.5 μA (Figure 20f).

To boost power density, Yun et al. introduced an evaporation-driven generator based on an ion-permselective

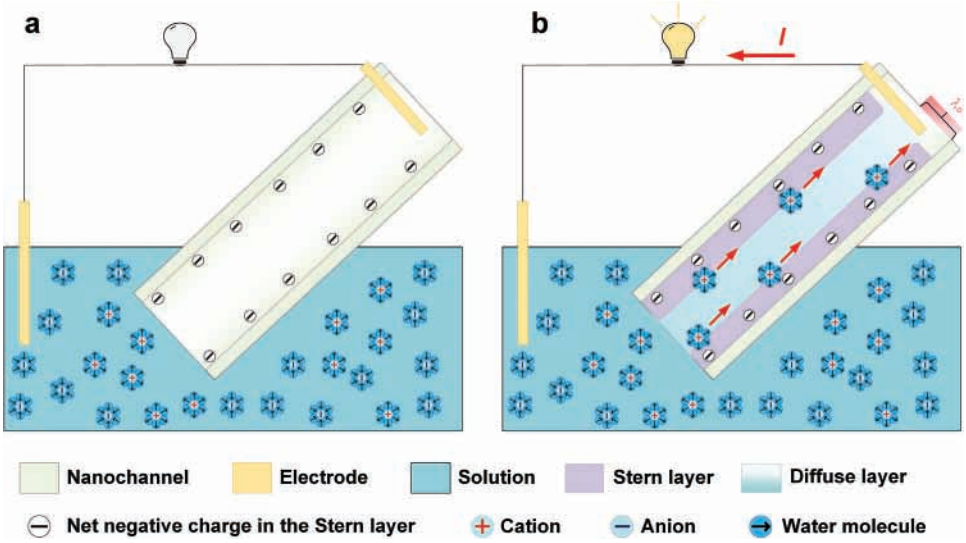

Figure 19. The constant current output could be generated by the migrating of ions driven by evaporation. a) After hydrolysis, the inner surface of the nanochannel carried a specific polarity, determining ion-selective membrane characteristics. b) Evaporation drove liquid into the nanochannels, where surface charge repels like-charged ions and attracts oppositely charged ions, migrating within the Debye length range as liquid flows and resulting in constant current output.

conducting polymer in 2022,[189] as displayed in Figure 20g. In the conductive polymer of poly(3,4-ethylenedioxythiophene):poly(styrenesulfonate) (PEDOT:PSS), the sulfonic acid groups and hydroxyl groups in the cellulose membrane synergistically rendered the polymer surface negatively charged after hydrolysis, which led to the adsorption of more cations into the polymer matrix, thereby demonstrating excellent cation permeability selectivity (Figure 20h). The internal resistance was reduced by leveraging PEDOT:PSS conductivity, maximizing generator performance. Simulation results highlighted that decreasing ionic diameter enhanced power generation (Figure 20i), with the generator achieving a high P_A density of 0.45 μW cm^{-2} from seawater evaporation. Addressing low power output, Zhang et al. developed a flexible fabric hydrovoltaic generator in 2023,[190] as illustrated in Figure 20j. Through optimized structure and material selection, the generator harnessed the ionic concentration gradient and ion-selective action, promoting orderly ion flow (Figure 20k). This design achieved a V_{OC} of ≈0.25 V, an I_{SC} output of ≈520 μA, and a P_A density of 2.08 μW cm^{-2} in simulated seawater (Figure 20l).

5.1.3. Migrating of Ions Driven by Salinity Gradient

In addition to evaporation, exploiting salinity gradients for ionic migration within the Debye length range in the EDL can significantly enhance output performance, as demonstrated in **Figure 21**. When separated by an ion-selective membrane, salinity gradients drive ions from high to low concentration, generating osmotic power until equilibrium (Figure 21a). Specific polar charges in the membrane attract ions into nanochannels, forming an EDL, which rapidly migrates within the Debye length range due to the salinity gradient, inducing constant current generation (Figure 21b). This efficient scavenging of osmotic energy from salinity gradients offers superior output compared to liquid evaporation-based generators.

In the energy scavenging device leveraging ion migration within the Debye length range, improving ion migration speed is crucial for enhancing output performance. Siria et al. utilized boron nitride nanotubes to construct single nanochannels in 2013,[110] scavenging osmotic energy from salt solutions with different concentrations as shown in **Figure 22**a. Increasing the ionic concentration ratio between solutions effectively improved the I_{SC} of the device, demonstrating its sensitivity to salinity gradients (Figure 22b). Moreover, higher pH levels enhanced negative surface charge accumulation, accelerating cation migration rates and boosting device performance. With optimization, the device achieved a P_A density of 0.4 W cm^{-2} (Figure 22c). In 2016, Feng et al. explored a single-layer MoS_2 nanopore for osmotic energy scavenging,[191] as depicted in Figure 22d. Increasing the ionic concentration ratio improved both V_{OC} and I_{SC}, enhancing device performance (Figure 22e). Additionally, they found that decreasing nanopore diameter improved ion selectivity and increased I_{SC}, with a peak power density of 100 W cm^{-2} achieved at a 10 nm diameter (Figure 22f). These advancements highlight innovative strategies for efficient osmotic power generation, paving the way for ocean energy resource utilization.

To address scalability challenges in osmotic power generation, Zhu et al. (2018) introduced a Janus 3D porous membrane-based device,[142] as displayed in Figure 22g. This membrane, composed of negatively charged hexasulfonated poly(aryl ether ketone)s (PAEK-HS) and positively charged poly(ether sulfone)s with pyridine pendants (PES-Py), prevented reverse current flow, enhancing efficiency (Figure 22h). Through tailored porosity and surface charge density, achieved via chemical design, effective ionic selectivity was ensured. At salinity gradients of 50 and 500 times between seawater and freshwater, the generator achieved P_A densities of 0.27 and 0.51 mW cm^{-2}, respectively (Figure 22i). Ren et al. (2022) developed a more efficient

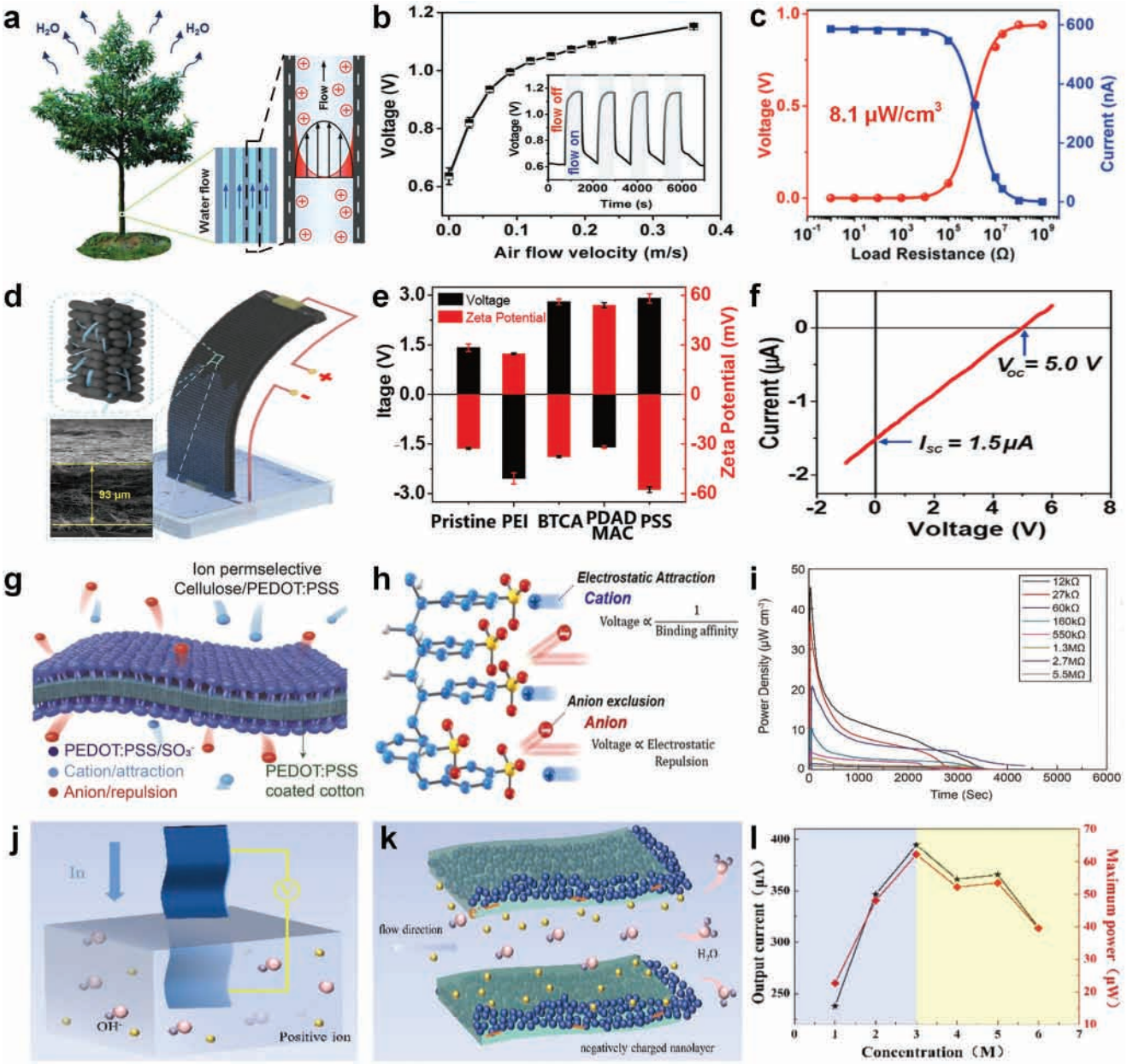

Figure 20. Energy scavenging devices were developed based on the migrating of ions driven by evaporation. a) The evaporation-driven generator was developed by Ding et al. in 2017.[187] b) By promoting the evaporation of the liquid, the output could be controlled. c) The volumetric P_A density could reach 8.1 μW cm^{-3}. a–c) Reproduced with permission.[187] Copyright 2017, Wiley-VCH. d) An evaporation-driven water flow nanogenerator using flexible carbon nanoparticle film was designed by Li et al. in 2019.[188] e) Liquid flow through the nanochannel resulted in observable changes in the current output direction due to migration charge polarity. f) A 5 cm × 5 cm dual-film generator could generate a maximum V_{OC} of 5 V and an I_{SC} of 1.5 μA. d–f) Reproduced with permission.[188] Copyright 2019, Elsevier Ltd. g) The evaporation-driven generator was proposed by Yun et al. in 2022.[189] h) In the PEDOT:PSS conductive polymer, the sulfonic acid groups and hydroxyl groups in the cellulose membrane synergistically rendered the polymer surface negatively charged after hydrolysis, which led to excellent cation permeability selectivity. i) The generator achieved a P_A density of 0.45 μW cm^{-2} driven by seawater evaporation. g–i) Reproduced with permission.[189] Copyright 2022 Elsevier Ltd. j) A flexible fabric hydrovoltaic generator was developed in 2023.[190] k) The generator harnessed the ionic concentration gradient and ion-selective action, promoting orderly ion flow. l) The optimized generator achieved an P_A density of 2.08 μW cm^{-2}. j–l) Reproduced with permission.[190] Copyright 2024, Royal Society of Chemistry.

osmotic energy scavenging device by leveraging the photothermal effect,[192] as depicted in Figure 22j. Nanoparticles introduced into the electrolyte solution enhanced the micro EDLs at the nanoparticle-aqueous solution interface, increasing space charge density and ionic selectivity of the nanofluidic channel. With a 10% volume fraction of nanoparticles in the nanochannel, the theoretical permeation output power at a 50 times salinity gradient increased by 43.1% (Figure 22k). Additionally, experiments showed that osmotic energy scavenging efficiency depended on water solution temperature, influencing ionic

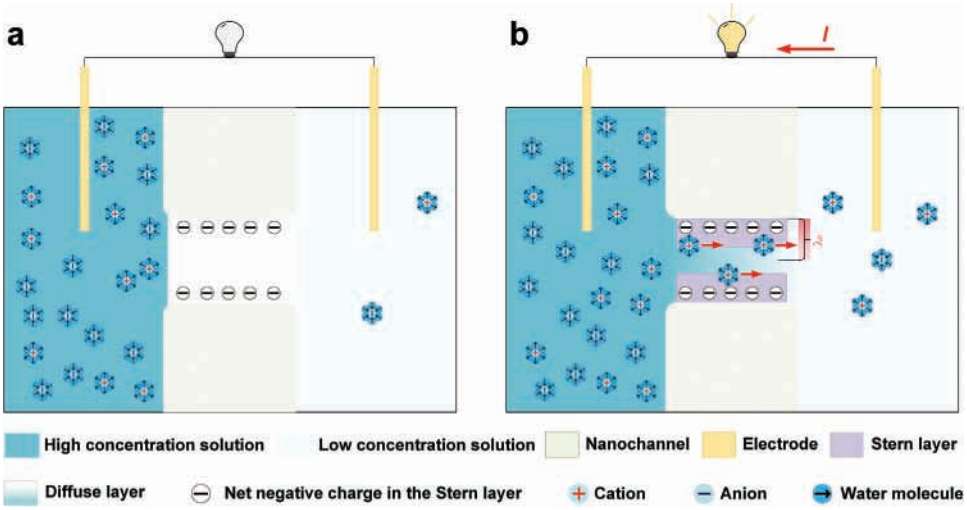

Figure 21. Exploiting salinity gradients for ionic migration within the Debye length range in the EDL can significantly enhance output performance. a) When separated by an ion-selective membrane, salinity gradients drive ions from high to low concentration, generating osmotic power until equilibrium. b) Specific polar charges in the membrane attract ions into nanochannels, forming an EDL, which rapidly migrates within the Debye length range due to the salinity gradient, inducing constant current generation.

migration rate and surface charge density in nanofluidic channels. The photothermal effect of nanoparticles significantly raised the solution temperature, accelerating ionic flow. Even with just a 1% mass fraction of silver (Ag) nanoparticles in NaCl water solution, the temperature rose from 297.2 to 340.9 K. With nanoparticle enhancement and the photothermal effect synergistically, under a 50 times salinity gradient between artificial seawater and freshwater, the P_A density effectively increased from 0.24 to 0.84 mW cm^{-2} (Figure 22l). In 2022, Hao et al. introduced a salt-adaptive sandwich-structured membrane to address the limitations of traditional ion-selective membranes under high ionic conditions,[193] as shown in Figure 22m. This innovative membrane allowed ions with different polar charges to transport in opposite directions within the nanochannels, generating high-efficiency electric current. By regulating the ionic concentration, the nanochannel system could rapidly switch pore morphology, transitioning from 1D straight nanochannels to 3D network pores. This alteration significantly reduced pore size, increased pore density, and boosted charge density by three orders of magnitude. Consequently, the I_{SC} continued to rise with time during the initial operation of the osmotic energy scavenging device, increasing by nearly two orders of magnitude, and stabilizing after ≈6 h (Figure 22n). The resulting ion-selective membrane exhibited remarkable salt resistance and stability, overcoming surface charge shielding issues faced by traditional membranes. With abundant surface charge and ultra-small pore size, the osmotic energy scavenging device based on this membrane achieved a remarkable P_A density of 2.6 mW cm^{-2} (Figure 22o). Therefore, in energy scavenging devices reliant on regulating the Debye length range, the directional migration of ions, propelled by concentration gradients resulting from functional group hydrolysis and liquid evaporation, often encompasses longer migration distances, thereby limiting power output for most devices to typically below 1 W m^{-2}. However, harnessing concentration gradients to propel ionic migration, with their stronger driving force and shorter migration distances (equivalent to the thickness of the ion-selective membrane), could substantially enhance power density, reaching ≈10 W/m^2. Moreover, when the distribution density of functional groups in the polymer is significantly different and includes high-valent free ions, a higher concentration gradient of high-valent ions can be constructed after hydrolysis, thereby effectively promoting charge transport and improving output performance. This environment is more conducive to the practical application of energy scavenging devices reliant on ion migration driven by functional group hydrolysis.

5.2. Migration of Ions in 2D Nanofluidic Channels

The operation mechanism for directional ionic migration within the Debye length range, driven by salinity gradients in solid, high-humidity environments, presents a promising solution to overcome limitations posed by liquid-based systems, as depicted in **Figure 23**. Here, 2D nanomaterial GO serves as the ion-selective membrane coating the left electrode. When exposed to high humidity, the oxygen-containing functional groups on GO's nanochannels undergo hydrolysis, generating numerous negative charges. Subsequent KOH treatment triggers deoxidation reactions, reducing GO to form reduced graphene oxide (rGO) deposited on the right electrode's surface. Introducing a high concentration of metal cations into the rGO creates an ionic concentration gradient across the rGO and GO layers. As humid air passes through the nanochannels, metal cations on the rGO migrate toward the GO side, inducing an ionic current in the external circuit (Figure 23a). The nanochannels within GO exhibit a two-layer spacing of 7.7 Å, with a single-layer thickness of 3.4 Å, resulting in an effective channel size of ≈4.3 Å.[145] The nanochannel size, smaller than the typical dimension of the ion-hydrated shell (Figure 23b), prevents metal ions from fully hydrating as they pass through. Consequently, incompletely hydrated ions within the nano-confined region demonstrate higher ionic mobility and permeability compared to

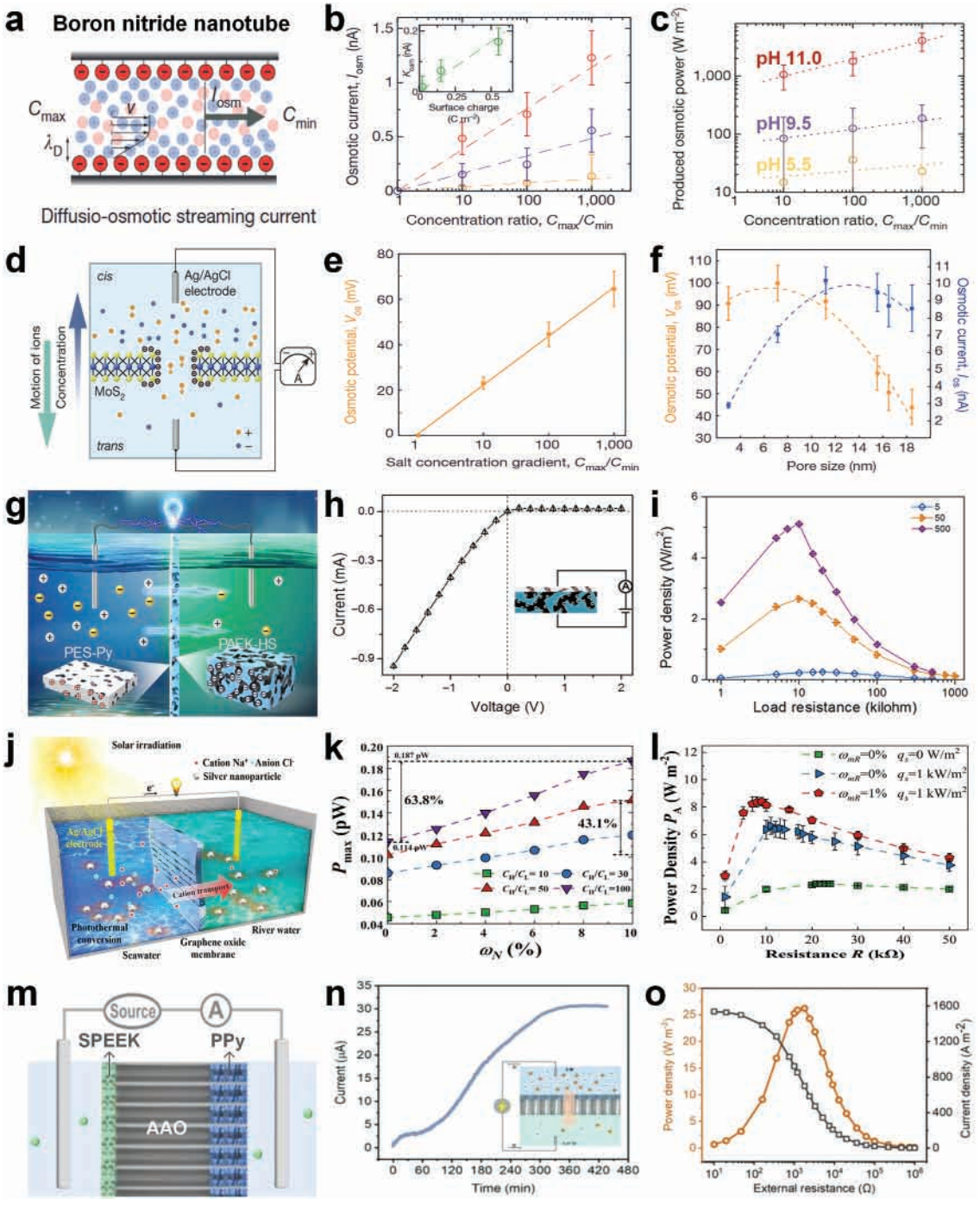

Figure 22. Energy scavenging devices were developed based on the migrating of ions driven by salinity gradient. a) A single nanochannel constructed by the boron nitride nanotube was proposed by Siria et al. in 2013.[110] b) Increasing the ionic concentration ratio between solutions effectively improved the I_{SC} of the device. c) The device achieved a P_A density of 0.4 W cm^{-2}. a–c) Reproduced with permission.[110] Copyright 2013, Springer Nature. d) A single-layer MoS_2 nanopore for osmotic energy scavenging was explored by Feng et al. in 2016.[191] e) Increasing the ionic concentration ratio improved device performance. f) The P_A density could reach 100 W cm^{-2}. d–f) Reproduced with permission.[191] Copyright 2016, Springer Nature. g) The Janus 3D porous membrane-based device was introduced by Zhu et al. in 2018.[142] h) The diode-like Janus membrane could obstruct reverse current flow. i) The generator achieved P_A densities of 0.51 mW cm^{-2}. g–i) Reproduced with permission.[142] Copyright 2018, The Authors, some rights reserved; exclusive license American Association for the Advancement of Science. Distributed under a Creative Commons Attribution NonCommercial License 4.0. j) A more efficient osmotic energy scavenging device by leveraging the photothermal effect was constructed by Ren et al. in 2022.[192] k) Adding nanoparticles to the nanochannels could increase the output power of the device. l) The P_A density could achieve 0.84 mW cm^{-2}. j–l) Reproduced with permission.[192] Copyright 2021, Elsevier Ltd. m) A salt-adaptive sandwich-structured membrane was constructed by Hao et al. in 2022.[193] n) The I_{SC} continued to rise with time during the initial operation of the device. o) The P_A density of the device could reach 2.6 mW cm^{-2}. m–o) Reproduced with permission.[193] Copyright 2022, Wiley-VCH.

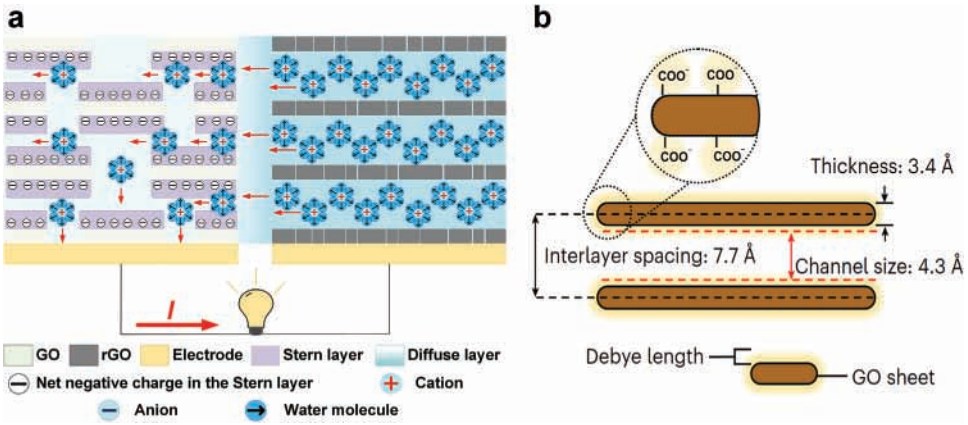

Figure 23. The operation mechanism for directional ionic migration within the Debye length range, driven by salinity gradients in solid, high-humidity environments, presents a promising solution to overcome limitations posed by liquid-based systems. a) As humid air passes through the nanochannels, metal cations on the rGO migrate toward the GO side, inducing an ionic current in the external circuit. b) The nanochannels within GO exhibit a two-layer spacing of 7.7 Å, with a single-layer thickness of 3.4 Å, resulting in an effective channel size of ≈4.3 Å. Reproduced with permission.[145] Copyright 2024, Springer Nature.

fully hydrated ions. This phenomenon, coupled with nanochannel properties, enhances ion migration efficiency, ultimately boosting the output performance of the energy scavenging devices.[144–147,194,195]

In 2021, inspired by the electric eel's ion-selective membrane mechanism, a solid-state osmotic power source was developed using full printing technology,[144] as shown in **Figure 24a**. This device utilized the unique 2D nanofluid channel structure of GO material, enhancing water permeability and cation conductivity. Unlike traditional osmotic energy scavenging devices, the introduction of a redox reaction using Ag electrodes improved galvanostatic discharge performance at 70% RH, leading to stronger energy output (Figure 24b). Additionally, employing a space-filling curve as a printing pattern increased the power generation unit's length, boosting the I_{SC} to 170 µA and achieving an outstanding volumetric P_A density of up to 2.5 mW cm^{-3} (Figure 24c). To enable long-term stable application in wearable or implantable devices, an ultra-thin (≈10 µm) osmotic power source was developed in 2022, combined with a mechanical energy scavenging TENG to form an energy scavenging system,[194] as depicted in Figure 24d. Utilizing Au electrodes ensured immunity to potential redox reactions. The directional ion migration generated a constant V_{OC} of 1.5 V, with a volumetric energy density of 6 mWh cm^{-3} and a volumetric P_A density of 28 mW cm^{-3}, comparable to supercapacitors (Figure 24e). This flat-panel osmotic power source, easily integrated into circuits and devices, formed a self-charging ion electronic device with a total thickness not exceeding 200 µm (Figure 24f), exhibiting excellent conformality and prolonged service life. Furthermore, a self-healing ionic gel osmotic generator based on GO aerogel and room-temperature ionic liquid was reported, operating effectively in harsh environments with a high power density of 1.3 mW cm^{-2}. The combination of graphene oxide aerogel with ionic liquid led to maximal performance improvement.

In 2023, we introduced an integrative paper-based osmotic power source, addressing the demand for biocompatible and recyclable energy solutions,[195] as displayed in Figure 24g. Leveraging salinity gradient differences and redox reactions, this device efficiently transported Li^+ ions within nanochannels, achieving remarkable volumetric P_A and energy densities of 438.02 mW cm^{-3} and 30.02 mWh cm^{-3}, respectively (Figure 24h). Its areal P_A density (1095.05 mW cm^{-2}) surpassed most flexible batteries, demonstrating its potential for various applications. This integrated product also incorporated a temperature sensor within the near-field communication (NFC) circuit of a wireless sensor system, allowing for integration on the same paper through double-sided printing (Figure 24i). Moreover, the paper-based design offered environmental advantages, as it could be recycled through incineration without producing harmful substances. In 2024, we further developed an ultra-high-performance osmotic power source by driving ion vertical transport at the edge of the PET substrate and Kapton film,[145] as illustrated in Figure 24j. This innovative approach aimed to reduce internal resistance and enhance power output by shortening the distance for ion transport. The device achieved an I_{SC} of ≈1 mA and a maximum P_A density of 1.59 W cm^{-2} (Figure 24k). With a high volumetric energy density of 9.46 Wh cm^{-3} and P_A density of 106.33 W cm^{-3} (Figure 24l), this technology showed promise for powering commercial electronics, highlighting its potential for practical applications. Focusing on energy scavenging devices regulating the Debye length range, precise alignment of nanochannel radius with the Debye length of ions emerges as a critical factor for achieving efficient output. Focusing on energy scavenging devices that regulate the Debye length range, precise alignment of nanochannel radius with the Debye length of ions emerges as a critical factor for achieving efficient output. Therefore, exploring nanotechnology's potential to meticulously control nanochannel size and shape, along with selecting appropriate materials for channel construction, assumes paramount importance. Concurrently, thorough investigation into the transport behavior of diverse ions in varied nanochannels is warranted to comprehend their interactions, transport rates, and selectivity. Through these concerted efforts, the design of more efficient devices capable of achieving heightened energy transfer and information flow can be realized.

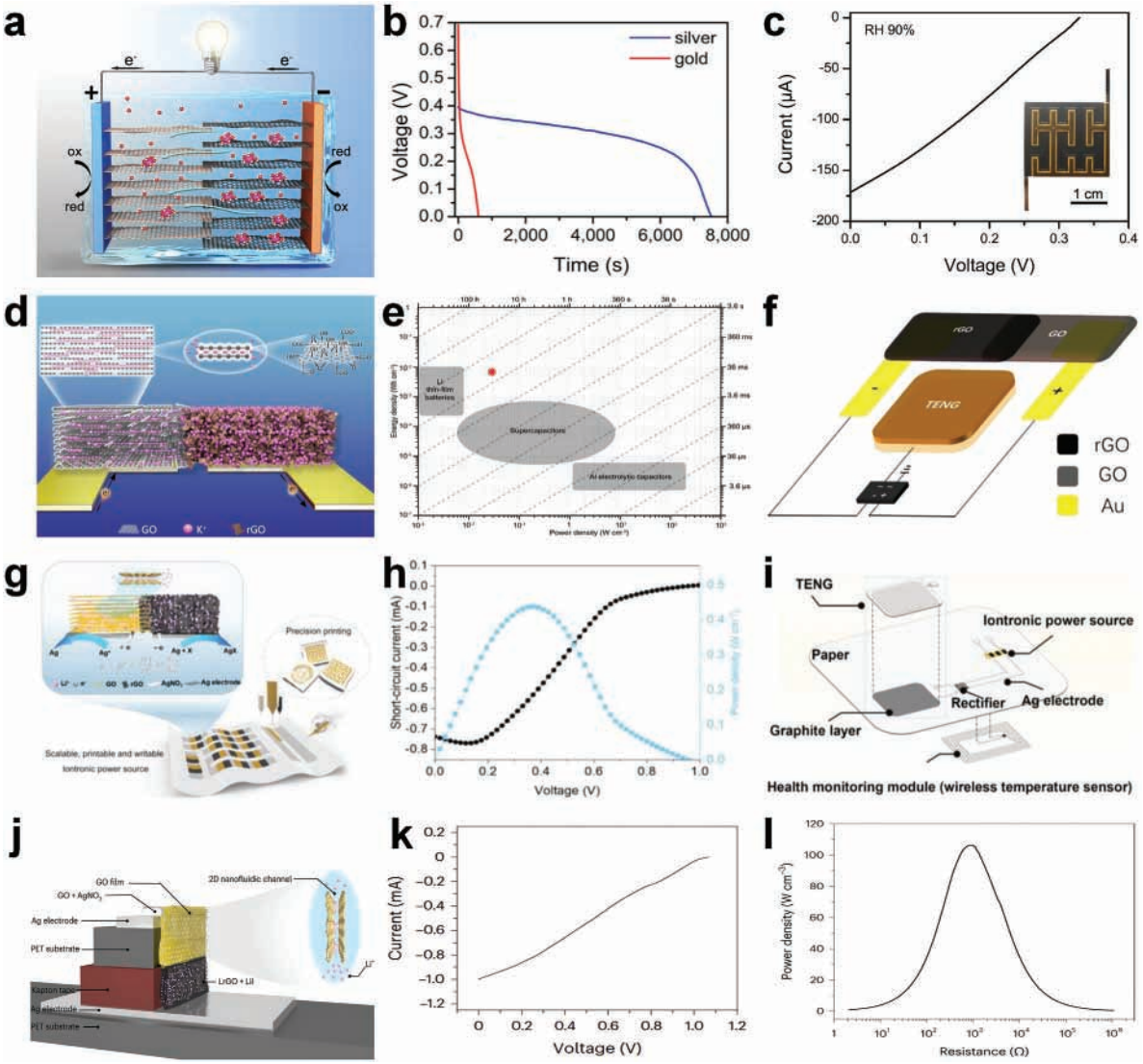

Figure 24. A series of energy scavenging devices were invented based on the migration of ions in 2D nanofluidic channels. a) A solid-state osmotic power source was developed using full printing technology in 2021.[144] b) By introducing the redox reaction, the device exhibited stronger energy output. c) The osmotic power source could achieve an I_{SC} of 170 μA and an outstanding volumetric P_A density of 2.5 mW cm^{-3}. a–c) Reproduced with permission.[144] Copyright 2021, the author(s) retains copyright to individual articles, and the NAS retains an exclusive license to publish these articles and holds copyright to the collectivework. d) To enable long-term stable application in wearable or implantable devices, an ultra-thin (10 μm) osmotic power source was developed in 2022.[194] e) Its volumetric energy density and P_A density could reach 6 mWh cm^{-3} and 28 mW cm^{-3}, respectively. f) This flat-panel osmotic power source, easily integrated into circuits and devices, formed a self-charging ion electronic device with a total thickness not exceeding 200 μm. d–f) Reproduced with permission.[194] Copyright 2022, The Author, Distributed under the terms of the Creative Commons CC BY license. g) An integrative paper-based osmotic power source was demonstrated in 2023.[195] h) The volumetric P_A and energy densities achieved 438.02 mW cm^{-3} and 30.02 mWh cm^{-3}. i) This integrated product also incorporated a temperature sensor within the NFC circuit of a wireless sensor system, allowing for integration on the same paper through double-sided printing. g–i) Reproduced with permission.[195] Copyright 2023, Wiley-VCH. j) An ultra-high-performance osmotic power source was inventedin 2024.[145] k) The device achieved an I_{SC} of ≈1 mA and a maximum P_A density of 1.59 W cm^{-2}. l) With a high volumetric energy density of 9.46 Wh cm^{-3} and P_A density of 106.33 W cm^{-3}, this technology showed promise for powering commercial electronics. j–l) Reproduced with permission.[145] Copyright 2024, Springer Nature.

6. Various Application Fields of Energy Scavenging Devices

6.1. Energy Scavenging Fields

Energy scavenging devices capable of dynamically regulating the EDL for efficient operation hold immense potential for diverse applications as depicted in **Figure 25**. Given the continuous advancements in technology and growing global interest in renewable energy sources, harnessing water wave energy, particularly in ocean environments, emerges as a promising pathway for generating clean and sustainable electricity. In 2014, Zhu et al. introduced a liquid-solid TENG driven by water waves[149] (Figure 25a). This innovative design utilized the movement of

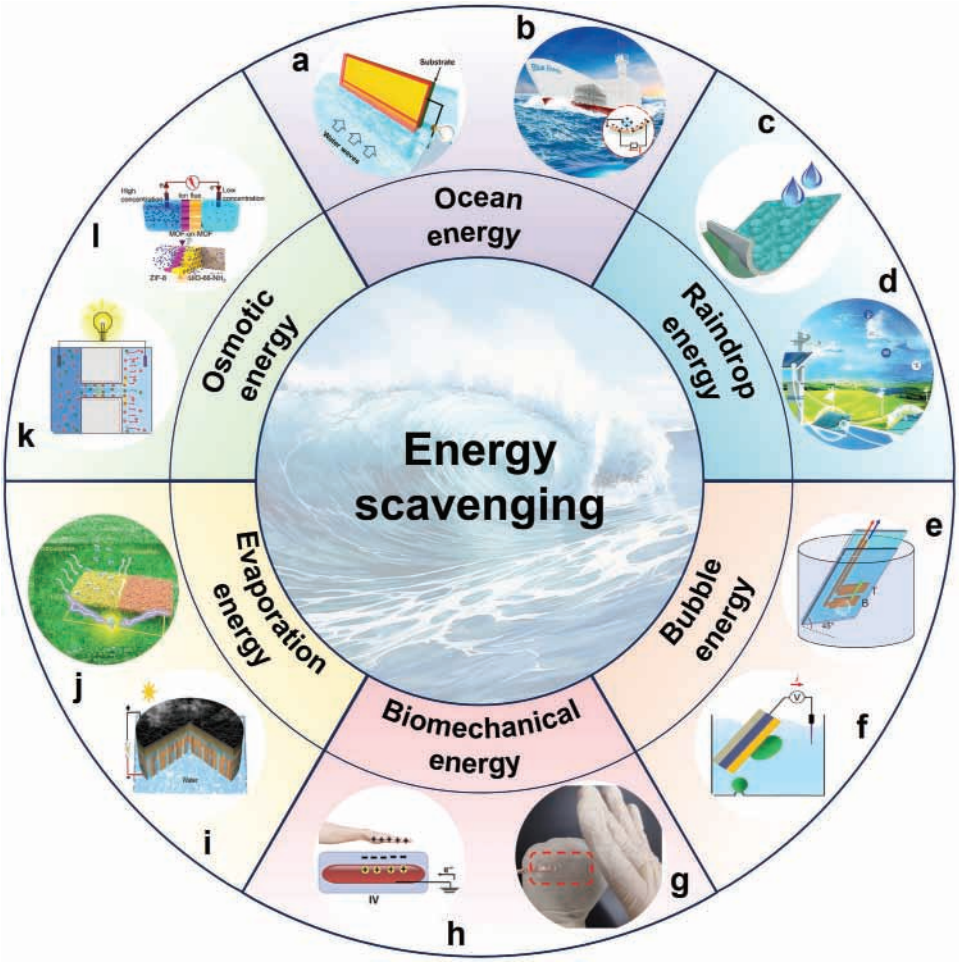

Figure 25. Energy scavenging devices that dynamically regulate the EDL have immense potential for wide applications in energy scavenging fields. a) A liquid-solid TENG driven by water waves was introduced by Zhu et al. in 2014. Reproduced with permission.[149] Copyright 2014, American Chemical Society. b) The droplet-based liquid-solid TENG was designed by Wei et al. in 2021. Reproduced with permission.[150] Copyright 2021, American Chemical Society. c) The solid-liquid TENG for scavenging raindrop energy was developed by Zhang et al. in 2018. Reproduced with permission.[196] Copyright 2018, Wiley-VCH. d) A complementary energy solution was created by Ye et al. in 2022. Reproduced with permission.[197] Copyright 2023, Wiley-VCH. e) A bubble-driven solid-liquid TENG was proposed by Wijewardhana et al. in 2017. Reproduced with permission.[198] Copyright 2017, Elsevier Ltd. f) A more efficient droplet-driven solid-liquid TENG was designed by Yan et al. in 2022. Reproduced with permission.[199] Copyright 2022, American Association for the Advancement of Science. Distributed under a Creative Commons Attribution NonCommercial License 4.0. g) A wearable TENG based on flexible and transparent cellulose hydrogel was invented by Hu et al. in 2021. Reproduced with permission.[200] Copyright 2021, Elsevier Ltd. h) A bio-mechanically driven hydrogel-based TENG was developed by Bagchi et al. in 2023. Reproduced with permission.[201] Copyright 2022, The Author(s), Distributed under the terms of the Creative Commons CC-BY license. i) A wood-based evaporation-driven generator was developed by Han et al. in 2023. Reproduced with permission.[202] Copyright 2024, Royal Society of Chemistry. j) A novel multifunctional generator was proposed by Sun et al. in 2023. Reproduced with permission.[203] Copyright 2023, Wiley-VCH. k) A high-power osmotic energy scavenging device was introduced by Ma et al. in 2021. Reproduced with permission.[204] Copyright 2021, Elsevier B.V. l) A hybridized bilayer metal-organic framework membrane was introduced by Tonnah et al. in 2023. Reproduced with permission.[205] Copyright 2023, American Chemical Society.

the boundary between the diffuse layer and the dense Stern layer, along with electrostatic induction, to induce an alternating flow of electrons between the electrodes. As a result, energy from water waves was efficiently converted and collected. With an area of 18 cm^2, the TENG system demonstrated an optimal average output power of 0.12 mW at a relative velocity of 0.5 m s^{-1}. Remarkably, it was capable of powering numerous light-emitting diodes (LEDs), highlighting its practical potential for lighting applications. In 2021, Wei et al. introduced a droplet-based liquid-solid TENG[150] (Figure 25b), operating on the same principle as Zhu et al.'s design. This TENG exhibited robust performance, even under extreme conditions. With just 1.5 mL droplets, it generated a charge of 30.7 nC and a voltage of 77.0 V, achieving a charge density of 15.35 nC cm^{-2}. When mounted on a boat, it charged a 0.47 µF capacitor to ≈4 V in just 4.1 s using ocean energy. These TENGs hold promise for deployment in marine environments, such as oceans, rivers, and coastal areas, for wave energy harvesting. Their versatility makes them suitable for various applications in marine environments, including monitoring, surveillance, and navigation. Raindrops, with their high speed and energy during descent, represent another significant source of water movement. In 2018, Zhang et al. introduced a

solid-liquid TENG[196] (Figure 25c) designed to harvest raindrop energy. Raindrops falling onto the dielectric surface of the device acquired a positive charge through CE with air, creating a charge imbalance and inducing a current flow between electrodes. With appropriate energy management circuitry, this TENG sustained LED illumination for over 300 s when continuously driven by simulated raindrops for 100 seconds. In 2022, Ye et al. combined liquid droplet-driven TENGs with photovoltaic-driven solar cells to create a complementary energy solution[197] (Figure 25d). This integration allowed for round-the-clock energy scavenging and sustainable energy supply. TENG arrays, based on the moving diffuse layer boundary, effectively harvested energy from raindrops falling in all directions, achieving a P_A density of 4.08 μW cm^{-2} under rainy conditions, surpassing traditional solar panels' P_A density of 3.7 μW cm^{-2}. This integration enhanced the overall output performance of the energy scavenging system, offering insights for efficient integration of TENG arrays with solar panels and addressing challenges associated with sustainable energy development. Moreover, the movement of bubbles in liquid could also induce boundary movement on the dense Stern layer of a dielectric surface. In 2017, Wijewardhana et al. proposed a bubble-driven solid-liquid TENG[198] (Figure 25e), harnessing rising air bubbles to facilitate energy scavenging. By capitalizing on the buoyancy-driven ascent of gas bubbles, this generator continuously promoted contact separation between the liquid and the dielectric surface, inducing electric current generation. It demonstrated high energy capture efficiency and stability, proving suitable for powering small electronic devices like 7-segment displays in flowing water pipes. To enhance output performance, Yan et al. designed a more efficient droplet-driven solid-liquid TENG in 2022[199] (Figure 25f). With a single bubble present, its V_{OC} reached up to 70 V. The generated power could be stored in capacitors, providing sustainable, clean, and real-time power for health monitoring devices. These generators offer a novel approach to energy scavenging, leveraging small bubbles in liquid media for durable and reliable long-term operation. In addition to water energy, exploring effective methods for harvesting biomechanical energy is also a promising field of research. In 2021, Hu et al. introduced a wearable TENG based on flexible and transparent cellulose hydrogel material, operating effectively in low-temperature environments[200] (Figure 25g). Positive charges on gloves regulated the EDL at the hydrogel-dielectric interface, generating over 180 V V_{OC}, sufficient to power numerous LEDs, demonstrating its potential for human movement in adverse conditions. In 2023, Bagchi et al. developed a biomechanically driven hydrogel-based TENG[201] (Figure 25h). Using semi-transparent hydrogel doped with gold nanoparticles as electrodes, it achieved a P_R density exceeding 0.17 mW cm^{-2} and an energy scavenging efficiency of ≈26%, offering new possibilities for self-powered wearable or implantable devices.

Evaporation energy holds significant promise, yet challenges like scalability and efficiency optimization persist. In 2023, Han et al. developed a wood-based evaporation-driven generator[202] by creating oxygen-containing functional groups on self-assembled multilayer nanofiber membranes (Figure 25i). This generator harnessed mobile ions produced during water evaporation to achieve a P_A density of 1.12 μW cm^{-2} and could charge a mobile phone battery, showcasing practical utility. Similarly, Sun et al. proposed a multifunctional generator in 2023[203] (Figure 25j), utilizing an asymmetric structure of polyaniline/carbon nanotube/polyvinyl alcohol (APCP) for power generation and seawater desalination. Connected units could power an electronic calculator continuously and collect 8.5 mL of fresh water within 11 h. These low-cost, long-life products offer promising prospects in flexible electronics, micro-energy systems, and related industries. The untapped potential of osmotic energy between seawater and freshwater presents further opportunities for development. In 2021, Ma et al. developed a high-power osmotic energy scavenging device using a single nanochannel[204] (Figure 25k). They emphasized extending the net charge on the nanochannel's inner surface toward the low-concentration side, achieving a P_A density increase from 0.42 to 0.49 W cm^{-2} and an energy scavenging efficiency surge from 4% to 26%. In 2023, Tonnah et al. introduced a hybridized bilayer metal-organic frameworks (MOF on MOF) membrane for enhanced ionic mobility in osmotic power generation[205] (Figure 25l). By utilizing the ethylene cavity in ZIF-8 and embedding PSS in UiO-66-NH2, they achieved a power density of 0.92 mW cm^{-2} under real seawater and river water mixing conditions, offering promising applications in seawater desalination and wastewater treatment.

6.2. Self-Powered Information Flow

Energy scavenging devices with dynamically regulating EDLs could offer significant potential for self-powered information flow fields including human-computer interaction and interface probes, as illustrated in **Figure 26**. For instance, Guo et al. introduced a groundbreaking flexible panel in human-computer interaction based on transparent TENG in 2022[152] (Figure 26a). This touchpad utilized dynamic EDL regulation at the hydrogel-dielectric interface, driven by users' finger charges, enabling rapid response and high-resolution human-machine interaction. With exceptional stretchability exceeding 11 500% strain capacity, it could adapt to diverse surfaces effortlessly. Its high transmittance of up to 98.1% ensured clear visibility on complex surfaces. Its biocompatibility allowed attachment to the hand for gesture-based computer operations, enhancing human-machine interaction. With multi-functional sensing capabilities, this transparent TENG holds promise for enhancing the intelligence and portability of smart electronic products. In 2023, Rahman et al. made a significant breakthrough by incorporating zeolitic imidazolate framework-8 (ZIF-8) into poly (acrylamide)-co-hydroxyethyl acrylate (PAAm-co-HEA) hydrogel,[153] creating a wearable TENG with high-precision strain sensing capabilities as the control panel (Figure 26b). This innovative device could work effectively even at sub-zero temperatures. This ability to operate under extreme conditions makes it have outstanding advantage in the field of wearable human-computer interaction interfaces. Through information flow, users could control computer games through intuitive gestures, enhancing the gaming experience. This advancement represents a significant step forward in wearable technology, offering new possibilities for human-computer interaction and energy scavenging applications. Moreover, energy scavenging devices regulating the EDL offer solutions for wireless communication systems for efficient information flow in human-computer interaction. In 2022, Wang et al. developed a water-based TENG for remote information flow by

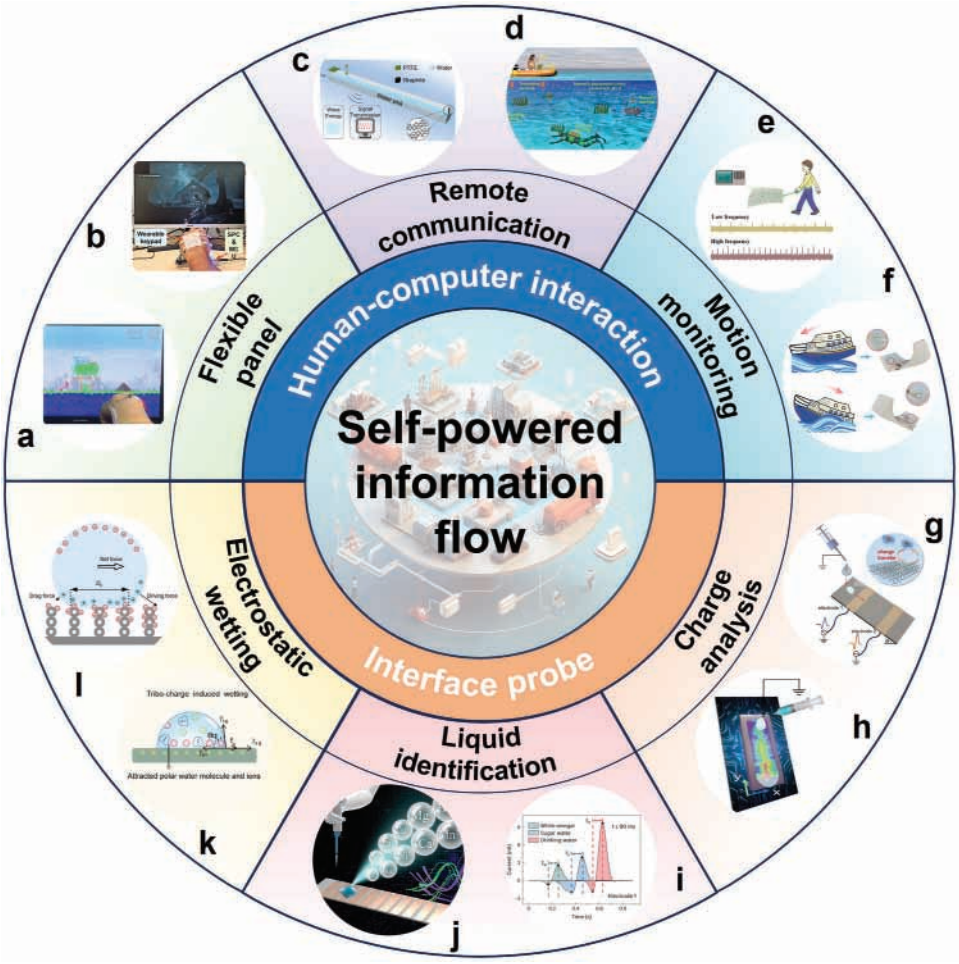

Figure 26. Energy scavenging devices with dynamically regulating EDLs could offer significant potential for self-powered information flow fields. a) A groundbreaking touchpad based on transparent TENG was introduced by Guo et al. in 2022. Reproduced with permission.[152] Copyright 2022, Wiley-VCH. b) A wearable TENG with high-precision strain sensing capabilities was introduced by Rahman et al.in 2023. Reproduced with permission.[153] Copyright 2023, Wiley-VCH. c) A water-based TENG for remote information transmission was introduced by Wang et al. in 2022. Reproduced with permission.[206] Copyright 2022, Elsevier B.V. d) A TENG-based method for underwater communication was proposed by Zhao et al. in 2022. Reproduced with permission.[207] Copyright 2022, The Author(s), Distributed under the terms of the Creative Commons CC BY license. e) A novel stretchable TENG for accurate human motion detection was introduced by Jing et al. in 2021. Reproduced with permission.[208] Copyright 2021, Elsevier Ltd. f) A TTI by integrating solid-liquid contact electrification and work function difference was proposed in 2024. Reproduced with permission.[209] Copyright 2024, Elsevier Inc. Distributed under the terms of the Creative Commons CC-BY license. g) A liquid droplet TENG with spatially arranged electrodes was pioneered by Zhang et al. in 2021. Reproduced with permission.[210] Copyright 2021, American Chemical Society. h) A pixelated TENG array for investigating charge transfer phenomena was introduced by Zhang et al. in 2023. Reproduced with permission.[211] Copyright 2023, American Chemical Society. i) A droplet identification sensor system inspired by human taste perception processes was introduced by Wei et al. in 2023. Reproduced with permission.[212] Copyright 2023, Springer Nature. j) A real-time TES for chemical analysis was introduced by Zhang et al. in 2024. Reproduced with permission.[213] Copyright 2024, American Chemical Society. This publication is licensed under CC-BY 4.0. k) An innovative method to simultaneously monitor dynamic changes in contact angle and electrical signals by integrating a single-electrode TENG with a goniometer was proposed by Zhang et al. in 2024. Reproduced with permission.[214] Copyright 2024, Wiley-VCH. l) A novel approach to achieve high-speed and ultra-long transmission of droplets by printing surface charge density gradients on different substrates was proposed by Sun et al. in 2019. Reproduced with permission.[215] Copyright 2019, Springer Nature.

modulating the EDL at the water-PTFE interface[206] (Figure 26c). This enabled self-powered Morse code transmission using water as the medium. Similarly, Zhao et al. proposed a TENG-based method for generating Maxwell displacement currents for underwater communication in 2022[207] (Figure 26d). By regulating charges at underwater electrodes and EDL distributions, stable signals were achieved despite underwater disturbances, facilitating text and image transmission at 16 bits per second. These innovations promise significant advancements in remote communication technology. Further sensor design optimizations could enhance sensitivity and stability in human-machine interaction, expanding its application range in detecting various motion scenarios for motion information flow. In 2021, Jing et al. introduced a stretchable TENG based on organogel electrodes for efficient energy harvesting and accurate human motion detection[208] (Figure 26e). By dynamically regulating the

EDL between the gel electrode and dielectric silicon, the TENG generated electrical signals in response to human movement. Integration with an experimental garment enabled successful monitoring of arm swinging, with signal frequency linearly correlating with walking frequency. To broaden the application range of motion monitoring, we proposed a transistor-like triboiontronics (TTI) by integrating solid-liquid contact electrification and work function difference in 2024[209] (Figure 26f). Gated by the water droplet, two different metals were analogous to the source and drain terminals to form the TTI, capable of monitoring movement without external electric power. When the DI water droplet moved to source-drain terminals, a DC threshold sensing signal rapidly responded with a high signal-to-noise ratio. Moreover, TTI with multiple source-drain terminals provided multifunctionality by enabling the alarm for irregular movements through various threshold sensing signals. TTI self-powered threshold sensor offered an accurate and effective way to pre-alarm potentially dangerous situations, such as shipwrecks, driving collisions, and earthquakes.

In the related research field of solid-liquid interface probes, Zhang et al. pioneered a liquid droplet TENG with spatially arranged electrodes in 2021,[210] shedding light on the charge transfer process at liquid-solid interfaces (Figure 26g). Their analysis revealed that charge transfer occurred as an accumulation process during droplet descent, with electrons playing a crucial role. This deepened our understanding of electrostatic phenomena and provided insights for further research into charge exchange mechanisms. In 2023, Zhang et al. introduced a pixelated TENG array[211] for investigating charge transfer phenomena when water droplets move on hydrophobic surfaces (Figure 26h). This array revealed non-uniform charge distribution during droplet motion, suggesting a two-step model involving electron transfer and ion adsorption. These studies, serving as probes for investigating solid-liquid interfaces, can scavenge crucial information about charge transfer, liquid properties, interface behavior, and biological interfaces, offering powerful tools for the research of interface science and technology. In the study of liquid properties, Wei et al. introduced a droplet identification sensor system inspired by human taste perception processes in 2023,[212] achieving comprehensive liquid identification capabilities through dynamic morphological changes and liquid-solid CE principles (Figure 26i). This self-powered system integrated visual and electrical signals with deep learning algorithms, achieving an impressive identification accuracy of 96.0%. To enhance liquid identification capabilities, Zhang et al. introduced real-time triboelectric spectroscopy (TES) for chemical analysis in 2024,[213] enabling ultra-fast and accurate detection of various ions in water (Figure 26j). By leveraging charge transfer at the liquid-solid interface, this method provided spectral tuning of the charge transfer mode for in situ chemical detection, achieving remarkable qualitative and quantitative accuracy nearing 93%. In addition, the TENG could be used as an interface probe to explore the effect of solid-liquid CE on the wettability of dielectric materials, thereby scavenging specific charge transfer information during the wetting process. In 2024, Tang et al. proposed an innovative method to simultaneously monitor dynamic changes in contact angle and electrical signals by integrating a single-electrode TENG with a goniometer[214] (Figure 26k). This approach revealed the impact of surface charge accumulation on the wetting kinetics of materials. The observed linear relationship between contact angle and surface charge suggests that CE-induced wetting occurs in two stages: first, triboelectric charge accumulates from CE on the dielectric material, and then these charges induce wetting on the material's surface. This discovery could hold significant potential for new applications and technological advancements in charged surface environments, providing valuable insights into wetting control and surface engineering. By utilizing solid-liquid CE, it becomes feasible to pre-program charge density on the surface of dielectric materials, thereby controlling various wetting characteristics to convey path information and propel droplets accordingly. In 2019, Sun et al. proposed a novel approach to achieve high-speed and ultra-long transmission of droplets by printing surface charge density gradients on different substrates[215] (Figure 26l). This method facilitates directed, long-range, and self-propelled droplet transport without the need for additional energy input under ambient conditions. Hence, this research opens up a new technological avenue for manipulating droplet transport on flat, flexible, and vertical surfaces, with potential applications in water harvesting, bio-analysis, and other domains. These studies offered efficient solutions for self-powered information flow fields, with features such as high sensitivity, portability, and ease of integration.

7. Conclusion and Perspectives

Controlled charge transport is indispensable across various scientific and technological domains, serving as carriers for energy and information flow and as probes for material properties and dynamics. Iontronics uses ions as signal carriers, offering the potential to regulate charge flux, control ion current direction, and magnitude akin to the nervous system, and amplify signals. The EDL functions as a critical interface for ionic-electronic coupling in iontronics, facilitating dynamic regulations to control ion transport and rearrangement, thereby influencing electronic properties. This provides an alternative approach to enable efficient energy and information flow, meeting the requirements of intelligent IoT and AI systems. In this comprehensive review, energy scavenging devices were classified into three categories based on the "two-step" EDL model, which involved regulating the distribution and movement of charge carriers within the entire EDL, diffuse layer, and Debye length range. First, when dynamically modulating the entirety of the EDL, manipulation of the EDL boundary facilitates the directional migration of ions, thereby engendering a low-amplitude constant current. Furthermore, leveraging electrostatic force enables precise control over charge distribution within the Stern layer, thereby orchestrating ionic migration and eliciting high-voltage AC signals. Second, in the process of regulating the diffuse layer, techniques such as displacement of the diffuse layer boundary on the dielectric surface or supplementation via solid-liquid CE may be employed. These methodologies foster electron transfer between charge-collecting electrodes, yielding either AC high-voltage output or more efficacious instantaneous DC ionic-electronic coupling output, respectively. Third, through dynamic regulation of the Debye length range of the EDL, ionic concentration gradients propel specific polar ions through charged nanochannels, yielding a steady current signal. Alternatively, in humid environments, ionic concentration gradients drive rapid ion migration in 2D nanofluidic

channels, resulting in heightened efficiency of continuous current output. Moreover, to underscore the practical efficacy and application versatility of energy scavenging devices, illustrative scenarios were presented, affirming their relevance in scavenging energy and information flow by self-powered systems.

In the forthcoming era, the advancement of energy scavenging and self-powered information flow will prioritize maximizing efficiency through refined design, material innovation, and the integration of intelligent technologies. This trend will entail a transition toward miniaturization to facilitate integration into portable electronics, thereby enabling the development of self-powered wearables, IoT sensors, and compact devices. In the realm of computing, the conventional von Neumann architecture confronts challenges as Moore's law approaches its limits. To address the escalating demand for data processing capabilities, there is a pressing need for more efficient neuromorphic computing paradigms. Iontronics, which harnesses ionic/electronic charge transfer for signal exchange at interfaces, offers notable advantages in energy efficiency compared to traditional electronics. By leveraging the EDL to regulate electronic properties, iontronics emerges as a promising avenue for effectively managing energy and information flow in the post-Moore era.

Acknowledgements

This work was supported by the Beijing Natural Science Foundation (Grant No. IS23040).

Conflict of Interest

The authors declare no conflict of interest.

Keywords

diffuse layer, dynamic regulation, electrical double layer, scavenging energy and information, Stern layer

Received: March 31, 2024
Revised: April 19, 2024
Published online: May 7, 2024

[1] J. F. Mercure, H. Pollitt, J. E. Viñuales, N. R. Edwards, P. B. Holden, U. Chewpreecha, P. Salas, I. Sognnaes, A. Lam, F. Knobloch, *Nat. Clim. Change* **2018**, *8*, 588.
[2] C. Kennedy, *J. Ind. Ecol.* **2020**, *24*, 887.
[3] M. Balat, *Energy Source Part B* **2007**, *2*, 31.
[4] X. Gong, R. Shi, J. Xu, B. Lin, *Appl. Energy* **2021**, *285*, 116384.
[5] D. Welsby, J. Price, S. Pye, P. Ekins, *Nature* **2021**, *597*, 230.
[6] M. I. Hoffert, *Science* **2010**, *329*, 1292.
[7] S. Spiegel, B. Brown, *Nature* **2017**, *550*, 43.
[8] K. K. Bertine, E. D. Goldberg, *Science* **1971**, *173*, 233.
[9] N. Butt, H. L. Beyer, J. R. Bennett, D. Biggs, R. Maggini, M. Mills, A. R. Renwick, L. M. Seabrook, H. P. Possingham, *Science* **2013**, *342*, 425.
[10] J. M. Perkel, *Nature* **2017**, *542*, 125.
[11] J. Franco, A. Aris, B. Canberk, A. S. Uluagac, *IEEE Commun. Surv. Tutorials* **2021**, *23*, 2351.
[12] L. Portilla, K. Loganathan, H. Faber, A. Eid, J. G. D. Hester, M. M. Tentzeris, M. Fattori, E. Cantatore, C. Jiang, A. Nathan, G. Fiori, T. Ibn-Mohammed, T. D. Anthopoulos, V. Pecunia, *Nat. Electron.* **2022**, *6*, 10.
[13] M. S. Ali, M. Vecchio, M. Pincheira, K. Dolui, F. Antonelli, M. H. Rehmani, *IEEE Commun. Surv. Tutorials* **2019**, *21*, 1676.
[14] X. Jie, S. Gonzalez-Cortes, T. Xiao, B. Yao, J. Wang, D. R. Slocombe, Y. Fang, N. Miller, H. A. Al-Megren, J. R. Dilworth, J. M. Thomas, P. P. Edwards, *Energy Environ. Sci.* **2019**, *12*, 238.
[15] P. Erickson, M. Lazarus, G. Piggot, *Nat. Clim. Change* **2018**, *8*, 1037.
[16] R. York, *Nat. Clim. Change* **2012**, *2*, 441.
[17] X. Tan, J. Nielsen, *Chem. Soc. Rev.* **2022**, *51*, 4763.
[18] R. Haight, W. Haensch, D. Friedman, *Science* **2016**, *353*, 124.
[19] G. L. Stephens, J. Li, M. Wild, C. A. Clayson, N. Loeb, S. Kato, T. L'Ecuyer, P. W. Stackhouse, M. Lebsock, T. Andrews, *Nat. Geosci.* **2012**, *5*, 691.
[20] J. Fasullo, A. Dai, T. Qian, L. Smith, K. E. Trenberth, *J. Hydrometeorol.* **2007**, *8*, 758.
[21] B. R. Scanlon, S. Fakhreddine, A. Rateb, I. de Graaf, J. Famiglietti, T. Gleeson, R. Q. Grafton, E. Jobbagy, S. Kebede, S. R. Kolusu, L. F. Konikow, D. Long, M. Mekonnen, H. M. Schmied, A. Mukherjee, A. MacDonald, R. C. Reedy, M. Shamsudduha, C. T. Simmons, A. Sun, R. G. Taylor, K. G. Villholth, C. J. Vörösmarty, C. Zheng, *Nat. Rev. Earth Environ.* **2023**, *4*, 87.
[22] Y. Wang, S. Gao, W. Xu, Z. Wang, *Adv. Funct. Mater.* **2020**, *30*, 1908252.
[23] J. Falnes, *Mar. Struct.* **2007**, *20*, 185.
[24] A. von Jouanne, T. K. A. Brekken, *P. IEEE* **2017**, *105*, 2147.
[25] N. Khan, A. Kalair, N. Abas, A. Haider, *Renewable Sustainable Energy Rev.* **2017**, *72*, 590.
[26] J. Tollefson, *Nature* **2014**, *508*, 302.
[27] Z. L. Wang, *Nature* **2017**, *542*, 159.
[28] J. Görtz, M. Aouad, S. Wieprecht, K. Terheiden, *Renewable Sustainable Energy Rev.* **2022**, *165*, 112027.
[29] N. Kittner, *Nat. Sustain.* **2024**, *7*, 104.
[30] Z. de Souza, G. L. Tiago Filho, R. M. Barros, I. F. Silva dos Santos, F. d. G. B. da Silva, M. D. Prado Leite, É. P. Prudente, *Renewable Sustainable Energy Rev.* **2017**, *68*, 272.
[31] M. J. Khan, M. T. Iqbal, J. E. Quaicoe, *Renewable Sustainable Energy Rev.* **2008**, *12*, 2177.
[32] E. Pallant, *Science* **2006**, *314*, 251.
[33] Z. Pan, W. G. Pitt, Y. Zhang, N. Wu, Y. Tao, T. T. Truscott, *Nat. Plants* **2016**, *2*, 16076.
[34] S. R. Begum, A. Chandrasekhar, *iScience* **2024**, *27*, 108878.
[35] A.-H. Cavusoglu, X. Chen, P. Gentine, O. Sahin, *Nat. Commun.* **2017**, *8*, 617.
[36] P. Tao, G. Ni, C. Song, W. Shang, J. Wu, J. Zhu, G. Chen, T. Deng, *Nat. Energy* **2018**, *3*, 1031.
[37] S. Fang, J. Li, Y. Xu, C. Shen, W. Guo, *Joule* **2022**, *6*, 690.
[38] Q. Ma, Q. He, P. Yin, H. Cheng, X. Cui, Q. Yun, H. Zhang, *Adv. Mater.* **2020**, *32*, 2003720.
[39] Z. Zhang, X. Li, J. Yin, Y. Xu, W. Fei, M. Xue, Q. Wang, J. Zhou, W. Guo, *Nat. Nanotechnol.* **2018**, *13*, 1109.
[40] O. Ellabban, H. Abu-Rub, F. Blaabjerg, *Renewable Sustainable Energy Rev.* **2014**, *39*, 748.
[41] Z. L. Wang, T. Jiang, L. Xu, *Nano Energy* **2017**, *39*, 9.
[42] T. Jiang, H. Pang, J. An, P. Lu, Y. Feng, X. Liang, W. Zhong, Z. L. Wang, *Adv. Energy Mater.* **2020**, *10*, 2000064.
[43] A. Ahmed, Z. Saadatnia, I. Hassan, Y. Zi, Y. Xi, X. He, J. Zu, Z. L. Wang, *Adv. Energy Mater.* **2016**, *7*, 1601705.
[44] S. L. Zhang, M. Xu, C. Zhang, Y.-C. Wang, H. Zou, X. He, Z. Wang, Z. L. Wang, *Nano Energy* **2018**, *48*, 421.
[45] B. Cao, P. Wang, P. Rui, X. Wei, Z. Wang, Y. Yang, X. Tu, C. Chen, Z. Wang, Z. Yang, T. Jiang, J. Cheng, Z. L. Wang, *Adv. Energy Mater.* **2022**, *12*, 202627.

[46] H. Zhai, S. Ding, X. Chen, Y. Wu, Z. Lin Wang, *Mater. Today* **2023**, *65*, 166.
[47] F. A. Shillington, *Nature* **1981**, *290*, 123.
[48] W. Jiang, C. Chen, C. Wang, J. Li, M. Zhao, T. Xiang, P. Wang, *Energy Environ. Sci.* **2023**, *16*, 6003.
[49] Q. Gao, Y. Xu, X. Yu, Z. Jing, T. Cheng, Z. L. Wang, *ACS Nano* **2022**, *16*, 6781.
[50] S. Yang, C. Zhang, Z. Du, Y. Tu, X. Dai, Y. Huang, J. Fan, Z. Hong, T. Jiang, Z. L. Wang, *Adv. Energy Mater.* **2024**, *14*, 2304184.
[51] Y. Yang, J. Wen, F. Chen, Y. Hao, X. Gao, T. Jiang, B. Chen, Z. L. Wang, *Adv. Funct. Mater.* **2022**, *32*, 2200521.
[52] X. Liang, Z. Liu, Y. Feng, J. Han, L. Li, J. An, P. Chen, T. Jiang, Z. L. Wang, *Nano Energy* **2021**, *83*, 105836.
[53] S. Zhang, Z. Jing, X. Wang, K. Fan, H. Zhao, Z. L. Wang, T. Cheng, *ACS Energy Lett.* **2022**, *7*, 4282.
[54] S. Gao, Y. Chen, S. Feng, X. Chen, J. Zhang, R. Wang, H. Wei, X. Luo, X. Zeng, *Nano Energy* **2023**, *113*, 108530.
[55] D. Jiang, F. Guo, M. Xu, J. Cai, S. Cong, M. Jia, G. Chen, Y. Song, *Nano Energy* **2019**, *58*, 842.
[56] S. Xu, X. Fu, G. Liu, T. Tong, T. Bu, Z. L. Wang, C. Zhang, *iScience* **2021**, *24*, 102318.
[57] Y. Zi, H. Guo, Z. Wen, M.-H. Yeh, C. Hu, Z. L. Wang, *ACS Nano* **2016**, *10*, 4797.
[58] C. Zhang, W. Tang, C. Han, F. Fan, Z. L. Wang, *Adv. Mater.* **2014**, *26*, 3580.
[59] C. Ye, K. Dong, J. An, J. Yi, X. Peng, C. Ning, Z. L. Wang, *ACS Energy Lett.* **2021**, *6*, 1443.
[60] R. Henderson, *Renewable Energy* **2006**, *31*, 271.
[61] T. Oki, S. Kanae, *Science* **2006**, *313*, 1068.
[62] P. Wu, N. Christidis, P. Stott, *Nat. Clim. Change* **2013**, *3*, 807.
[63] M. L. Roderick, F. Sun, G. D. Farquhar, *Science* **2012**, *336*, 1230.
[64] S. Jasechko, Z. D. Sharp, J. J. Gibson, S. J. Birks, Y. Yi, P. J. Fawcett, *Nature* **2013**, *496*, 347.
[65] Z. Tang, S. Lin, Z. L. Wang, *J. Phys. Chem. C* **2022**, *126*, 8897.
[66] X. Crispin, S. V. Kalinin, *Nat. Mater.* **2017**, *16*, 704.
[67] V. R. Stamenkovic, D. Strmcnik, P. P. Lopes, N. M. Markovic, *Nat. Mater.* **2016**, *16*, 57.
[68] W. J. Heideger, A. Vasudev, *Nature* **1966**, *209*, 295.
[69] S. F. L. Mertens, A. Hemmi, S. Muff, O. Groning, S. De Feyter, J. Osterwalder, T. Greber, *Nature* **2016**, *534*, 676.
[70] A. Hamnett, *Nature* **1981**, *290*, 276.
[71] M. Becker, P. Loche, M. Rezaei, A. Wolde-Kidan, Y. Uematsu, R. R. Netz, D. J. Bonthuis, *Chem. Rev.* **2024**, *124*, 1.
[72] W. Schmickler, *Chem. Rev.* **1996**, *96*, 3177.
[73] Y. Z. Wang, X. Y. Shan, L. P. Ma, J. W. Wang, D. W. Wang, Z. Q. Peng, H. M. Cheng, F. Li, *Adv. Energy Mater.* **2019**, *9*, 1803715.
[74] S.-J. Shin, D. H. Kim, G. Bae, S. Ringe, H. Choi, H.-K. Lim, C. H. Choi, H. Kim, *Nat. Commun.* **2022**, *13*, 174.
[75] X. Shen, T. Sun, L. Yang, A. Krasnoslobodtsev, R. Sabirianov, M. Sealy, W.-N. Mei, Z. Wu, L. Tan, *Nat. Commun.* **2021**, *12*, 820.
[76] Y. Yang, H. Hua, Z. Lv, M. Zhang, C. Liu, Z. Wen, H. Xie, W. He, J. Zhao, C. C. Li, *Adv. Funct. Mater.* **2022**, *33*, 2212446.
[77] L. Dick, T. Stettner, Y. Liu, S. Liu, B. Kirchner, A. Balducci, *Energy Storage Mater.* **2022**, *53*, 744.
[78] M. Suda, R. Kato, H. M. Yamamoto, *Science* **2015**, *347*, 743.
[79] M. Shi, Z. Zhang, M. Zhao, X. Lu, Z. L. Wang, *J. Electrochem. Soc.* **2021**, *168*, 120548.
[80] Y. Lv, M. Zhao, Y. Du, Y. Kang, Y. Xiao, S. Chen, *Energy Environ. Sci.* **2022**, *15*, 4748.
[81] Q. Wu, M. T. McDowell, Y. Qi, *J. Am. Chem. Soc.* **2023**, *145*, 2473.
[82] Z. Wang, J. Diao, G. Henkelman, C. B. Mullins, *Adv. Funct. Mater.* **2024**, 2314002.
[83] K. Qi, P. Liang, S. Wei, H. Ao, X. Ding, S. Chen, Z. Fan, C. Wang, L. Song, X. Wu, C. Wu, Y. Zhu, *Energy Environ. Sci.* **2024**, *17*, 2566.
[84] H. Gao, J. Li, J. R. Miller, R. A. Outlaw, S. Butler, K. Lian, *Energy Storage Mater.* **2016**, *4*, 66.
[85] X. Chen, L. Qiu, J. Ren, G. Guan, H. Lin, Z. Zhang, P. Chen, Y. Wang, H. Peng, *Adv. Mater.* **2013**, *25*, 6436.
[86] K. Ge, H. Shao, P.-L. Taberna, P. Simon, *ACS Energy Lett.* **2023**, *8*, 2738.
[87] J. Zhao, A. F. Burke, *Adv. Energy Mater.* **2020**, *11*, 2002192.
[88] L. Jia, Z. H. Guo, L. Li, C. Pan, P. Zhang, F. Xu, X. Pu, Z. L. Wang, *ACS Nano* **2021**, *15*, 19651.
[89] Y.-M. Yuan, B. Liu, M. R. Adibeig, Q. Xue, C. Qin, Q.-Y. Sun, Y. Jin, M. Wang, C. Yang, *Adv. Mater.* **2024**, *36*, 2310429.
[90] J. Shi, Y. Dai, Y. Cheng, S. Xie, G. Li, Y. Liu, J. Wang, R. Zhang, N. Bai, M. Cai, Y. Zhang, Y. Zhan, Z. Zhang, C. Yu, C. F. Guo, *Sci. Adv.* **2023**, *9*, adf8831.
[91] Y. Liu, J. Wang, J. Chen, Q. Yuan, Y. Zhu, *Adv. Compos. Hybrid Mater.* **2023**, *6*, 210.
[92] H. Qin, L. Xu, S. Lin, F. Zhan, K. Dong, K. Han, H. Wang, Y. Feng, Z. L. Wang, *Adv. Funct. Mater.* **2022**, *32*, 2111662.
[93] G. Xue, Y. Xu, T. Ding, J. Li, J. Yin, W. Fei, Y. Cao, J. Yu, L. Yuan, L. Gong, J. Chen, S. Deng, J. Zhou, W. Guo, *Nat. Nanotechnol.* **2017**, *12*, 317.
[94] X. Liang, S. Liu, S. Lin, H. Yang, T. Jiang, Z. L. Wang, *Adv. Energy Mater.* **2023**, *13*, 2300571.
[95] T. G. Morrissey, S. K. Mitchell, A. T. Jaros, E. Ambos, C. Keplinger, *Energy Technol.* **2019**, *7*, 1801007.
[96] L. Zhang, X. Li, Y. Zhang, Y. Feng, F. Zhou, D. Wang, *Nano Energy* **2020**, *78*, 105370.
[97] Y. Zhang, S. Guo, Z. G. Yu, H. Qu, W. Sun, J. Yang, L. Suresh, X. Zhang, J. J. Koh, S. C. Tan, *Adv. Mater.* **2022**, *34*, 2201228.
[98] L. Zheng, Z.-H. Lin, G. Cheng, W. Wu, X. Wen, S. Lee, Z. L. Wang, *Nano Energy* **2014**, *9*, 291.
[99] D. Choi, D. W. Kim, D. Yoo, K. J. Cha, M. La, D. S. Kim, *Nano Energy* **2017**, *36*, 250.
[100] Y. Liu, Y. Zheng, T. Li, D. Wang, F. Zhou, *Nano Energy* **2019**, *61*, 454.
[101] Z.-H. Lin, G. Cheng, L. Lin, S. Lee, Z. L. Wang, *Angew. Chem., Int. Ed.* **2013**, *52*, 12545.
[102] F. Shen, D. Zhang, Q. Zhang, Z. Li, H. Guo, Y. Gong, Y. Peng, *Nano Energy* **2022**, *99*, 107431.
[103] W. Xu, J. Yang, S. Liu, Y. Meng, D. Feng, L. Jia, S. Liu, B. Wang, X. Li, *Nano Energy* **2021**, *86*, 106093.
[104] J. Dong, S. Huang, J. Luo, J. Zhao, F. R. Fan, Z.-Q. Tian, *Nano Energy* **2022**, *95*, 106971.
[105] J. Yin, X. M. Li, J. Yu, Z. H. Zhang, J. X. Zhou, W. L. Guo, *Nat. Nanotechnol.* **2014**, *9*, 378.
[106] X. Liu, H. Gao, J. E. Ward, X. Liu, B. Yin, T. Fu, J. Chen, D. R. Lovley, J. Yao, *Nature* **2020**, *578*, 550.
[107] J. Tan, J. Duan, Y. Zhao, B. He, Q. Tang, *Nano Energy* **2018**, *48*, 128.
[108] Y. Huang, H. Cheng, C. Yang, P. Zhang, Q. Liao, H. Yao, G. Shi, L. Qu, *Nat. Commun.* **2018**, *9*, 4166.
[109] W. Zhao, Y. Wang, M. Han, J. Xu, L. Han, K. C. Tam, *Nano Energy* **2022**, *98*, 107291.
[110] A. Siria, P. Poncharal, A.-L. Biance, R. Fulcrand, X. Blase, S. T. Purcell, L. Bocquet, *Nature* **2013**, *494*, 455.
[111] X. Li, T. Xiao, B. Lu, J. He, J. Zhai, *Adv. Mater. Interfaces* **2021**, *9*, 2101960.
[112] Q. Ren, Q. Cui, K. Chen, J. Xie, P. Wang, *Desalination* **2022**, *535*, 115802.
[113] X. J. Li, L. Q. Zhang, Y. E. Feng, Y. L. Zhang, H. Z. Xu, F. Zhou, D. A. Wang, *ACS Nano* **2023**, *17*, 23977.
[114] Z. Q. Yuan, X. Y. Du, H. D. Niu, N. W. Li, G. Z. Shen, C. J. Li, Z. L. Wang, *Nanoscale* **2019**, *11*, 495.
[115] L. Wang, W. Liu, Z. Yan, F. Wang, X. Wang, *Adv. Funct. Mater.* **2020**, *31*, 2007221.

[116] X. Zhao, Z. Wang, Z. Liu, S. Yao, J. Zhang, Z. Zhang, T. Huang, L. Zheng, Z. L. Wang, L. Li, *Nano Energy* **2022**, *96*, 107067.
[117] L. Song, Z. Zhang, X. Xun, L. Xu, F. Gao, X. Zhao, Z. Kang, Q. Liao, Y. Zhang, *Research* **2021**, *2021*, 9801832.
[118] M. Xu, S. Wang, S. L. Zhang, W. Ding, P. T. Kien, C. Wang, Z. Li, X. Pan, Z. L. Wang, *Nano Energy* **2019**, *57*, 574.
[119] Y. Gao, H. Zhang, B. Song, C. Zhao, Q. Lu, *Biosensors* **2023**, *13*, 787.
[120] G. Gao, J. Yu, X. Yang, Y. Pang, J. Zhao, C. Pan, Q. Sun, Z. L. Wang, *Adv. Mater.* **2019**, *31*, 1806905.
[121] H. Zhang, J. Yu, X. Yang, G. Gao, S. Qin, J. Sun, M. Ding, C. Jia, Q. Sun, Z. L. Wang, *ACS Nano* **2020**, *14*, 3461.
[122] R. Li, D. Wei, Z. Wang, *Nanomaterials* **2024**, *14*, 165.
[123] C. Dang, C. Shao, H. Liu, Y. Chen, H. Qi, *Nano Energy* **2021**, *90*, 106619.
[124] S. Jang, Y. Joung, H. Kim, S. Cho, Y. Ra, M. Kim, D. Ahn, Z.-H. Lin, D. Choi, *Nano Energy* **2022**, *97*, 107213.
[125] S. Chatterjee, S. Saha, S. R. Barman, I. Khan, Y.-P. Pao, S. Lee, D. Choi, Z.-H. Lin, *Nano Energy* **2020**, *77*, 105093.
[126] X. Zhang, Y. Zheng, D. Wang, Z. U. Rahman, F. Zhou, *Nano Energy* **2016**, *30*, 321.
[127] J. Xiong, H. Luo, D. Gao, X. Zhou, P. Cui, G. Thangavel, K. Parida, P. S. Lee, *Nano Energy* **2019**, *61*, 584.
[128] X. Li, S. Li, X. Guo, J. Shao, Z. L. Wang, D. Wei, *Matter* **2023**, *6*, 3912.
[129] H. Helmholtz, *Ann. Phys.* **1853**, *165*, 211.
[130] Z. L. Wang, A. C. Wang, *Mater. Today* **2019**, *30*, 34.
[131] S. Lin, X. Chen, Z. L. Wang, *Chem. Rev.* **2022**, *122*, 5209.
[132] R. Zhang, S. Wang, M.-H. Yeh, C. Pan, L. Lin, R. Yu, Y. Zhang, L. Zheng, Z. Jiao, Z. L. Wang, *Adv. Mater.* **2015**, *27*, 6482.
[133] F. Zhan, A. C. Wang, L. Xu, S. Lin, J. Shao, X. Chen, Z. L. Wang, *ACS Nano* **2020**, *14*, 17565.
[134] A. S. Aji, R. Nishi, H. Ago, Y. Ohno, *Nano Energy* **2020**, *68*, 104370.
[135] F. Yi, X. Wang, S. Niu, S. Li, Y. Yin, K. Dai, G. Zhang, L. Lin, Z. Wen, H. Guo, J. Wang, M.-H. Yeh, Y. Zi, Q. Liao, Z. You, Y. Zhang, Z. L. Wang, *Sci. Adv.* **2016**, *2*, 1501624.
[136] D. Bao, Z. Wen, J. Shi, L. Xie, H. Jiang, J. Jiang, Y. Yang, W. Liao, X. Sun, *J. Mater. Chem. A* **2020**, *8*, 13787.
[137] A. Khan, S. Ginnaram, C.-H. Wu, H.-W. Lu, Y.-F. Pu, J. I. Wu, D. Gupta, Y.-C. Lai, H.-C. Lin, *Nano Energy* **2021**, *90*, 106525.
[138] J. You, J. Shao, Y. He, F. F. Yun, K. W. See, Z. L. Wang, X. Wang, *ACS Nano* **2021**, *15*, 8706.
[139] W. Xu, H. Zheng, Y. Liu, X. Zhou, C. Zhang, Y. Song, X. Deng, M. Leung, Z. Yang, R. X. Xu, Z. L. Wang, X. C. Zeng, Z. Wang, *Nature* **2020**, *578*, 403.
[140] B. Wang, Y. Wu, Y. Liu, Y. Zheng, Y. Liu, C. Xu, X. Kong, Y. Feng, X. Zhang, D. Wang, *ACS Appl. Mater. Interfaces* **2020**, *12*, 31351.
[141] H. Wang, Y. Sun, T. He, Y. Huang, H. Cheng, C. Li, D. Xie, P. Yang, Y. Zhang, L. Qu, *Nat. Nanotechnol.* **2021**, *16*, 811.
[142] X. Zhu, J. Hao, B. Bao, Y. Zhou, H. Zhang, J. Pang, Z. Jiang, L. Jiang, *Sci. Adv.* **2018**, *4*, aau1665.
[143] J. Fang, X. Zhang, P. Duan, Z. Jiang, X. Lu, C. Fu, Y. Zhang, Y. Yao, K. Shang, J. Qin, Y. Liu, T. Yang, *Mater. Horiz.* **2024**, *11*, 1261.
[144] L. Yang, F. Yang, X. Liu, K. Li, Y. Zhou, Y. Wang, T. Yu, M. Zhong, X. Xu, L. Zhang, W. Shen, D. Wei, *Proc. Natl. Acad. Sci. USA* **2021**, *118*, 2023164118.
[145] F. Yang, P. Peng, Z.-Y. Yan, H. Fan, X. Li, S. Li, H. Liu, T.-L. Ren, Y. Zhou, Z. L. Wang, D. Wei, *Nat. Energy* **2024**, *9*, 263.
[146] P. Peng, F. Yang, X. Li, S. Li, Z. Wang, D. Wei, *Cell Rep. Phys. Sci.* **2024**, *5*, 101824.
[147] H. Qian, D. Wei, Z. Wang, *Nano Res.* **2023**, *16*, 11718.
[148] N. Wang, Y. Zheng, Y. Feng, F. Zhou, D. Wang, *Nano Energy* **2020**, *77*, 105088.
[149] G. Zhu, Y. Su, P. Bai, J. Chen, Q. Jing, W. Yang, Z. L. Wang, *ACS Nano* **2014**, *8*, 6031.
[150] X. Wei, Z. Zhao, C. Zhang, W. Yuan, Z. Wu, J. Wang, Z. L. Wang, *ACS Nano* **2021**, *15*, 13200.
[151] M. Feng, X. Kong, Y. Feng, X. Li, N. Luo, L. Zhang, C. Du, D. Wang, *Small* **2022**, *18*, 2201442.
[152] X. Guo, F. Yang, X. Sun, Y. Bai, G. Liu, W. Liu, R. Wang, X. He, *Adv. Funct. Mater.* **2022**, *32*, 2201230.
[153] M. T. Rahman, M. S. Rahman, H. Kumar, K. Kim, S. Kim, *Adv. Funct. Mater.* **2023**, *33*, 2303471.
[154] M. Gouy, *J. Phys. Theor. Appl.* **1910**, *9*, 457.
[155] D. L. Chapman, *Philos. Mag.* **1913**, *25*, 475.
[156] O. Stern, *Electrochemistry* **1924**, *30*, 508.
[157] D. C. Grahame, *Chem. Rev.* **1947**, *41*, 441.
[158] P. Gu, S. Yang, X. Liu, G. Yang, *Soil Sci. Soc. Am. J.* **2020**, *84*, 494.
[159] I. M. Bhattacharyya, G. Shalev, *ACS Sens.* **2020**, *5*, 154.
[160] A. Hernández, J. Arcos, J. Martínez-Trinidad, O. Bautista, S. Sánchez, F. Méndez, *Int. J. Heat Mass Transfer* **2022**, *187*, 122522.
[161] A. Vacic, J. M. Criscione, N. K. Rajan, E. Stern, T. M. Fahmy, M. A. Reed, *J. Am. Chem. Soc.* **2011**, *133*, 13886.
[162] E. Stern, R. Wagner, F. J. Sigworth, R. Breaker, T. M. Fahmy, M. A. Reed, *Nano Lett.* **2007**, *7*, 3405.
[163] S. Das, S. Chakraborty, S. K. Mitra, *Phys. Rev. E* **2012**, *85*, 051508.
[164] S. Lin, L. Xu, A. Chi Wang, Z. L. Wang, *Nat. Commun.* **2020**, *11*, 399.
[165] S. Lin, X. Chen, Z. L. Wang, in *Encyclopedia of Solid-Liquid Interfaces*, (Eds: K. Wandelt, G. Bussetti), Elsevier, Oxford **2024**, p. 576.
[166] K. von Burg, P. Delahay, *Chem. Phys. Lett.* **1981**, *78*, 287.
[167] Y. Takakuwa, M. Niwano, M. Nogawa, H. Katakura, S. Matsuyoshi, H. Ishida, H. Kato, N. Miyamoto, *Jpn. J. Appl. Phys.* **1989**, *28*, 2581.
[168] Z. L. Wang, *Adv. Energy Mater.* **2020**, *10*, 2000137.
[169] F. H. J. Heyden, D. Stein, C. Dekker, *Phys. Rev. Lett.* **2005**, *95*, 116104.
[170] J. Chi, C. Liu, L. Che, D. Li, K. Fan, Q. Li, W. Yang, L. Dong, G. Wang, Z. L. Wang, *Adv. Sci.* **2022**, *9*, 2201586.
[171] Y. Dong, S. Xu, C. Zhang, L. Zhang, D. Wang, Y. Xie, N. Luo, Y. Feng, N. Wang, M. Feng, X. Zhang, F. Zhou, Z. L. Wang, *Sci. Adv.* **2022**, *8*, add0464.
[172] J. Yin, Z. Zhang, X. Li, J. Yu, J. Zhou, Y. Chen, W. Guo, *Nat. Commun.* **2014**, *5*, 3582.
[173] S. Yang, Y. Su, Y. Xu, Q. Wu, Y. Zhang, M. B. Raschke, M. Ren, Y. Chen, J. Wang, W. Guo, Y. Ron Shen, C. Tian, *J. Am. Chem. Soc.* **2018**, *140*, 13746.
[174] S. Kumar, A. Sharma, V. Gupta, M. Tomar, *J. Alloys Compd.* **2021**, *884*, 161058.
[175] Y. Ouyang, X. Li, S. Li, Z. L. Wang, D. Wei, *ACS Appl. Mater. Interfaces* **2024**, *16*, 18236.
[176] Y. Wu, Y. Luo, J. Qu, W. A. Daoud, T. Qi, *Nano Energy* **2019**, *64*, 103948.
[177] X. Chen, J. Xiong, K. Parida, M. Guo, C. Wang, C. Wang, X. Li, J. Shao, P. S. Lee, *Nano Energy* **2019**, *64*, 103904.
[178] K. Xia, Y. Tian, J. Fu, Z. Zhu, J. Lu, Z. Zhao, H. Tang, Z. Ye, Z. Xu, *Nano Energy* **2021**, *87*, 106210.
[179] R. Sarpeshkar, *Neural Comput.* **1998**, *10*, 1601.
[180] L. Zhang, D. Wang, *Matter* **2023**, *6*, 3698.
[181] Z.-H. Lin, G. Cheng, S. Lee, K. C. Pradel, Z. L. Wang, *Adv. Mater.* **2014**, *26*, 4690.
[182] L. Li, X. Li, W. Deng, C. Shen, X. Chen, H. Sheng, X. Wang, J. Zhou, J. Li, Y. Zhu, Z. Zhang, J. Yin, W. Guo, *Sci. Adv.* **2023**, *9*, adi2993.
[183] Y. Wei, X. Li, Z. Yang, J. Shao, Z. L. Wang, D. Wei, *Mater. Today* **2024**.
[184] F. Zhao, Y. Liang, H. Cheng, L. Jiang, L. Qu, *Energy Environ. Sci.* **2016**, *9*, 912.
[185] C. Shao, J. Gao, T. Xu, B. Ji, Y. Xiao, C. Gao, Y. Zhao, L. Qu, *Nano Energy* **2018**, *53*, 698.
[186] N. Chen, Q. Liu, C. Liu, G. Zhang, J. Jing, C. Shao, Y. Han, L. Qu, *Nano Energy* **2019**, *65*, 104047.

[187] T. Ding, K. Liu, J. Li, G. Xue, Q. Chen, L. Huang, B. Hu, J. Zhou, *Adv. Funct. Mater.* **2017**, *27*, 1700551.
[188] J. Li, K. Liu, T. Ding, P. Yang, J. Duan, J. Zhou, *Nano Energy* **2019**, *58*, 797.
[189] T. G. Yun, J. Bae, H. G. Nam, D. Kim, K. R. Yoon, S. M. Han, I.-D. Kim, *Nano Energy* **2022**, *94*, 106946.
[190] X. Zhang, X. Zhang, X. Fan, H.-T. Ren, J.-H. Lin, C.-W. Lou, T.-T. Li, *J. Mater. Chem. A* **2023**, *11*, 26173.
[191] J. Feng, M. Graf, K. Liu, D. Ovchinnikov, D. Dumcenco, M. Heiranian, V. Nandigana, N. R. Aluru, A. Kis, A. Radenovic, *Nature* **2016**, *536*, 197.
[192] Q. Ren, K. Chen, H. Zhu, J. F. Zhang, Z. G. Qu, *Energy Convers. Manage.* **2022**, *251*, 115032.
[193] J. Hao, B. Bao, J. Zhou, Y. Cui, X. Chen, J. Zhou, Y. Zhou, L. Jiang, *Adv. Mater.* **2022**, *34*, 2203109.
[194] D. Wei, F. Yang, Z. Jiang, Z. Wang, *Nat. Commun.* **2022**, *13*, 4965.
[195] P. Peng, F. Yang, Z. Wang, D. Wei, *Adv. Energy Mater.* **2023**, *13*, 2302360.
[196] Q. Zhang, Q. Liang, Q. Liao, M. Ma, F. Gao, X. Zhao, Y. Song, L. Song, X. Xun, Y. Zhang, *Adv. Funct. Mater.* **2018**, *28*, 1803117.
[197] C. Ye, D. Liu, P. Chen, L. N. Y. Cao, X. Li, T. Jiang, Z. L. Wang, *Adv. Mater.* **2023**, *35*, 2209713.
[198] K. R. Wijewardhana, T.-Z. Shen, J.-K. Song, *Appl. Energy* **2017**, *206*, 432.
[199] X. Yan, W. Xu, Y. Deng, C. Zhang, H. Zheng, S. Yang, Y. Song, P. Li, X. Xu, Y. Hu, L. Zhang, Z. Yang, S. Wang, Z. Wang, *Sci. Adv.* **2022**, *8*, abo7698.
[200] Y. Hu, M. Zhang, C. Qin, X. Qian, L. Zhang, J. Zhou, A. Lu, *Carbohydr. Polym.* **2021**, *265*, 118078.
[201] B. Bagchi, P. Datta, C. S. Fernandez, L. Xu, P. Gupta, W. Huang, A. L. David, D. Siassakos, S. Homer-Vanniasinkam, M. K. Tiwari, *Nano Energy* **2023**, *107*, 108127.
[202] C. Han, Z. Bai, H. Sun, L. Mi, Z. Sun, *J. Mater. Chem. A* **2024**, *12*, 723.
[203] S. Sun, H. Li, M. Zhang, B. Sun, Y. Xie, W. Zhou, P. Yang, H.-Y. Mi, Z. Guo, C. Liu, C. Shen, *Small* **2023**, *19*, 2303716.
[204] L. Ma, Z. Li, Z. Yuan, H. Wang, C. Huang, Y. Qiu, *J. Power Sources* **2021**, *492*, 229637.
[205] R. K. Tonnah, M. Chai, M. Abdollahzadeh, H. Xiao, M. Mohammad, E. Hosseini, M. Zakertabrizi, D. Jarrahbashi, A. Asadi, A. Razmjou, M. Asadnia, *ACS Nano* **2023**, *17*, 12445.
[206] Z. Wang, D. Wan, R. Fang, Z. Yuan, K. Zhuo, T. Wang, H. Zhang, *Appl. Surf. Sci.* **2022**, *605*, 154765.
[207] H. Zhao, M. Xu, M. Shu, J. An, W. Ding, X. Liu, S. Wang, C. Zhao, H. Yu, H. Wang, C. Wang, X. Fu, X. Pan, G. Xie, Z. L. Wang, *Nat. Commun.* **2022**, *13*, 3325.
[208] T. Jing, B. Xu, Y. Yang, *Nano Energy* **2021**, *84*, 105867.
[209] S. Li, Z. Zhang, F. Yang, X. Li, P. Peng, Y. Du, Q. Zeng, M. Willatzen, Z. L. Wang, D. Wei, *Device* **2024**, *2*, 100332.
[210] J. Zhang, S. Lin, M. Zheng, Z. L. Wang, *ACS Nano* **2021**, *15*, 14830.
[211] J. Zhang, S. Lin, Z. L. Wang, *ACS Nano* **2023**, *17*, 1646.
[212] X. Wei, B. Wang, X. Cao, H. Zhou, Z. Wu, Z. L. Wang, *Nat. Food* **2023**, *4*, 721.
[213] J. Zhang, X. Wang, L. Zhang, S. Lin, S. Ciampi, Z. L. Wang, *J. Am. Chem. Soc.* **2024**, *146*, 6125.
[214] Z. Tang, D. Yang, H. Guo, S. Lin, Z. L. Wang, *Adv. Mater.* **2024**, 2400451.
[215] Q. Sun, D. Wang, Y. Li, J. Zhang, S. Ye, J. Cui, L. Chen, Z. Wang, H.-J. Butt, D. Vollmer, X. Deng, *Nat. Mater.* **2019**, *18*, 936.

Xiang Li achieved his B.S. degree from the Shenyang University of Technology in 2018, and his M.S. degree from the Shenyang Jianzhu University in 2022. He is studying for a Ph.D. degree at the Beijing Institute of Nanoenergy and Nanosystems. His research interest is solid-liquid contact electrification and dynamic regulation of electrical double layer.

Zhong Lin Wang received his Ph.D. from Arizona State University in physics. He now is the Hightower Chair in Materials Science and Engineering, Regents' Professor, Engineering Distinguished Professor, and Director, Center for Nanostructure Characterization at Georgia Tech. Dr. Wang has made original and innovative contributions to the synthesis, discovery, characterization and understanding of fundamental physical properties of oxide nanobelts and nanowires, as well as applications of nanowires in energy sciences, electronics, optoelectronics, and biological science. He pioneered the field of piezotronics and piezo-phototronics by introducing piezoelectric potential gated charge transport process in fabricating new electronic and optoelectronic devices.

Di Wei serves as the principal investigator at BINN and heads the Iontronics Laboratory. As fellow of the Royal Society of Chemistry (FRSC) and senior member of Wolfson College at Cambridge University, he has published over 100 papers including Nature Energy, Nature Commun., PNAS, Adv Mater, Energ Environ Sci., Matter etc. as the first/corresponding author. He also has a portfolio of over 200 international patents (including PCT). He has edited three English books, published by Wiley and Cambridge University Press etc., focusing on nanotechnology for energy and sensor applications. Details can be found at: http://iontronics.group/.